Conformations of semiflexible polymers and filaments

Dissertation

zur Erlangung des akademischen Grades
Doktor der Naturwissenschaften (Dr. rer. nat)
in der Wissenschaftsdisziplin Theoretische Physik

eingereicht an der
Mathematisch-Naturwissenschaftlichen Fakultät der Universität Potsdam

angefertigt in der
Abteilung Theorie & Bio-Systeme
des Max-Planck-Instituts für Kolloid- und Grenzflächenforschung in Golm

von

Petra Gutjahr

geboren am 18. Januar 1979 in Saarbrücken

Dezember 2007

Max-Planck-Institut
für Kolloid- und Grenzflächenforschung

Universität
Potsdam

Zusammenfassung

Die biologische Funktion und die technologischen Anwendungen semiflexibler Polymere, wie DNA, Aktinfilamente und Nanoröhren aus Kohlenstoff, werden wesentlich von deren Biegesteifigkeit bestimmt. Semiflexible Polymere werden charakterisiert durch ihre Persistenzlänge, mit deren Definition sich der erste Teil dieser Arbeit befasst.

Anziehende Wechselwirkungen, wie sie z.B. bei der Adsorption, der Kondensation und der Bündelung von Filamenten auftreten, können die Konformation eines semiflexiblen Polymers verändern. Die Konformation ist dabei abhängig von der relativen Größe der Materialparameter und kann durch diese gezielt beeinflusst werden. Im Einzelnen werden hier die Morphologien semiflexibler Polymerringe, wie z.B. DNA oder ringförmiger Nanoröhren, untersucht, die auf drei verschieden strukturierten Substraten adsorbieren: (i) Ein topographischer Kanal, (ii) ein chemisch modifizierter Streifen und (iii) ein periodisches Muster topographischer Oberflächenstufen. Die Ergebnisse werden mit der Kondensation von Ringen durch anziehende Wechselwirkungen verglichen.

Des Weiteren wird die Bündelung zweier Aktinfilamente, deren Enden verankert sind, untersucht. Diese Systemgeometrie liefert eine systematische Methode, um die Stärke der Anziehung zwischen den Filamenten aus experimentell beobachtbaren Konformationen zu berechnen.

Abstract

The biological function and the technological applications of semiflexible polymers, such as DNA, actin filaments and carbon nanotubes, strongly depend on their rigidity. Semiflexible polymers are characterized by their persistence length, the definition of which is the subject of the first part of this thesis.

Attractive interactions, that arise e.g. in the adsorption, the condensation and the bundling of filaments, can change the conformation of a semiflexible polymer. The conformation depends on the relative magnitude of the material parameters and can be influenced by them in a systematic manner. In particular, the morphologies of semiflexible polymer rings, such as circular nanotubes or DNA, which are adsorbed onto substrates with three types of structures, are studied: (i) A topographical channel, (ii) a chemically modified stripe and (iii) a periodic pattern of topographical steps. The results are compared with the condensation of rings by attractive interactions.

Furthermore, the bundling of two individual actin filaments, whose ends are anchored, is analyzed. This system geometry is shown to provide a systematic and quantitative method to extract the magnitude of the attraction between the filaments from experimentally observable conformations of the filaments.

Contents

Contents

Chapter 1

Introduction

Biological and chemical systems offer a great variety of semiflexible polymers, filaments and fibers. Their rigidity is essential for many biological functions in cells and their applications in (bio-)nanotechnology. The aim of this chapter is to give a brief review on semiflexible polymers. Therefore, we start with a few well-known examples and illustrate why they are classified as semiflexible. The notion of the persistence length is thereby explained. On length scales comparable to this persistence length, the conformations of filaments are described theoretically by the worm-like chain model, which is the basis for all calculations within this thesis. As this model comprises only the elastic behavior, we briefly comment on some other properties, that may influence the shape of semiflexible polymers. The main part of this thesis considers shape deformations induced by attractive interactions responsible for adsorption, condensation and bundling of filaments. The physical origin of these interactions is explained and the resulting phenomena relevant for later chapters are introduced. We also give a brief summary of the most common methods used in related experimental studies. Biomembranes can be described as thin elastic sheets and, thus, are the two-dimensional analogues of semiflexible polymers. As the comparison between these systems is helpful in some cases, we also give a short introduction to fluid membranes. At the end of this chapter, we give an overview of this thesis.

1.1   Semiflexible Polymers and Filaments

Semiflexible polymers, filaments and fibers play a major role in biological and chemical physics. The most important property that governs their behavior on length scales relevant for their biological function in cells or for their applications in (bio-)nanotechnology is their resistance to bending or *bending rigidity*. Despite their considerable bending rigidity, however, they can still exhibit significant thermal shape fluctuations. Such one-dimensional objects, which are neither flexible, nor completely rigid, are called *semiflexible*.
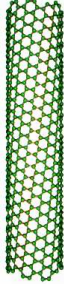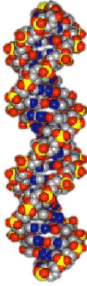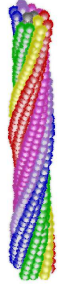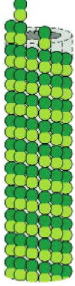
	Nanotube	DNA	F-actin	HbS fiber	Microtubule
D	1-2 nm	2 nm	7 nm	21 nm	25 nm
L_p	0.8 μm	50 nm	10 μm	$\sim$ 0.2-1 mm	$\sim$ 1-5 mm

Figure 1.1: Examples of semiflexible nanotubes, polymers, filaments and fibers: Carbon nanotubes, double-stranded DNA, the cytoskeletal filaments F-actin and microtubules, and HbS fibers associated with sickle cell anemia. The images and the experimental values for the persistence lengths are taken from [1, 2, 3, 4, 3] and [5, 6, 7, 8, 9], respectively. The values for the diameter and the persistence length of nanotubes refer to the single-walled type.

1.1.1 Examples

Certainly, the most prominent example is double-stranded DNA as the carrier of genetic information. It is composed of two polynucleotide chains that form a right-handed double helical structure. While the core of the helix is occupied by the basepairs, the backbones of the chains thereby wind around each other, see Fig. 1.1.

Furthermore, the shape, motility and internal structure of cells is governed by a sophisticated network of filaments called the *cytoskeleton*. Its mechanical properties strongly depend on those of its three main filamentous building blocks: F-actin (filamentous actin), microtubules and intermediate filaments. The former two possess considerable bending rigidity and are semiflexible. Actin filaments are made up of the protein G-actin (globular actin), which assembles into a two-stranded helical structure. Microtubules, on the other hand, are hollow cylinders, that typically consist of 13 protofilaments, which are themselves linear assemblies of tubulin subunits.

Another extensively studied semiflexible biopolymer is connected to the sickle-cell disease. Sickle cell anemia is a blood disorder caused by a genetic mutation, which leads to the transcription of sickle hemoglobin (HbS) instead of normal hemoglobin (HbA). At low oxygen conditions, HbS has the special ability to polymerize into long, twisted fibers, which are usually composed of 7 double

strands and have an elliptical cross section. These fibers evolve into a gel that deforms and rigifies red blood cells, so that the blood circulation through narrow blood vessels is obstructed causing a sickle cell crisis.

Moving on to synthetic macromolecules, carbon nanotubes are well-known for their unique mechanical, optical and electronical properties, which promise a wide range of technical applications. The molecular structure of nanotubes resembles a single layer, that has been wrapped up into a seamless cylinder. In the same way, nanotubes consisting of several concentric layers can be fabricated. Accordingly, one speaks of single-walled and multi-walled nanotubes. Both structures are very rigid and, thus, semiflexible. In Fig. 1.1, these different examples are ordered by the size of their diameter.

Strictly speaking, of all these examples only the single strands of DNA are polymers, if we define a polymer to be composed of repeating structural units or monomers connected by covalent chemical bonds. By contrast, the two strands of DNA are bound together by hydrogen bonds, while cytoskeletal filaments and HbS fibers are supramolecular aggregates, whose structure is determined by the hydrophobic effect and other non-covalent interactions. Carbon nanotubes are not classified as polymers (although the bonds between carbon atoms within a nanotube are covalent), but they belong to the fullerene structural family. For simplicity, however, we will refer to all these objects as semiflexible polymers meaning that they have similar elastic properties and, in this respect, are described similarly.

The schematic images in Fig. 1.1 suggest that semiflexible polymers occur only as open linear chains. But this is not true. In fact, various types of filaments are found to self-assemble into closed loops, such as DNA minicircles [10] and amyloid fibrils [11]. Particularly for DNA this closed form is important for many biological processes. For example, the genetic material of prokaryotes is stored in DNA rings. In other cases, the ring formation is achieved by chemical bonds, such as for carbon nanotubes [12, 5], or by attractive interactions between polymer segments, e.g. for filamentous actin [13] and DNA [14].

1.1.2 Why are polymers semiflexible?

A common starting point to answer this question is to identify structural differences between the above examples and a typical flexible polymer, say, polyethylene. The backbone of polyethylene is a chain made up of carbon-carbon bonds and has an effective diameter of a few Ångström. The orientation of adjacent bonds is (neglecting self-avoidance) uncorrelated. Therefore, the simplest model for a flexible polymer is to interpret the conformation of bonds as the path of a

random walker with fixed step size. At finite temperature, a flexible polymer assumes a shape that maximizes the conformational entropy. For a rather complete description of flexible polymers, see e.g. Refs. [15, 16, 17].

Compared to this simple picture of a flexible polymer, the semiflexible polymers depicted in Fig. 1.1 have an elaborate internal structure. The relative positions of the monomer subunits within the structure are more or less fixed, which restricts the displacement of individual monomers. In this sense, the semiflexible polymers shown in Fig. 1.1 resemble solid rods. Furthermore, the diameters exceed those of flexible polymers by at least one order of magnitude, see Fig. 1.1. In order to analyze the conformation of a semiflexible polymer, in the simplest approximation, we neglect all structural details and represent the rigid architecture of a semiflexible polymer by a homogeneous cylindrical rod, which is treated by means of standard elasticity theory [18]. In particular, one can assign a mesoscopic elastic bending modulus or bending rigidity κ to each type of semiflexible polymer.

According to [18], the bending rigidity κ is the product of the Young's modulus E and the inertia of the rod's cross section I, i.e.

$$\kappa = EI \quad \text{with} \quad I \equiv \int dS_{\text{cr}} \, r^2 = \frac{\pi}{4} \left(\frac{D}{2} \right)^4 . \tag{1.1}$$

Here S_{cr} indicates the area of the cross section and r the distance of a point on the cross section to the neutral axis. The last equality holds for a circular cross section with a diameter D. The bending rigidity has units energy times length. In biological and chemical systems, thermal fluctuations play an important role so that energies are commonly measured in units of T[1]. Thus, κ/T gives a length, which is called the *persistence length* L_p. It indicates the length scale above which thermal shape fluctuations influence the shape of a semiflexible polymer significantly and is prevalently used to specify the stiffness of a semiflexible polymer. Plugging in the values for the diameters given in Fig. 1.1 and a Young's modulus E of approximately 1 GPa for DNA and the cytoskeletal filaments, 0.1 GPa for HbS fibers and 1 TPa for single-walled nanotubes lead to estimates for the persistence length L_p at room temperature, which roughly match the measured values given in Fig. 1.1. As can be seen, the values for the persistence length extend over several orders of magnitude, which can be attributed to the fourth power of the diameter in the formula eq. (1.1) for I.

In summary, semiflexible polymers behave as homogenous elastic rods on length scales comparable to their persistence length L_p, which is significantly bigger than their diameter. This separation of length scales implies that architectural details, such as individual monomers and helical structure, should indeed

---

[1]Note that throughout this thesis, $k_B \equiv 1$ and T is measured in energy units.
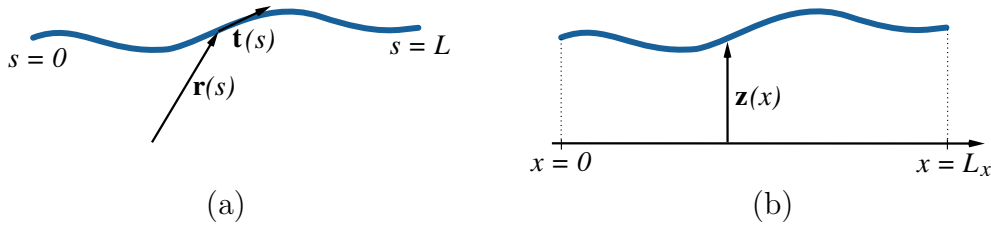
Figure 1.2: Schematic description of a semiflexible polymer in the worm-like chain model in (a) the arc length and (b) the parametrization by displacement fields.

be negligible on the scale defined by L_p. For instance, a helical turn of DNA encloses only 10 base pairs, whereas the persistence length is as long as 150 base pairs. Obviously, L_p is very important for the classification of semiflexible polymers and, therefore, Chapter 2 is dedicated to define this quantity more carefully.

1.1.3 The worm-like chain model

A powerful theoretical description comprising these notions is the *worm-like chain (WLC) model* that was suggested by Kratky and Porod in 1949 [19]. In this framework, the neutral axis of the semiflexible polymer is represented by a smooth space curve $\mathbf{r}(s)$ parametrized by the arc length s, which is schematically shown in Fig. 1.2(a). The endpoints of the semiflexible polymer are at $s = 0$ and $s = L$, where L denotes the contour length of the polymer. For filament rings, the two end points coincide with a single point on the contour that can be chosen arbitrarily. The arc length parametrization automatically implies that the tangent vector $\mathbf{t}(s) \equiv \partial_s \mathbf{r}(s)$, with $\partial_s \equiv \frac{\partial}{\partial s}$, has unit length. Thus, in d dimensions, each orientation of the tangent vector $\mathbf{t}(s)$ corresponds to a certain point of the hypersphere S_{d-1}. The bending energy is then proportional to the square of the curvature of the space curve $\mathbf{r}(s)$ integrated over the contour length and the Hamiltonian of the WLC model is given by

$$\mathcal{H}_{\mathrm{wlc}}\{\mathbf{t}(s)\} = \int_0^L ds \frac{\kappa}{2}(\partial_s \mathbf{t})^2, \quad \text{with } \mathbf{t}^2(s) = 1. \tag{1.2}$$

The condition on the length of the tangent vector $\mathbf{t}^2(s) = 1$ enforces the local (and global) inextensibility of semiflexible polymers within the WLC model. Furthermore, it implies that only $d - 1$ components of the d-dimensional tangent vector are independent. In particular, in two dimensions the tangent vector can simply be expressed in terms of tangent angles $\theta(s)$ so that the Hamiltonian depends

only on a single scalar function

$$\mathcal{H}_{\mathrm{wlc}}\{\theta(s)\} = \int_0^L ds \frac{\kappa}{2}(\partial_s\theta)^2 \ . \tag{1.3}$$

External forces or geometric constraints, such as walls, can give rise to a preferred orientation of a semiflexible polymer. If the conformation deviates only weakly from the straight conformation, which we define to be parallel to the x-axis, it is often more convenient to use the parametrization by displacement fields, see Fig. 1.2(b). Then the space curve describing the semiflexible polymer can be written as $\mathbf{r}(x) = (x, \mathbf{z}(x))$, where $\mathbf{z}(x)$ is the $(d-1)$-dimensional displacement field. It measures the displacement of the rod from the straight conformation at a certain position x on the preferred axis and is obviously only well-defined, if the conformation does not contain any overhangs. The ends of the polymer are located at $x = 0$ and $x = L_x$. Consequently, in the parametrization by displacement fields, the *projected length L_x* rather than the contour length L of a semiflexible polymer is automatically fixed during calculations. L is then obtained by integrating the length of the corresponding tangent vector $\mathbf{t}(x) = (1, \partial_x\mathbf{z}(x))$. An approximate version of the WLC Hamiltonian is obtained by expanding (1.2) in the displacement field $\mathbf{z}(x)$ up to second order

$$\mathcal{H}_{\mathrm{wlc}}\{\mathbf{z}(x)\} \simeq \int_0^{L_x} dx \frac{\kappa}{2}(\partial_x^2\mathbf{z})^2, \tag{1.4}$$

where the gradients of $\mathbf{z}(x)$ are assumed to be small.

Whatever parametrization is chosen, semiflexible polymers assume a conformation of minimal bending energy with respect to appropriate boundary conditions, provided that the system is equilibrated and thermal fluctuations are small compared to the stiffness of the semiflexible polymer. The stationary shapes of semiflexible polymers are found by solving the respective Euler-Lagrange equation, i.e. the first variation of $\mathcal{H}_{\mathrm{wlc}}$ has to vanish. Therefore, without further constraints, an open polymer acquires a straight conformation, while a closed polymer ring forms a circle.

On the basis of the WLC Hamiltonian (1.2), the persistence length L_p is usually defined as the length scale over which the correlation of tangent orientation decays [19, 20, 21]. The corresponding correlation function is given by

$$\langle \mathbf{t}(s) \cdot \mathbf{t}(s') \rangle = e^{-\frac{|s-s'|}{L_p}} \ . \tag{1.5}$$

But also other quantities, that help to distinguish the behavior of semiflexible from flexible polymers experimentally, can be obtained as functions of the contour length and the persistence length: The mean square end-to-end distance of a

semiflexible polymer subject to thermal fluctuations [19] and the force-extension relation [22], which reflects how a semiflexible polymer resists stretching with an entropic force, are probably the most prominent examples for such quantities.

1.1.4 Extensions of the worm-like chain model

If very large forces are applied to the ends of a semiflexible polymer, end-to-end distances that slightly exceed the contour length have been observed for DNA [23], F-actin [24] and polyelectrolytes (see below) [25]. Obviously, these results cannot be explained by the WLC model, in which semiflexible polymers are assumed to be inextensible. One way to solve this problem is to add a corrective term, that accounts for the overall extension of a semiflexible polymer, to the WLC model [26, 27, 28, 29]. Alternatively, the polymer can be described by a discretized version of the WLC Hamiltonian using microscopic bonds with a finite extensibility [30, 31, 32]. For F-actin, forces above 50 pN are needed to stretch a filament beyond its contour length, which is well above the forces considered in this thesis, cf. Chapter 4.

Furthermore, most biopolymers carry ionizable groups along their backbone and dissociate in solution into charged polymers and counterions. Such polymers are so-called *polyelectrolytes*. The theoretical description of polyelectrolytes, see e.g. Ref. [33], is much more complicated than that of neutral polymers, because of the long-ranged (Coulombic) interactions between polymer segments. In ionic solutions these repulsive interactions are screened by the formation of counterion clouds around the polymer backbone. If the solution is dilute, one can use the Debye-Hückel approximation, in which the interaction between two monomers is assumed to decay exponentially on the scale of the screening length

$$l_{DH} \equiv (8\pi q_s^2 l_B c_s)^{-1/2}. \tag{1.6}$$

Here q_s and c_s are the valency and the concentration of the salt ions and

$$l_B \equiv \frac{e_0^2}{4\pi\epsilon_0\epsilon T} \tag{1.7}$$

is the Bjerrum length denoting the distance, at which the Coulombic interaction between two elementary charges e_0 is equal to T. Due to screening one might expect that the effect of electrostatic interactions should no longer be noticeable on length scales well above l_{DH}. By contrast, Odijk, Skolnick and Fixman [34, 35] showed that a polymer bearing evenly distributed charges along its backbone at distances r exhibits an electrostatic stiffening, which is effectively described by an additive correction to the persistence length, namely

$$L_p^* = L_p + L_{OSF} \quad \text{with} \quad L_{OSF} \sim \frac{l_B l_{DH}^2}{r^2}. \tag{1.8}$$

In biological systems, l_{DH} and, thus, L_{OSF} becomes small, so that this correction will be neglected here.

Another phenomenon, which is beyond the scope of the worm-like chain model and likewise beyond the scope of this thesis, is the supercoiling known for DNA. If a twist strain is imposed, e.g. by an enzyme, to a DNA molecule, this strain can be relaxed by allowing the DNA to wrap around itself, which is mathematically denoted as a *writhe*. In everyday life, the knotted configurations of telephone cables are an intuitive example for supercoiling. For closed DNA and for the case where the ends are fixed, the sum of the number of twists of the double helix and the number of writhes is conserved. This conservation law has to be included into calculations, for details see e.g. [36].

1.1.5 Interacting semiflexible polymers

So far, only the properties of individual semiflexible polymers were considered. However, in most biological and chemical systems, semiflexible polymers are not isolated and self-assemble into larger structures, as in the cytoskeleton. The smallest structures made of semiflexible polymers are condensates consisting of a single semiflexible polymer, considered at the end of Chapter 3, and bundles of two filaments, which are the topic of Chapter 4. On the other hand, in experiments it is often beneficial to adsorb polymers to surfaces, e.g. to control their shape as in Chapter 3. This is certainly only possible, if the attraction between polymer and substrate is strong enough to render the adsorbed state energetically favorable.

In the simplest case, semiflexible polymers adhere to each other due to van der Waals forces. Especially for carbon nanotubes this attraction is rather strong and suffices to stabilize highly strained rings formed by coiling [12]. In comparison, the mechanisms that lead to an effective attraction between biopolymers are much more complex usually being a combination of many different effects [37, 38]. Here we concentrate on the bundling induced by multivalent cations. As we learned in the last paragraph, most biopolymers are negatively charged and, consequently, repel each other. At the same time, a polyelectrolyte attracts counterions from the buffer solution, which form a cloud around the polymer. This process is known as counterion condensation [39, 40]. The sheath of counterions is polarizable, which, in fact, can lead to an effective attraction between polyelectrolytes via so-called 'salt bridges'.

The resulting attraction is surprisingly strong. In vitro, multivalent cations cause DNA – despite their rigidity – to collapse into compact, highly ordered configurations, mostly rod-like condensates or toroids [37], see Fig. 1.3(a) and Chapter 3. These condensates show great similarities to DNA packaged into virus capsids and, in addition, are interesting for gene transfer in gene therapy.

(a)   (b)
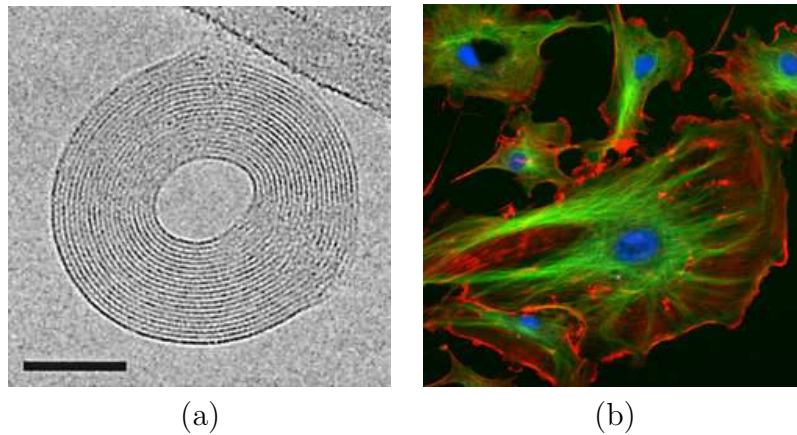
Figure 1.3: (a) Micrograph of a toroidal condensate of λ phage DNA [41]. The scale bar is 50 nm. (b) Image of the eukaryotic cytoskeleton [42]. Microtubules, actin filaments and the cell nucleus are shown in green, red and blue, respectively.

Analogous to DNA condensation, also actin filaments have been observed to form bundles [38] and toroidal condensates [13], which are, due to the greater bending rigidity, much bigger than those made of DNA.

In the cytoskeleton, see Fig. 1.3(b), the filaments are linked together by various types of proteins with typically two binding domains. We focus only on crosslinker proteins binding actin filaments, which are relevant for the experiments we will consider in Chapter 4. For further details of the cytoskeleton see e.g. Ref. [3]. Many of these crosslinkers are found in the actin cortex – a thin layer just beneath the cell membrane – which is to a large extend responsible for the mechanical support and the motility of animal cells. The arising structures within the actin cortex strongly depend on the properties of the crosslinking proteins [43, 44]: Whereas some proteins, such as filamin, generate gel-like networks with orthogonal interconnections, bundles of parallel filaments, as found in filopodia and in stress fibers, are produced by e.g. fimbrin, α-actinin and the motor protein myosin II. The latter protein is, in contrast to the other mentioned crosslinkers, an example of an active binding protein, which can convert chemical energy into mechanical work and move along a filament.

Semiflexible polymers can not only interact with each other, but also with other objects, in particular, with surfaces [45]. The adsorption to substrate surfaces exhibits great advantages for the direct observation of individual polymers, see the next paragraph, and plays an important role for applications in (bio-)nanotechnology, cf. Chapter 3. A typical experimental system to study adsorbed semiflexible polymers is DNA deposited on mica [46]. Both materials – mica and DNA – are negatively charged. Using essentially the mechanisms as mentioned

above, adsorption can be achieved by adding divalent cations. The cations constituting the ion cloud can freely diffuse along the surface so that the adsorbed DNA can be treated as a free worm-like chain in two dimensions. Similar to the attraction between nanotubes, also the adsorption of nanotubes is governed by van der Waals interactions [47]. Alternatively, the nanotubes are coated with surfactants, which enhances the binding to hydrophobic substrate domains, see e.g. Ref. [48].

In this thesis, all interactions introduced above will be described by the same simplified theoretical model. For attractions between two filaments, it consists of a spherical potential well of radius l and an effective strength W, $W < 0$ [49]. For the case of a semiflexible polymer adsorbing to a substrate, the spherical potential is replaced by a planar square well potential. The potential range l depends on the type of interaction and is usually taken to be small compared to other relevant length scales. For van der Waals and screened electrostatic interactions l is comparable to the polymer diameter D and the screening length l_{DH}, respectively. On the other hand, for crosslinkers, the potential range l is determined by the distance between the two binding domains and, in addition, the binding to filaments may exhibit a preferred angle. The details can be found in Sections 3.2.1, 3.3.1, 3.5 and 4.3, respectively. In either case, interactions between crosslinking proteins or cations as well as dynamic effects are essentially neglected.

1.1.6   Experimental methods

In the last decades, the properties of semiflexible polymers have been extensively probed in experiments. At the same time sophisticated techniques have been developed, that allow to visualize the conformation of a single semiflexible polymer and its pointwise manipulation in a highly controlled fashion. Most commonly used are magnetic [50] or optical tweezers [51] and scanning probe techniques, such as atomic force microscopy (AFM) [52], that reach sensitivities in the piconewton range and spatial resolutions down to the nanometer scale.

Magnetic or optical tweezers work via the control or trapping of single objects, such as beads, that can be attached to one end of a semiflexible polymer. In this way, the force-extension relation of DNA was measured for the first time [50, 53]. On the other hand, AFM provides a powerful tool to deal with semiflexible polymers adsorbed to solid surfaces. A cantilever with a sharp tip senses the topography and the local mechanical properties of a surface with very high spatial resolution. In this type of experiment, one can extract information directly from the polymer's shape. For instance, the persistence length can be determined by measuring tangent correlations or end-to-end distances, see e.g. Ref. [46]. The

disadvantages of this method are the temporal resolution limited by relatively long scanning times and the necessity to confine the probed semiflexible polymers to a solid surface, which might alter their physical properties. But then the interplay between a semiflexible polymer and a substrate surface can also be exploited for the immobilization and controlled manipulation of DNA and other semiflexible polymers required in bionanotechnology. For this purpose, the possibility to achieve such shape control for semiflexible polymer rings using simple striped surface structures is explored in Chapter 3.

Moreover, in Chapter 4, we consider experiments that create a biomimetic model of the actin cortex. These experiments use an alternative approach, that provides well-defined boundary conditions for the quantitative analysis of filament conformations, but does not rely on the adsorption of filaments. There, the filaments are locally attached to so-called microscopic pillars [54], but are otherwise unconstrained. To avoid interactions with the underlying substrate the height of the pillars is chosen to be comparable or bigger than the contour length of the filaments. Further details concerning these experiments are given in Section 4.2.

1.2 Fluid membranes

Membranes, such as the cell membrane, act as enclosing or separating elements in biological systems [3] and constitute a wide field of research for many years already. Their detailed composition might be manifold and very complicated, but the basic component of all biological membranes are lipid molecules, see Fig. 1.4. Lipids are typically amphiphilic – that is, they have a hydrophilic (water soluble) head and a hydrophobic (water insoluble) tail – and as a result, spontaneously form thin bilayers in water. In order to avoid boundaries, where hydrophobic tails are exposed to water, fluid membranes form closed bags or *vesicles*. If the lipids can diffuse freely within the two layers, the two-dimensional membrane is fluid.

Similar to semiflexible polymers, the shapes of fluid membranes can be described by means of elasticity theory. On length scales large compared to the size of the lipids, they can be modelled as thin elastic sheets. Their conformation in three-dimensional space is governed by the bending rigidity [56, 57, 58], while other elastic moduli play only a minor role. From this point of view, fluid membranes are the two-dimensional analogue of semiflexible polymers. For a review of the conformation of membranes, see e.g. [59].

The shape of a membrane is represented by a three-dimensional vector field $\mathbf{R}(s_1, s_2)$ depending on the coordinates s_1 and s_2 that parametrize the membrane surface. If the shape deviates only weakly from a flat plane, say, the
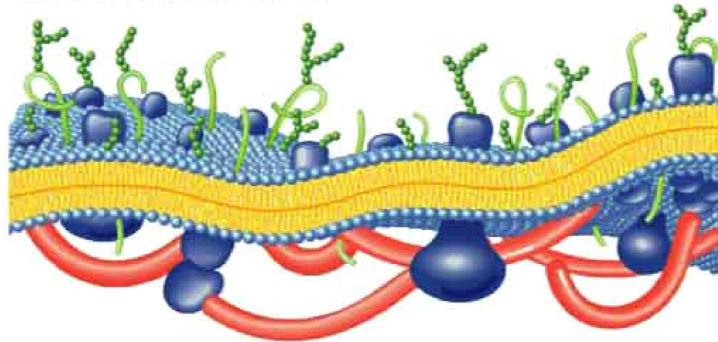
Figure 1.4: Schematic image of a biomembrane [55] consisting of a bilayer of lipids (heads: light blue, tails: yellow), which is decorated with proteins (green and blue) and anchored polymers (red). The thickness of the phospholipid bilayer is approximately 5 nm.

xy-plane, it is common to parametrize the membrane by displacement fields. Similar to the one-dimensional case, the embedding functions are then expressed as $\mathbf{R}(x, y) = (x, y, z(x, y))$, where $z(x, y)$ denotes the height function with respect to the reference plane. The corresponding Hamiltonian was first introduced by Canham [56] and Helfrich [57] and can be written in a rather compact form

$$\mathcal{H}_{\mathrm{mem}} = \int dA \left\{ \frac{\kappa}{2}(2M)^2 + \bar{\kappa}G \right\}. \tag{1.9}$$

In principle, this Hamiltonian is the two-dimensional generalization of eq. (1.2). Here, the integral extends over the membrane surface, dA indicating the infinitesimal area element of the membrane surface. The curvature of a surface is described by the curvature tensor, which can be diagonalized at every point. Its eigenvalues C_1 and C_2 are the principle curvatures, which specify the largest and the smallest local curvature. As the only quantities allowed to appear in the Hamiltonian are scalars, only the trace and the determinant of the curvature tensor, namely

$$M \equiv \frac{C_1 + C_2}{2} \quad \text{and} \quad G \equiv C_1 C_2, \tag{1.10}$$

occur in eq. (1.9). M and G are called the mean and the Gaussian curvature, respectively. According to the Gauss-Bonnet theorem, the integral $\int dA\, G$ depends only on the topology of the surface. Hence, as long as the membrane surface does not undergo topological changes, the second term yields only a constant contribution and the first term can be identified with (1.2). The bending rigidity is denoted by κ analogous to the last section, whereas the new parameter $\bar{\kappa}$

is the bending modulus associated with the Gaussian curvature. It should be noted, that in this case κ and likewise $\bar{\kappa}$ have units of energy. The mathematical definitions of the above quantities can be found in App. A.

The stationary shapes of vesicles are obtained by minimizing $\mathcal{H}_{mem}$ supplemented by additional constraints, such as a prescribed membrane area or a fixed enclosed volume. One of the key simplifications often needed to make explicit calculations feasible, is to assume an axisymmetric conformation. The computational problem is then reduced to find the one-dimensional contour of the vesicle shape in the plane. It is therefore not surprising, that in some cases the treatment of vesicles and adsorbed ring polymers displays great similarities, which will also be encountered in Chapter 3.

For phospholipid bilayers, the bending rigidity is deduced from experiments to be of the order of 10 - 20 T [60, 61]. Consequently, thermal shape fluctuations are also relevant for fluid membranes. For membranes, the notion of a persistence length was introduced by de Gennes and Taupin [62], but the details of this definition and how it can be compared to the persistence length of semiflexible polymers will be postponed to the next chapter.

The Canham-Helfrich model has proven to provide the theoretical framework to explain various phenomena. In particular, it is suitable to describe the elastic behavior of vesicles, which have become a popular model system to investigate properties of biological membranes over the years. Among the major achievements in this context, see e.g. Ref. [63, 64] for a review, are the correct description of non-trivial equilibrium shapes of vesicles, which are similar to shapes observed for red blood cells, and the adhesion of vesicles, which is important for many biological applications [3].

1.3 Overview

This thesis is organized as follows. The topic of the next chapter is the relation between the persistence length of semiflexible polymers and the renormalization of the bending rigidity. First, we review existing definitions for the persistence length based on tangent correlations for semiflexible polymers and on the renormalized bending rigidity for membranes. Applying both definitions to polymers shows that they are, in fact, incompatible. In order to clarify this issue, we calculate the renormalization of the bending rigidity of a semiflexible polymer by a real-space renormalization analysis as is commonly used for Ising-like spin systems. From the asymptotic behavior of the renormalized bending rigidity, we deduce a new definition for the persistence length, which generalizes the conventional definition, but gives identical results. The content of this chapter has been published previously in Refs. [65, 66].

Chapter 3 considers the controlled adsorption of semiflexible polymer rings on surfaces containing chemically or topographically modified stripes. For either type of structure, we study the equilibrium morphologies by calculating a projection of the energy landscape, determining its local minima and their stability. The results are summarized in morphological diagrams, and the influence of thermal fluctuations is discussed. As an example of more complicated structures, we also consider a substrate with a periodic topographical pattern. Finally, we compare our findings to the morphological transitions related to the condensation of a semiflexible ring by attractive polymer-polymer interactions.

In Chapter 4, we present a theoretical analysis based on experiments, which study the partial zipping of actin filaments with anchored ends. First, we describe the experimental setup to motivate our theoretical model. We distinguish between two regimes, namely, the case of strong and weak attraction between the filaments. For either case, the resulting conformations are discussed at zero temperature and in the presence of thermal fluctuations in order to reveal how the attraction strength can be extracted from experimentally observed data.

Finally, we end with a summary of all three topics and an outlook on possible extensions and open questions for future work.

Chapter 2

Persistence length of semiflexible polymers and bending rigidity renormalization

The persistence length of semiflexible polymers (and one-dimensional fluid membranes) is obtained from the renormalization of their bending rigidity. The renormalized bending rigidity is calculated using an exact real-space functional renormalization group transformation based on a mapping to the one-dimensional Heisenberg model. The renormalized bending rigidity vanishes exponentially at large length scales and its asymptotic behavior is used to define the persistence length. For semiflexible polymers, our results agree with definitions based on the asymptotic behavior of tangent correlation functions. Our definition differs from the one commonly used for fluid membranes, which is based on a perturbative renormalization of the bending rigidity.

2.1   Introduction

Thermal fluctuations of two-dimensional fluid membranes and one-dimensional semiflexible polymers or filaments are governed by their bending energy and can be characterized using the concept of a *persistence length L_p*, which is illustrated in Fig. 2.1. In the absence of thermal fluctuations at zero temperature, fluid membranes are planar and (open) semiflexible polymers are straight because of their bending rigidity. Sufficiently large and thermally fluctuating membranes or semiflexible polymers lose their planar or straight conformation. Only subsystems of size $\ell \ll L_p$ appear rigid and maintain an average planar or straight conformation with a preferred normal or tangent direction, respectively. Membrane patches or polymer segments of sizes $\ell \gg L_p$, on the other hand, appear flexible. In the "semiflexible" regime $\ell \sim L_p$ the statistical mechanics is governed by the competition of the thermal energy T and the bending rigidity κ. Experimental values for the persistence length of one-dimensional semiflexible biopolymers vary from 50 nm for double-stranded DNA [6], up to the mm-range for microtubules [9], cf. Fig. 1.1. The persistence lengths of two-dimensional fluid membranes are typically much larger than experimental length scales.

Although the qualitative idea of the persistence length is simple, it poses a rather complex problem to give a systematic definition of L_p, which is applicable
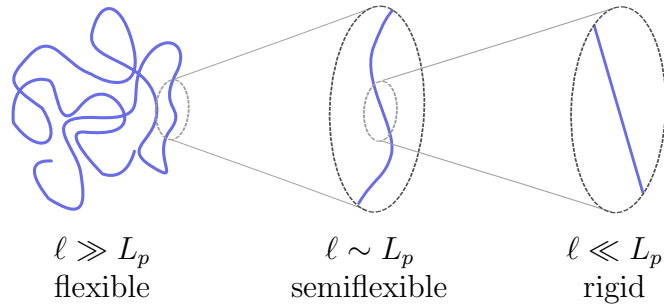
$$\ell \gg L_p \qquad\qquad \ell \sim L_p \qquad\qquad \ell \ll L_p$$
flexible   semiflexible   rigid

Figure 2.1: Schematic contour of a thermally fluctuating semiflexible polymer on different length scales ℓ. On very short length scales $\ell \ll L_p$ the thermal energy is not sufficient to introduce a bend in the contour of the semiflexible polymer (right), whereas on large scales $\ell \gg L_p$ the conformational entropy dominates, so that the orientational order is completely destroyed (left). The intermediate regime $\ell \sim L_p$ is characterized by the balance between thermal fluctuations and the stiffness of the semiflexible polymer (middle).

to semiflexible polymers and their higher dimensional counterparts, membranes and interfaces. In fact, there exists no universal definition of L_p so far, but instead, several definitions are used either for one- or two-dimensional objects. All definitions are based on the same concept, namely, to identify a parameter that allows to differentiate between the three different regimes, illustrated in Fig. 2.1, and, thus, to establish a criterion that determines, if some elastic object can be treated as semiflexible. But whether the resulting definitions are really equivalent can not be taken for granted.

Two widespread definitions are reviewed in the next section. The first is prevalently used for polymers and defines the persistence length as the length scale above which the orientation of the tangent vectors along the semiflexible polymer is lost and the shape can be decomposed into approximately independent segments of size L_p, see eq. (1.5) in Chapter 1. For the second definition, which is well-established in the context of membranes, a scale dependent bending rigidity is introduced reflecting the influence of thermal fluctuations on the elastic behavior on large length scales. One possible definition of L_p is then to identify L_p with the length scale where the (perturbatively) renormalized bending rigidity vanishes. A comparison of these definitions is only feasible for semiflexible polymers and yields *disagreeing* results for L_p. This discrepancy can be attributed to two reasons: Firstly, the persistence length derived from κ-renormalization relies on perturbative calculations limited to rather small scales, and, hence, might not be significant for the long range behavior. Secondly, the two definitions are indeed not equivalent, which brings back the issue of a universal definition of L_p.

In this chapter, we concentrate on a discrete description for semiflexible polymers, which is equivalent to the one-dimensional classical Heisenberg model. The advantage of this model is that the κ-renormalization as well as the tangent correlation function are exactly computable in arbitrary dimensions d. Consequently, a direct comparison of the persistence length determined via κ-renormalization and via the tangent correlation function is possible. We introduce this model in Section 2.3. The κ-renormalization is carried out in a similar fashion as is commonly used for Ising-like spin systems. In contrast to the nonlinear σ-model, we find nontrivial results for $\kappa(\ell)$ both in two and in three dimensions. As expected for an exact result, $\kappa(\ell)$ is always positive and approaches zero only asymptotically. We analyze the large scale behavior of $\kappa(\ell)$ leading to a power series of exponentials with the same decay length as obtained for the tangent correlations. We define this length scale to be the persistence length of the polymer.

2.2 Various definitions of L_p

2.2.1 Decay of conformational orientation

Consider the schematic shape of a freely fluctuating semiflexible polymer in Fig. 2.1. On small length scales (right), it is perfectly straight so that all its tangent vectors point to the same direction. By contrast, this tangential orientation is lost on very large length scales (left). The physical quantity measuring this behavior is the tangent correlation function. Accordingly, for semiflexible polymers with one internal dimension, L_p is usually defined by the characteristic length scale for the exponential decay of the two-point correlation function between unit tangent vectors $\mathbf{t}$ along the polymer.

In Chapter 1, the worm-like chain model [19] was presented as a continuous model for an inextensible semiflexible polymer of contour length L. The Hamiltonian is given by the bending energy, eq. (1.2). For a WLC embedded in d spatial dimensions, the tangent correlation function is found to be [20, 21]

$$\langle \mathbf{t}(s) \cdot \mathbf{t}(s') \rangle = e^{-|s-s'|/L_p}, \quad \text{with } L_p = \frac{2}{d-1}\frac{\kappa_0}{T} \tag{2.1}$$

where κ_0 is the (unrenormalized) bending rigidity of the model[1]. The thermal average $\langle . \rangle$ is taken by summing over all possible polymer shapes weighted by the Boltzmann factor containing the bending energy (1.2). The polymer contour is completely determined by the field $\mathbf{t}(s)$ of unit tangent vectors so that, in practice, the sum over all conformations is achieved by functional integration over $\mathbf{t}(s)$, as will be seen in detail in the next section.

---

[1]In this chapter, the mesoscopic bending rigidity κ is labeled with an index 0 to distinguish between 'bare' and renormalized quantities. In subsequent chapters, this distinction will become redundant and the index will be omitted again.

For fluid membranes with two internal dimensions, the quantity analogous to (2.1) is the correlation function of unit normal vectors, since the normal vectors measure the local orientation of a surface. An approximate result for the correlation function of normals has been given in Ref. [15], but a rigorous treatment is missing because of the more involved differential geometry, which gives rise to a number of complications discussed in the following.

Surfaces cannot be fully determined by specifying an arbitrary set of normal vectors, because they have to fulfill additional compatibility conditions in terms of the metric and curvature tensors, the equations of Gauss, Mainardi and Codazzi, which ensure their continuity, cf. App. A. Implementations of these constraints lead to a considerably more complicated field theory than (1.2) describing a two-dimensional fluid membrane in terms of its normal vector field [67].

Not only the Hamiltonian itself becomes much more complicated. Even the definition of thermal averages $\langle . \rangle$ is far from obvious for membranes. As mentioned earlier, it involves a summation over all possible surfaces, but each physical conformation should be counted only once. A particular surface shape can be parametrized in many different ways, so in order to avoid overcounting, one has to choose a parametrization. At the same time, one has to assure that the obtained results do not depend on this choice (reparametrization invariance). The Fadeev-Popov procedure [68, 69, 70] implements this issue by means of an additional factor in the path integral measure. For semiflexible polymers, the parametrization via arc length guarantees the correct counting and reparametrization invariance automatically. The respective Fadeev-Popov factor is thus equal to one. Furthermore, in the arc length parametrization, the degrees of freedom are equidistantly distributed along the contour of the polymer and their total number is preserved automatically. Such a favorable parametrization as the arc length does not exist for membranes. In order to fix the number of degrees of freedom of a membrane patch, another factor has to be included, which is known as the Liouville factor [71, 72]. The even distribution of the degrees of freedom cannot be assured, since, for membranes with arbitrary shape, it is merely possible to find a local coordinate system, which defines a metric *proportional* to the Euclidean metric. The proportionality factor, however, may vary along the membrane. This particular choice is known as the conformal gauge.

In most cases, one is only interested in the limit of very rigid membranes, where the partition sum can approximately be truncated to surface shapes that deviate only weakly from the flat plane. Then the parametrization by displacement fields is adequate and corrections arising from the Fadeev-Popov and the Liouville factor do not emerge below second order in T/κ_0. Nevertheless, the difficulties described above strongly indicate that exact calculations in this context are rarely manageable.

18

2.2.2 Thermal softening and stiffening

For fluid membranes, an alternative definition of the persistence length L_p has been given, which is linked to the effect of κ-renormalization. The mode coupling between thermal shape fluctuations of different wave lengths modifies the large scale bending behavior, which can be described by an effective or *renormalized* bending rigidity κ. Transferring this notion to Fig. 2.1 would lead to a different value for the effective bending rigidity $\kappa(\ell)$ in each regime. In particular, this schematic case exemplifies the thermal softening of a polymer, that is, $\kappa(\ell)/T$ decreases from right to left.

The renormalized κ has been calculated using different perturbative renormalization group (RG) approaches [73, 74, 75, 76, 77, 78, 70, 79, 80], which are limited to the first order in T/κ_0 due to the reasons presented in the previous subsection. The results are still controversial: Several authors [73, 74, 75, 76, 77, 78, 70] find a thermal softening of the membrane with increasing length scales, but differing prefactors, whereas Pinnow and Helfrich [79, 80] obtained the opposite result. Furthermore, different definitions of the persistence length are considered in these approaches: In Refs. [76, 77, 78, 70], L_p is identified with the length scale, where the renormalized bending rigidity κ vanishes, while Helfrich and Pinnow defined L_p via the averaged absorbed area [73, 74, 75, 79, 80].

Even though a lot of effort was made to find the κ-renormalization for the membrane, it has never been calculated for the simpler case of the semiflexible polymer. In this chapter, we obtain an exact real-space RG scheme for the bending rigidity of a semiflexible polymer or a one-dimensional fluid membrane, which allows us to define the persistence length as the characteristic decay length of the renormalized bending rigidity.

In principle, a perturbative result for the effective κ of a semiflexible polymer can be deduced from the RG analysis of the one-dimensional nonlinear σ-model, which is equivalent to the WLC Hamiltonian (1.2). After a Wilson-type momentum-shell RG analysis, one obtains the effective rigidity, see e.g. Refs. [81],

$$\frac{\kappa(\Lambda)}{T} = \frac{\kappa_0}{T}\left[1 - \frac{T}{\kappa_0}\frac{d-2}{\pi}\left\{\frac{1}{\Lambda} - \frac{1}{\Lambda_0}\right\} + \mathcal{O}(T^2/\kappa_0^2)\right], \qquad (2.2)$$

which depends on the momentum Λ. The parameter $\kappa_0 = \kappa(\Lambda_0)$ is the 'bare' coupling taken at the high momentum cut-off $\Lambda_0 = \pi/b_0$, which is given by a 'lattice spacing' or bond length b_0. Using also $\Lambda = \pi/\ell$ we obtain the renormalized $\kappa = \kappa(\ell)$ as a function of the length scale ℓ. Following the procedure previously used for membranes, the persistence length can be defined via

$$\kappa(L_p) \equiv 0 \quad \text{and, thus,} \quad L_p \simeq \frac{\pi^2}{d-2}\frac{\kappa_0}{T}. \qquad (2.3)$$

19

For the case of the polymer in the plane ($d = 2$), the Hamiltonian simplifies to a free or Gaussian field theory such that $\kappa = \kappa_0$ is unrenormalized to all orders in κ_0/T and, therefore, L_p as defined via $\kappa(L_p) \equiv 0$ would become infinitely large.

A similar perturbative momentum-shell RG procedure is possible in the parametrization of a weakly bent semiflexible polymer by displacement fields, analogous to the RG analysis for two-dimensional membranes [76]. There the polymer is parametrized by its projected length x with $0 < x < L_x$, where L_x is the fixed projected length of the semiflexible polymer while its contour length becomes a fluctuating quantity. The renormalized $\kappa = \kappa(\ell_x)$ becomes a function of the projected length scale ℓ_x, which complicates a comparison with the result (2.2), which was derived in an ensemble of fixed contour length. Using the analogous criterion $\kappa(L_p) = 0$ we obtain

$$L_p \simeq \frac{2\pi^2}{3d-1} \frac{\kappa_0}{T} \tag{2.4}$$

within the parametrization by displacement fields.

A comparison of the RG results from the non-linear σ-model, see eq. (2.3), and the one obtained in the parametrization by displacement fields, see eq. (2.4) with eq. (2.1) shows that the RG results for the persistence length L_p are not compatible with the definition using the tangent correlation function. This raises the general question which of the definitions should be preferred.

2.3 Model

A discretization of the WLC Hamiltonian (1.2) should preserve its local inextensibility. In addition, we want to use a discretized Hamiltonian which is locally invariant with respect to full rotations of single tangent vectors $\mathbf{t}$, i.e. to a translation of any angular coordinate of the corresponding hypersphere by 2π – in addition to the global rotational symmetry of the polymer as a whole. A suitable discrete model is an inextensible semiflexible chain model as given by [82, 32]

$$\mathcal{H}_{\mathrm{dwlc}}\{\mathbf{t}_i\} = \frac{\kappa_0}{b_0} \sum_{i=1}^{M} (1 - \mathbf{t}_i \cdot \mathbf{t}_{i-1}), \quad \text{with } \mathbf{t}_i^2 = 1, \tag{2.5}$$

with M bonds or chain segments of fixed length b_0. The semiflexible chain model is equivalent to the one-dimensional classical Heisenberg model (except for the first term, which represents a constant energy term) describing a one-dimensional chain of classical spins, cf. Fig. 2.2.

The partition sum reads

$$\mathcal{Z}_M = \left(\prod_{j=0}^{M} \int d\mathbf{t}_j \right) \exp[-\mathcal{H}_{\mathrm{dwlc}}\{\mathbf{t}_j\}/T] = \left(\prod_{j=0}^{M} \int d\mathbf{t}_j \right) \prod_{i=1}^{M} T_{i,i-1}, \tag{2.6}$$

where we have introduced the transfer matrix

$$T_{i,i-1} = \exp\left[-K_0(1 - \mathbf{t}_i \cdot \mathbf{t}_{i-1})\right] \equiv \exp\left[h^{(0)}(\mathbf{t}_i \cdot \mathbf{t}_{i-1}, K_0)\right], \qquad (2.7)$$

with $K_0 \equiv \kappa_0/b_0 T$ and $\int d\mathbf{t}_i = 1$. Equation (2.7) defines the interaction function $h^{(0)}(x)$ between neighboring tangents. For the following calculations it proves very advantageous that the transfer matrix (2.7) can be expanded in terms of the complete set of its eigenfunctions $\psi_k(\mathbf{t}_i)$. In order to find these eigenfunctions ψ_k and the corresponding eigenvalues λ_k, one has to solve the integral equation

$$\int d\mathbf{t}_i T_{i,i-1} \psi_k(\mathbf{t}_i) = \lambda_k \psi_k(\mathbf{t}_{i-1}). \qquad (2.8)$$

We can parametrize the tangent vectors via the polar/spherical coordinates θ_i and ϕ_i and express the scalar product of unit tangent vectors in the interaction $h^{(0)}(\mathbf{t}_i \cdot \mathbf{t}_{i-1}, K_0)$ using the azimuthal angle difference as

$$\begin{aligned}
\mathbf{t}_i \cdot \mathbf{t}_{i-1} &= \cos(\theta_{i,i-1}) \equiv \cos(\theta_i - \theta_{i-1}) , \\
\mathbf{t}_i \cdot \mathbf{t}_{i-1} &= \cos(\Theta_{i,i-1}) \equiv \cos\theta_i \cos\theta_{i-1} + \sin\theta_i \sin\theta_{i-1} \cos(\phi_i - \phi_{i-1})
\end{aligned} \qquad (2.9)$$

for the semiflexible polymer in the plane and in three-dimensional space, respectively. Then the left-hand side of (2.8) can be rewritten with the help of the expansions

$$e^{K_0 \cos\theta_{i,i-1}} = \sum_{m=-\infty}^{\infty} I_m(K_0) \, e^{im\theta_{i,i-1}} \qquad (2.10)$$

in two dimensions and

$$e^{K_0 \cos\Theta_{i,i-1}} = \sqrt{\frac{\pi}{2K_0}} \sum_{l=0}^{\infty} (2l+1) \, I_{l+1/2}(K_0) \, P_l(\cos\Theta_{i,i-1}) \qquad (2.11)$$

in three dimensions, where $I_k(x)$ denotes the modified Bessel function of the first kind and $P_l(x)$ the Legendre polynomials [83]. For $d = 2$, one immediately sees that the eigenfunctions are simply exponentials $e^{im\theta_i}$, whereas, by making use of the addition theorem

$$P_l(\cos\Theta_{i,i-1}) = \frac{4\pi}{2l+1} \sum_{m=-l}^{l} Y_{lm}^*(\theta_i, \phi_i) \, Y_{lm}(\theta_{i-1}, \phi_{i-1}) \qquad (2.12)$$

and the orthogonality condition

$$\int_0^{2\pi} \int_0^{\pi} d\Omega \, Y_{lm}^*(\theta, \phi) \, Y_{l'm'}(\theta, \phi) = \delta_{l,l'} \delta_{m,m'} \qquad (2.13)$$

21

of spherical harmonics $Y_{lm}(\theta, \phi)$, the eigenfunctions for $d = 3$ are found to be $\sqrt{4\pi}Y_{lm}(\theta_i, \phi_i)$. In total, the transfer matrix can be expanded as

$$T_{i,i-1} = \sum_{m=-\infty}^{\infty} \lambda_m^{(0)} e^{im\theta_{i,i-1}}, \quad \lambda_m^{(0)}(K_0) = e^{-K_0} I_m(K_0) \tag{2.14a}$$

in two dimensions and

$$T_{i,i-1} = \sum_{l=0}^{\infty}(2l+1)\lambda_l^{(0)} P_l(\cos\Theta_{i,i-1}), \quad \lambda_l^{(0)}(K_0) = \sqrt{\frac{\pi}{2K_0}}\, e^{-K_0} I_{l+1/2}(K_0)$$

$$\tag{2.14b}$$

in three dimensions. In the remainder of this chapter, the sums $\sum_{m=-\infty}^{\infty}$ for $d = 2$ and $\sum_{l=0}^{\infty}(2l+1)$ for $d = 3$ are abbreviated by $\sum_{n}^{(d)}$.

For simplicity, we restricted our analysis to $d = 2$ and $d = 3$ spatial dimensions, but our results can easily be generalized to arbitrary dimensions d: The transfer matrix is then expanded in Gegenbauer polynomials and the eigenvalues $\lambda_k^{(0)}$ are proportional to modified Bessel functions $I_{k+d/2-1}(K_0)$. It should also be mentioned, that for an arbitrary interaction function $h(\mathbf{t}_i \cdot \mathbf{t}_{i-1}, K)$ depending on an arbitrary parameter K we can expand the transfer matrix in the same sets of functions as in (2.14), which defines eigenvalues e.g. $\lambda_m = \lambda_m(K)$ in $2d$ and $\lambda_l = \lambda_l(K)$ in $3d$.

The partition sum and tangent-tangent correlations may be calculated exactly for open and periodic boundary conditions as was done, e.g., in $d = 3$ by Fisher [84] and Joyce [85]. For arbitrary dimension d the tangent-tangent correlation for open boundary conditions is simply given by

$$\langle \mathbf{t}(0) \cdot \mathbf{t}(L)\rangle = \left[\lambda_1^{(0)}(K_0)/\lambda_0^{(0)}(K_0)\right]^{L/b_0}, \tag{2.15}$$

whereas for closed chains the same result is obtained only asymptotically for L much bigger than b_0. In the continuum limit of small b_0 or large K_0, one can replace the Bessel functions contained in the eigenvalues $\lambda_k^{(0)}$, see (2.14), by their asymptotic form [83]

$$I_k(x) \approx (x/2\pi)^{-1/2} \exp[x - (k^2 - 1/4)(2x)^{-1}] \quad \text{for large } x \tag{2.16}$$

leading to the result already found for the WLC model (2.1).

2.4 Renormalization procedure

The real-space functional RG analysis for the semiflexible chain (2.5) proceeds in close analogy to the one-dimensional Heisenberg model [86] and similarly to
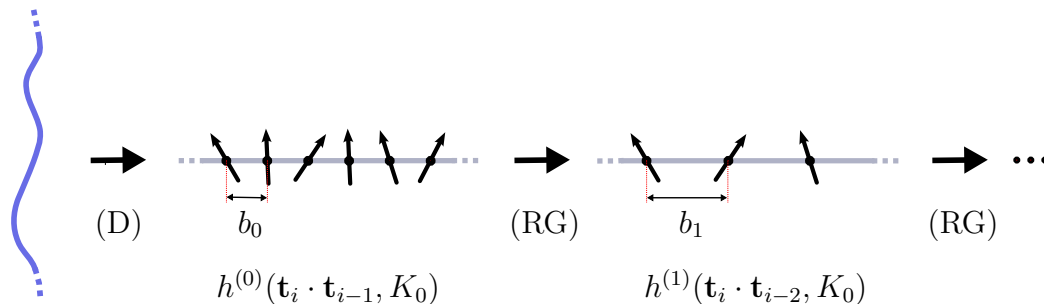
Figure 2.2: Schematic discretization and renormalization procedure. As a first step (D), the contour of the semiflexible polymer is represented by a semiflexible chain (or classical Heisenberg chain) with fixed bond length b_0. The tangent vector $\mathbf{t}_n \equiv \mathbf{t}(s_n)$ at the position $s_n = n b_0$ on the contour of the semiflexible polymer is assigned to the site n on the chain. The interaction function between neighboring tangents is denoted by $h^{(0)}$ and depends on their scalar product and the dimensionless parameter $K_0 = \kappa_0/b_0 T$. This interaction is recursively renormalized. At each RG step (RG), every second tangent degree of freedom is eliminated leading to an effective interaction $h^{(1)}$ on length scales $b_1 = 2b_0$.

the Ising-like case where the $\mathbf{t}_i$'s are confined to discrete values [87]. Similar real-space functional RG methods have also been used to study wetting transitions or the unbinding transitions of strings [88, 89].

The principle idea of the renormalization procedure is to extract the long range behavior of a system by integrating recursively over short range fluctuations. This means in the present case, that at each RG step, every second tangent degree of freedom is eliminated as illustrated in Fig. 2.2. The resulting effective interaction describing the system on large length scales is expressed in such a way, that it has the same algebraic form as the original interaction, but with new parameters, plus a constant energy shift, which is physically irrelevant. Therefore, all changes caused by integration are absorbed in the set of *renormalized* system parameters, which encode how the system behaves on different length scales.

We introduce a general transfer matrix

$$T_{i,i-1} = \exp\left[h(\mathbf{t}_i \cdot \mathbf{t}_{i-1}, K)\right] \tag{2.17}$$

where $h = h(u, K)$ defines an *arbitrary* interaction function depending on the scalar product of adjacent tangents $u = \mathbf{t}_i \cdot \mathbf{t}_{i-1}$ and the parameter K. We start the RG procedure with an initial value $K = K_0$ and an initial interaction function $h^{(0)}(u, K_0) = -K_0(1-u)$, see eq. (2.7). Accordingly, the eigenvalues are initially $\lambda_m(K_0) = \lambda_m^{(0)}(K_0)$ and $\lambda_l(K_0) = \lambda_l^{(0)}(K_0)$. The explicit expressions for the eigenvalues are given by (2.14).

Integration over one intermediate tangent $\mathbf{t}'$ between $\mathbf{t}$ and $\mathbf{t}''$ defines a recursion formula resulting in a new interaction function $h^{(1)} = h^{(1)}(u, K_0)$ and an energy shift $g^{(0)}$ given by

$$\exp[h^{(1)}(\mathbf{t}\cdot\mathbf{t}'', K_0) + g^{(0)}(K_0)] = \int d\mathbf{t}' \, \exp[\, h^{(0)}(\mathbf{t}\cdot\mathbf{t}', K_0) + h^{(0)}(\mathbf{t}'\cdot\mathbf{t}'', K_0)], \quad (2.18)$$

where the energy shift $g^{(0)}$ is determined by the condition that $h^{(1)}(1, K_0) = h^{(0)}(1, K_0) = 0$, i.e. the energy is shifted in such a way that the interaction term is zero for a straight polymer. This leads to

$$\exp[g^{(0)}(K_0)] = \int d\mathbf{t} \, \exp[2\, h^{(0)}(\mathbf{t} \cdot \mathbf{t}', K_0)],$$

$$\exp[h^{(1)}(\mathbf{t} \cdot \mathbf{t}'', K_0)] = \exp[-g^{(0)}(K_0)] \int d\mathbf{t}' \, \exp[\, h^{(0)}(\mathbf{t} \cdot \mathbf{t}', K_0) + h^{(0)}(\mathbf{t}' \cdot \mathbf{t}'', K_0)].$$
$$(2.19)$$

The recursion relations (2.18) and (2.19) are exact and can be used to obtain an exact expression for the eigenvalues $\lambda_k^{(N)}$ after N iterations, as given by

$$\lambda_k^{(N)} = \left[\lambda_k^{(N-1)}\right]^2 \Big/ \left\{ \sum_n^{(d)} [\lambda_n^{(N-1)}]^2 \right\} = \left[\lambda_k^{(0)}\right]^{2^N} \Big/ \left\{ \sum_n^{(d)} [\lambda_n^{(0)}]^{2^N} \right\}. \quad (2.20)$$

It should be mentioned, that the tangent correlation function $\langle \mathbf{t}(0) \cdot \mathbf{t}(L) \rangle$, with $L = 2^N b_0$, in (2.15) can now also be calculated by performing N recursion steps until the tangent vectors are nearest neighbors and, therefore, can be expressed in terms of the new eigenvalues $\lambda_k^{(N)}$, as

$$\langle \mathbf{t}(0) \cdot \mathbf{t}(L) \rangle = \left[\lambda_1^{(N)}(K_0)/\lambda_0^{(N)}(K_0)\right] = \left[\lambda_1^{(0)}(K_0)/\lambda_0^{(0)}(K_0)\right]^{2^N} \quad \text{with } L/b_0 = 2^N. \quad (2.21)$$

In general, the new and the old interaction $h^{(1)}(u, K_0)$ and $h^{(0)}(u, K_0)$ will differ in their functional structure, see for instance Fig. 2.3. Thus, the renormalization of the parameter K_0 cannot be carried out in an exact and simple manner as for one-dimensional Ising-like models with discrete spin orientation [87]. The only fixed point function of the recursion (2.18) is independent of u, i.e. $h^*(u, K_0) = 0$ because of $h^*(1, K_0) = 0$. This result, together with the condition $h^{(1)}(1, K_0) = 0$, which is imposed at every RG step, suggests that the function $h^{(1)}(u, K_0)$ can be approximated by

$$h^{(1)}(u, K_0) \simeq -K_1(K_0)\,(1-u) \quad \text{for } u = \mathbf{t} \cdot \mathbf{t}'' \simeq 1, \quad (2.22)$$

i.e. by a linear function as long as the scalar product $u = \mathbf{t} \cdot \mathbf{t}''$ is close to one, i.e. sufficiently close to the straight configuration. This approximation should
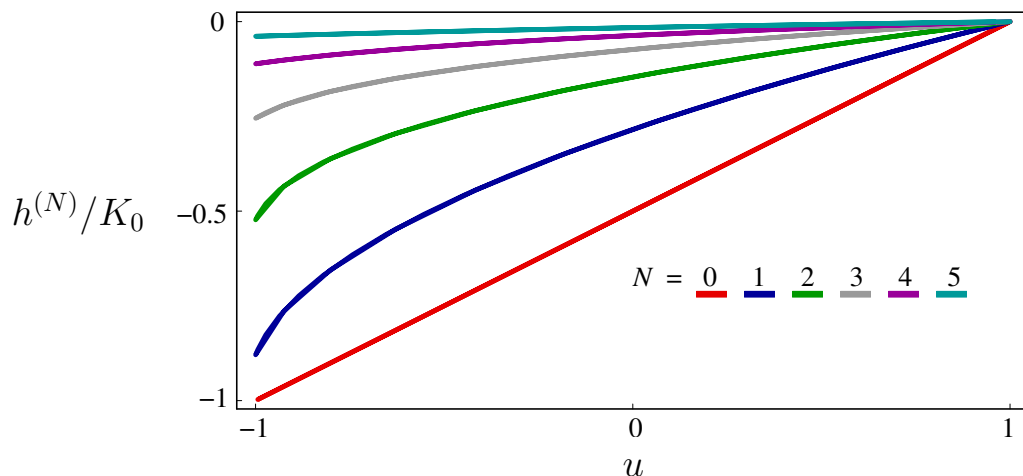
Figure 2.3: Interaction $h^{(N)}$ divided by K_0 as a function of the tangent scalar product $u \equiv \mathbf{t} \cdot \mathbf{t}''$ for $d = 2$ and $K_0 = 10$ after $N = 0, ..., 5$ iterations. The plot illustrates, that as long as $u \approx 1$, the renormalized interactions $h^{(N)}$ can be approximated by linear functions $h^{(N)}(u) \simeq -K_N(1 - u)$. The absolute value of the slope of each line is identified with the renormalized parameter K_N after N recursion steps.

improve when the whole function $h^{(1)}(u, K_0)$ becomes small upon approaching the fixed point $h^*(u, K_0) = 0$ after many iterations, i.e. on large length scales. Using the approximation (2.22), $K_1(K_0)$ is defined by the slope of $h^{(1)}(u, K_0)$ at $u = 1$,

$$K_1(K_0) \equiv \left. \frac{dh^{(1)}(u, K_0)}{du} \right|_{u=1} = \left. \frac{d}{du} \exp \left[h^{(1)}(u, K_0) \right] \right|_{u=1} , \quad \text{with } u = \mathbf{t} \cdot \mathbf{t}''. \quad (2.23)$$

Equivalently, one could expand the explicit expression for $h^{(1)}(x, K_0)$ given by (2.19) and the right hand side of (2.22) for small tangent angles and compare the coefficients. In order to extract the renormalized bending rigidity κ_1 from the result for K_1, one has to take into account that K_1 also contains the new bond length $b_1 = 2b_0$, which increases by a factor of 2 at each decimation step. Therefore,

$$\kappa_1(K_0) = 2b_0 T \, K_1(K_0). \quad (2.24)$$

Using this procedure we can calculate the renormalized bending rigidity κ_N after N iterations in 2d and 3d starting from the exact expressions (2.20) for the eigenvalues. Inserting the renormalized eigenvalues into (2.14), gives the transfer matrix that contains the exact interaction function after N iterations in 2d and

25
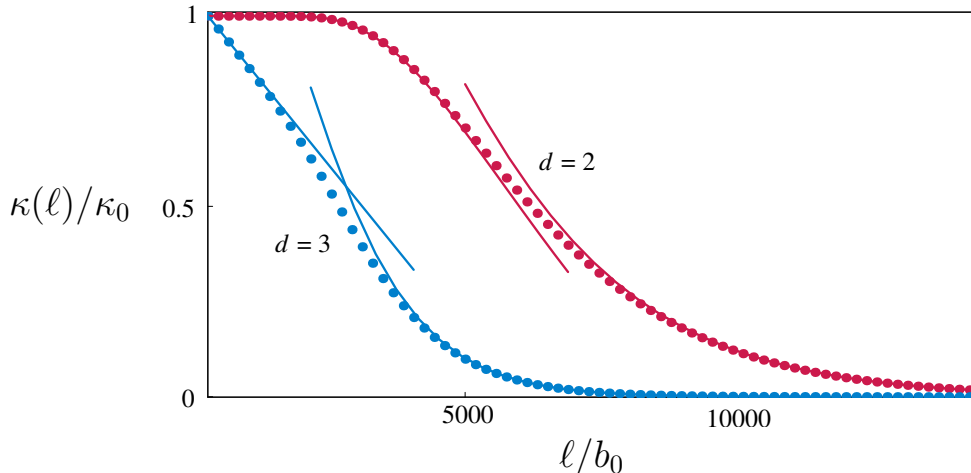
Figure 2.4: Renormalized $\kappa(\ell)/\kappa_0$ as a function of $\ell/b_0 = 2^N$ for $K_0 = 1000$ for $d = 2$ (red) and $d = 3$ (blue) according to the recursion relation (2.25). The lines show the asymptotic behavior for $\ell \gg \kappa_0/T$ and $\ell \ll \kappa_0/T$ according to eqs. (2.26) and (2.28), respectively.

3d. Taking the derivative according to (2.23) and applying the rescaling (2.24) finally yields the result

$$\frac{\kappa_N}{\kappa_0} = \frac{2^N}{K_0} \left\{ \sum_n^{(d)} \left[\lambda_n^{(0)}(K_0) \right]^{2^N} A_n^{(d)} \right\} \Big/ \left\{ \sum_n^{(d)} \left[\lambda_n^{(0)}(K_0) \right]^{2^N} \right\}, \qquad (2.25)$$

with $A_n^{(2)} \equiv n^2$ and $A_n^{(3)} \equiv \frac{1}{2}n(n+1)$. In the following we will interpret κ_N as a continuous function $\kappa(\ell)$ of the length scale ℓ by replacing the rescaling factor $2^N = b_N/b_0$ by the continuous parameter ℓ/b_0.

2.5 Persistence length

The sums in the expressions for the effective bending rigidity (2.25) can be computed numerically. Fig. 2.4 displays the results for $\kappa(\ell)/\kappa_0$ as a function of ℓ/b_0 for $K_0 = 1000$ in 2d and 3d. The value $K_0 = 1000$ is appropriate for a semiflexible polymer with $\kappa_0/T = 10\,\mu\text{m}$ and a bond length $b_0 = 10\,\text{nm}$, which is close to experimental values for F-actin [9, 7]. For DNA, appropriate values are $\kappa_0/T \simeq 50\,\text{nm}$ and $b_0 \simeq 0.3\,\text{nm}$ and, thus, $K_0 \simeq 150$.

As long as ℓ is small, κ decays almost linearly in $d = 3$, which is also in qualitative agreement with the result (2.2) from the RG of the nonlinear σ-model.

In contrast to the non-linear σ-model, κ is also renormalized in two dimensions, although compared to $d = 3$ the decay is much slower at small length scales. This qualitative difference is due to the following important difference between the Heisenberg and the nonlinear σ-model: Parametrizing the WLC model (1.2) via tangent angles leaves only quadratic terms $\propto (\theta_{i,i-1})^2$, whereas the discrete semiflexible chain (2.5) gives terms $\propto 1 - \cos(\theta_{i,i-1})$, which represent the full expansion of the cosine and are invariant with respect to a translation of any angular coordinate of the corresponding hypersphere by 2π.

As ℓ increases, $\kappa(\ell)$ approaches zero only asymptotically. Therefore, the definition of the persistence length as length scale where the renormalized κ vanishes, $\kappa(L_p) = 0$ – which is usually used for fluid membranes – would always give an *infinite* result. We propose not to ask at which length scale the renormalized κ reaches zero, but rather *how* it reaches zero. For $\ell \geq b_0 K_0 = \kappa_0/T$ the sums in (2.25) converge fast and one has to include only the first few terms for accurate results. In fact, one can take again the continuum limit of small b_0 or large K_0 and use the asymptotic form (2.16) for the Bessel functions contained in the eigenvalues $\lambda_k^{(0)}$, see (2.14). This is justified for sufficiently large $K_0 \gtrsim 100$, which is fulfilled by semiflexible polymers like F-actin ($K_0 \simeq 1000$) or DNA ($K_0 \simeq 150$). Using this asymptotics we find $(\lambda_m^{(0)}(K_0))^{\ell/b_0} \sim e^{-m^2\ell/2b_0 K_0}$ for $d = 2$ and $(\lambda_l^{(0)}(K_0))^{\ell/b_0} \sim e^{-l(l+1)\ell/2b_0 K_0}$ for $d = 3$. Moreover, we may expand (2.25) as a power series in $e^{-\ell T/\kappa_0}$ and obtain

$$
\begin{aligned}
\kappa(\ell)/\kappa_0 &\approx (\ell T/\kappa_0) \left(2e^{-\ell T/2\kappa_0} - 4e^{-\ell T/\kappa_0} + 8e^{-3\ell T/2\kappa_0} - \dots\right) \quad \text{for} \quad d = 2, \\
\kappa(\ell)/\kappa_0 &\approx (\ell T/\kappa_0) \left(3e^{-\ell T/\kappa_0} - 9e^{-2\ell T/\kappa_0} + 42e^{-3\ell T/\kappa_0} - \dots\right) \quad \text{for} \quad d = 3.
\end{aligned}
\tag{2.26}
$$

The characteristic length scales in the expansions are $2\kappa_0/T$ in $d = 2$ and κ_0/T in $d = 3$, which are, thus, a natural definition for the persistence length L_p. For general dimensionality d, the exponent of the first term is determined by the order of the Bessel function appearing in the eigenvalue. Thus the RG calculation leads to a persistence length

$$
L_p = \frac{2\kappa_0}{T(d-1)},
\tag{2.27}
$$

which agrees perfectly with the result (2.1) based on the tangent correlation function.

Our definition based on the large-scale asymptotics of the exact RG flow is qualitatively different from the definition (2.3) used in perturbative RG calculations. While the result (2.2) from the nonlinear σ-model is only valid for small length scales $\ell \ll \kappa_0/T$, where $\kappa(\ell)$ is close to κ_0, the expansion (2.26) describes the region $\ell \gg \kappa_0/T$. Indeed, taking the expansion of the RG flow (2.25) for

$\ell \ll \kappa_0/T$, that is

$$\begin{aligned}
\kappa(\ell)/\kappa_0 &\approx 1 - (8\pi^2\kappa_0/\ell T)e^{-2\pi^2\kappa_0/\ell T} + \mathcal{O}(\ell e^{-4\pi^2\kappa_0/\ell T}) \quad \text{for} \quad d = 2 \\
\kappa(\ell)/\kappa_0 &\approx 1 - (\ell T/6\kappa_0) - \mathcal{O}(\ell^2 T^2/\kappa_0^2) \qquad\qquad\qquad \text{for} \quad d = 3 \ ,
\end{aligned} \tag{2.28}$$

and defining L_p by the exponential decay length in two dimensions, respectively, by the linear term in three dimensions leads to a persistence length, which is considerably bigger than the value (2.27) found above. Hence it is not surprising that the two computations (2.2) and (2.26) yield different results. The slow exponential decay in the expansion (2.28) for $d = 2$ is reminiscent of the non-renormalization of κ in the non-linear σ-model, see eq. (2.2), and leads to a "plateau" in the numerical result for $\kappa(\ell)/\kappa_0$ for $\ell \ll \kappa_0/T$ in Fig. 2.4.

2.6   Conclusion

In this chapter, we have presented a definition of the persistence length L_p of a semiflexible polymer or one-dimensional fluid membrane based on the large scale behavior of the RG flow of the bending rigidity κ, as obtained from a functional real-space RG calculation. Our result (2.27) for L_p generalizes the conventional definition based on the exponential decay of a particular two-point tangent correlation function and gives identical results for L_p. The RG flows (2.25) or (2.26) allow us to follow the behavior of a semiflexible polymer from a stiff polymer on short length scales to an effectively flexible polymer on large length scales quantitatively as a function of the length scale. On large length scales, our functional RG gives qualitatively different results from perturbative RG techniques, which have been used for the closely related problem of fluid membranes [73, 74, 75, 76, 77, 78, 79, 80] and which we also applied to the one-dimensional semiflexible polymer. The generalization of our renormalization approach to two-dimensional fluid membranes is complicated by the more involved differential geometry of these two-dimensional objects and remains an open issue for future investigation. Our results indicate that also for two-dimensional fluid membranes the asymptotic large scale RG flow of the bending rigidity is needed in order to identify their persistence length.

Chapter 3

Semiflexible polymer rings on structured substrates

We investigate morphologies of semiflexible polymer rings, such as circular nanotubes or DNA, which are adsorbed onto topographically or chemically structured substrate surfaces. We classify all equilibrium morphologies for two striped surface structures, (i) a topographical surface channel and (ii) a chemically structured surface domain. For both types of stripes we find four equilibrium shapes: a round toroidal, a confined elongated, and two shapes containing bulges.
We determine the complete morphology diagram as a function (i) of the contour length of the polymer divided by the stripe width and (ii) of the ratio of adhesive strength to bending rigidity (reduced adhesion strength).
For more complex geometries consisting of several topographical stripes we find a cascade of transitions between elongated shapes. Finally, we compare our findings to ring condensation by attractive interactions.

3.1   Introduction

Many applications in (bio-)nanotechnology, such as the construction of electric devices or sensors containing nanotubes, require immobilization, controlled shape manipulation, and positioning of semiflexible polymers. Adsorption on substrates is the simplest technique to immobilize single polymers and a first step towards further manipulation and visualization of structure details using, e.g. modern scanning probe techniques [46, 90]. Furthermore, the *controlled* adsorption of single polymers at predefined positions, e.g. at electrodes, has been achieved by using chemically structured substrates [91, 48, 92, 93], see Fig. 3.1. The substrate patterns used in these experiments are composed of domains of arbitrary shape, which are characterized by a greater binding affinity compared to the surrounding substrate. Theoretically, this effect can be described by a laterally modulated adhesion potential, where, in the simplest version, the polymer gains a constant adsorption energy $W < 0$ per unit length.

For manipulation, control over the shape of the adsorbed polymer, which is for example a nanotube or DNA, is needed. Typical shapes of semiflexible and
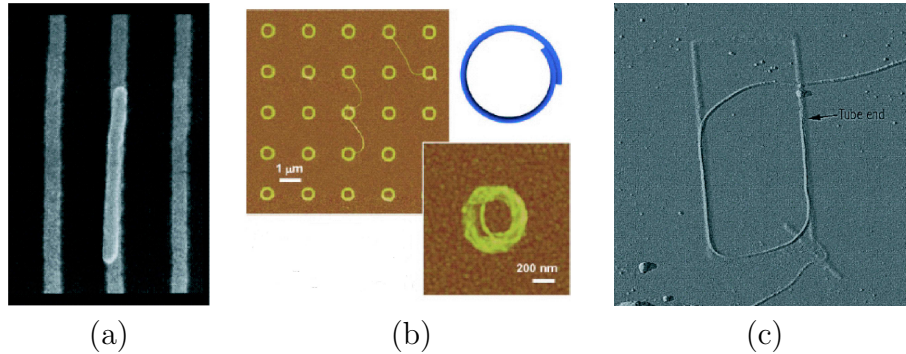
Figure 3.1: Three experimental examples for controlled adsorption of nanotubes on structured substrates are shown: (a) The electron micrograph of a multi-walled nanotube (light-grey) of length $\simeq 0.6\,\mu$m covered with a surfactant shell completely adsorbed to a hydrophobic electrode (grey) with a width of $\simeq 60$ nm on a silicon wafer [48]. (b) The AFM image of single-walled nanotubes of length $\simeq 1 - 3\,\mu$m that are forced to form a coiled shape by hydrophilic ring domains with a width of 170 nm and a maximal diameter of 650 nm on a gold substrate [93]. (c) The AFM image of a single-walled nanotube (sharp grey contour) of length $\simeq 1\,\mu$m adsorbed to NH_2-functionalized lines (blurred grey) on a silicon wafer [92].

flexible polymers are fundamentally different: While on a homogeneous substrate, flexible polymers are governed by conformational entropy and adsorb in random coil configurations, open (closed) semiflexible polymers with large persistence lengths are dominated by their bending rigidity and adsorb in a straight (circular) configuration, as is nicely demonstrated e.g. in [91].

In Fig. 3.1 three experimental examples of an open nanotube adsorbed to a patterned substrate are shown. In the first case (a), the striped structure (grey) does not interfere with the straight conformation of the nanotube (light-grey), which is favored by bending energy. By contrast, in the second case (b), it has to form a tightly wound coil (yellow) to bind with its full contour length L to the ring domain of maximal diameter a (invisible). This latter configuration is only stable, if the cost of bending energy E_b is compensated by the gain in adsorption energy E_{ad}, i.e. for

$$E_b + E_{ad} \simeq 2\frac{\kappa L}{a^2} - WL \leq 0 \ \ \text{or} \ \ \frac{Wa^2}{\kappa} \geq 2. \tag{3.1}$$

Also in the last case (c), one can see clearly, that the nanotube (sharp grey contour) bends to align well with the two parallel stripes (blurred grey).

In this chapter, we explore the possibility to gain such shape control for semiflexible polymer rings using simple striped surface structures, which, in a sense,
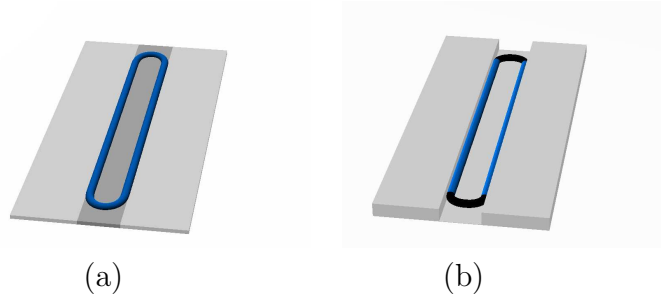
(a)   (b)

Figure 3.2: Adsorbed circular polymer on a striped surface containing (a) a chemically structured surface domain of width a_{do} and (b) two topographical surface steps forming a channel of width a_{st}.

is the counterpart to the setup depicted in Fig. 3.1(b). Examples of such circular semiflexible polymers are provided by carbon nanotubes [12, 5], DNA minicircles [10], filamentous actin [13], and amyloid fibrils [11]. The substrate patterns studied in the following correspond to a single chemically striped domain, see Fig. 3.2(a), and to a single topographical surface channel, see Fig. 3.2(b), but also to periodic topographical structures, which provide a simple model for the interaction between a polymer and the atomic lattice structure of substrate surface. It turns out, that a shallow topographical step of a certain width has an effect very similar to a thin adhesive stripe as shown in Fig. 3.1(a) and (c), because the polymer is attracted to the surface steps. Such topographical surface steps have been employed in recent manipulation experiments on semiflexible polymer rings [94].

We find that, for persistence lengths larger than the stripe width, the competition between the bending rigidity of the circular polymer and its attraction to the striped domain allows a controlled switching between four distinct stable morphologies, see Figs. 3.4 and 3.13: Apart from a weakly bound almost circular shape and a strongly bound confined shape, bulged intermediate shapes become stable for large contour lengths. Our results are summarized in the full morphological diagrams for semiflexible ring shapes depending on the size of the ring compared to the size of the structure as well as the material parameters, namely, the bending rigidity κ and the adhesion energy gain W. This analysis can be used to (i) control the ring shape and (ii) analyze material properties of the substrate or the semiflexible polymer ring experimentally. Flexible polymer rings, on the other hand, exhibit random coil configurations and such morphological transitions are absent.

Interestingly, the conformation of the nanotube enforced by the ring domain in Fig. 3.1(b) strongly resembles the compact toroidal condensates observed for

DNA [14, 37, 95, 96] or actin filaments [13, 97]. The condensation of DNA occurs in living cells and viruses and, on the other hand, it has potential technical applications in gene delivery for gene transfer. In poor solvent, in the presence of condensing agents or depletion forces, polymer-polymer contacts become favorable, but the bending rigidity of a semiflexible polymer inhibits its collapse towards a tightly packed globular structure, which is common for flexible polymers. It has been reported, e.g. in [98], that this phenomenon can also be induced on substrates that are treated with cationic silanes. The resulting morphological transitions into highly ordered rodlike or toroidal shapes [99] are closely related to the transitions on striped surfaces, as they are likewise caused by the competition between stiffness and attractive interactions.

This chapter is organized as follows. In Section 3.2, we begin with the analysis of the equilibrium morphologies of a ring adhered to a substrate containing a topographical channel, since only for this architecture also an analytical treatment is possible. Therefore, our model for the adhesion potential caused by the topographical channel and the general minimization procedure are introduced, which is followed by the analytical and numerical calculations. We obtain a projection of the energy landscape, analyze its local minima and summarize our findings in a morphological diagram. In the end of the section, the influence of thermal fluctuations is discussed. In the same manner, the system with the chemical domain is analyzed numerically in Section 3.3. As an example of more complicated structures, our results are generalized to substrates with periodic surface stripes. Finally, we compare our findings for morphological transitions of semiflexible rings on structured substrates to the condensation of a semiflexible ring by attractive polymer-polymer interactions.

3.2   Topographical surface channel

3.2.1   Substrate model

We consider a planar substrate in the xy-plane that contains two parallel topographical surface steps at $x = \pm a_{st}/2$ forming an infinitely long surface channel of width a_{st}, see Fig. 3.3 (left). A semiflexible polymer ring, characterized by the bending rigidity κ and the fixed contour length L, gains an overall adsorption energy $W_{st} < 0$ per polymer length by adsorbing to the substrate surface. At the edges of the surface channel the adsorption energy is doubled, since the semiflexible polymer can bind to two adjacent surfaces at the same time. We will refer to this extra energy contribution as the adsorption energy and omit the constant energy offset throughout this chapter. The resulting effective lateral adsorption
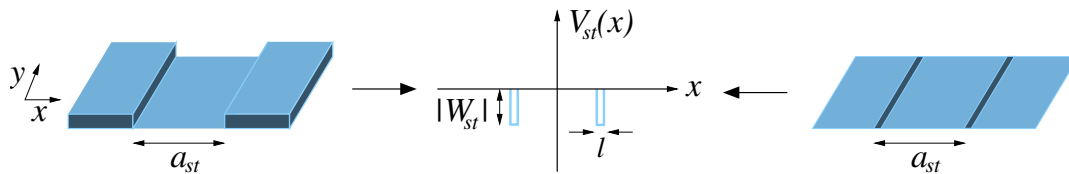
Figure 3.3: Schematic image of a topographical surface channel (left) and the corresponding adsorption potential $V_{st}(x)$ (middle). The distance between the two steps is denoted by a_{st}. At the edges, a polymer gains the additional adsorption energy $W_{st} < 0$ per length, because it can bind to two surfaces, which is reflected in $V_{st}(x)$ by two narrow square wells at $x = \pm a_{st}/2$. The widths of the square wells l is determined by the range of the adsorption potential. A substrate with two thin chemically modified lines (right) induces a potential of the same shape, but there W_{st} depends on the chemical composition of the adhesive lines.

potential can be described by

$$
V_{st}(x) = \begin{cases} W_{st} & \text{for } |x \pm a_{st}/2| < l/2, \\ 0 & \text{otherwise,} \end{cases} \tag{3.2}
$$

as shown in Fig. 3.3 (middle). The range of the adsorption potential V_{st} is denoted by l, which is taken to be of the order of the polymer diameter D and small compared to the channel width, $l \ll a_{st}$. It is also equivalent to the range of the overall adsorption potential perpendicular to the substrate surface. Furthermore, we are solely interested in surface steps of a height comparable to the polymer diameter D, as can be fabricated by conventional nanolithographic methods. Then, small energy corrections arising if the polymer crosses the surface steps can be neglected. The resulting confined shapes are therefore not a consequence of pure geometric constraints, but of the adsorption energy gain induced by the surface steps. It should be mentioned, that a potential of the *same* shape is generated by a substrate containing two thin chemically modified lines of width l, which are characterized by an adhesion contrast W_{st} and which are located at a distance a_{st}, see Fig. 3.3 (right)[1]. Therefore, all results that are derived for the topographical channel in this section also apply to a ring that is adsorbed to such a substrate pattern.

---

[1]Note that, in this case, W_{st} is tuned by the chemical composition of the stripes and is not simply equal to the adhesion strength of the surrounding substrate.

3.2.2   Minimization procedure

We will first focus on polymer morphologies at $T = 0$ and discuss the effect of thermal fluctuations at the end of this section. Moreover, the overall adhesion is assumed to be so strong, that the polymer is firmly adsorbed to the substrate surface and thus the ring conformations are essentially planar. However, the motion of the semiflexible polymer along the substrate should be unhindered, so that kinetic trapping effects can be excluded and the ring always equilibrates. Such conditions are found experimentally, e.g. for DNA adsorbed to mica via electrostatic interactions [46].

With the above assumptions, for an adsorbed ring of length L and rigidity κ on a structured substrate of the type shown in Fig. 3.3, which is characterized by a_{st} and relative adsorption strength W_{st}, the Hamiltonian can be written in terms of the tangent angles $\theta(s)$ as

$$\mathcal{H}\{\theta(s)\} = \mathcal{H}_{\text{wlc}}\{\theta(s)\} + \int_0^L ds\, V_{st}(x). \qquad (3.3)$$

As before, the WLC Hamiltonian represents the bending energy of the ring, see (1.3), whereas, in the second term, the adsorption energy is calculated by integrating the laterally modulated adsorption potential (3.2) along the ring contour. Only polymer segments that are located at $|x \pm a_{st}/2| < l/2$ and oriented parallel to the y-axis can adhere to the surface pattern and actually give rise to a non-vanishing contribution to the integral, so that, if we refer to the total length of these adhered segments as the *adhered length* L_{st}, the adsorption energy is simply $-|W_{st}|L_{st}$. On the other hand, since the adhered segments are necessarily straight and, accordingly, $\partial_s\theta(s) = 0$, they do not contribute to the bending energy. As a consequence, the segments of an adhered ring can be divided into two categories, namely, straight adhered segments of length L_{st}, by which the ring *gains* adsorption energy, and curved non-adhered segments of length $L - L_{st}$, that *cost* bending energy. We express this observation in the Hamiltonian by writing

$$\mathcal{H}\{\theta(s), L_{st}\} = \mathcal{H}_{\text{wlc}}\{\theta(s), L - L_{st}\} - |W_{st}|L_{st}. \qquad (3.4)$$

By analyzing this Hamiltonian, it turns out, that only two control parameters, which are combinations of the four parameters L, κ, a_{st} and W_{st}, are actually needed to characterize the system. The first control parameter is the ratio between the contour length of the ring and the stripe width

$$\bar{L} \equiv \frac{L}{a_{st}} \qquad (3.5)$$

and the second one is the dimensionless *reduced adsorption strength*, namely

$$|w_{st}| \equiv \frac{|W_{st}|a_{st}^2}{\kappa} \qquad (3.6)$$

or alternatively

$$|\tilde{w}_{st}| \equiv \frac{|W_{st}|L^2}{\kappa} = |w_{st}|\bar{L}^2. \tag{3.7}$$

Both parameters $|w_{st}|$ and $|\tilde{w}_{st}|$ have advantages and disadvantages, which we will discuss later in detail, but as the results for either choice can easily transformed into the other, we will start with $|w_{st}|$.

At equilibrium, the ring will adjust its conformation to minimize its total energy, i.e. the above Hamiltonian. Two trivial, extreme cases are $|w_{st}| = 0$ corresponding to a substrate without structure, where the adsorbed semiflexible ring forms a circle with $L_{st} = 0$, and $|w_{st}|$ infinitely large, where a rectangular shape with adhered length $L_{st} = L - 2a_{st}$ is generated. For arbitrary values of the control parameters, the balance between the two energy contributions is tuned by exchange of contour length between adhered segments of length L_{st} and curved segments of length $L - L_{st}$. In this sense, the adhered length acts as internal parameter, that specifies an equilibrium state together with the control parameters, and is, thus, a convenient (but not the only possible) quantity to map the energy landscape of the system.

Therefore in a first step (i), we minimize the Hamiltonian $\mathcal{H}$ with respect to the tangent angles, while keeping L_{st} and, accordingly, the adhesion energy fixed, as

$$\delta_\theta \mathcal{H} = \delta_\theta \mathcal{H}_{\text{wlc}} \overset{!}{=} 0, \tag{3.8}$$

which yields the minimized bending energy as a function of the adhered length $E_b(L_{st})$. With this result, also the total energy as a function of the adhered length $E_{tot}(L_{st})$ for a given value of the adhesion strength W_{st} is easily deduced by including the adsorption energy

$$E_{tot}(L_{st}) = E_b(L_{st}) - |W_{st}|L_{st}. \tag{3.9}$$

This function represents the a projection of the full energy landscape onto the one-dimensional coordinate L_{st} for a particular choice of the control parameters of the system. In the following, we refer to this function as the *projected energy landscape*. It exhibits sometimes only one, but usually several minima, depending on the control parameters, which reflects the fact that the ring does not transform from a circle into a rectangle in a uniform manner, but rather displays various equilibrium morphologies, which are shown Fig. 3.4. Thereby, we will attribute the terms *metastable* and *stable* to morphologies that belong to the local and global minima, respectively.

In order to find the position L_{st} of these minima (for particular $\bar{L}$ and $|w_{st}|$), the Hamiltonian $\mathcal{H}$ is varied in a second step (ii) with respect to the adhered length,

$$\partial_{L_{st}} E_{tot}(L_{st}) = \partial_{L_{st}} E_b(L_{st}) - |W_{st}| \overset{!}{=} 0, \tag{3.10}$$
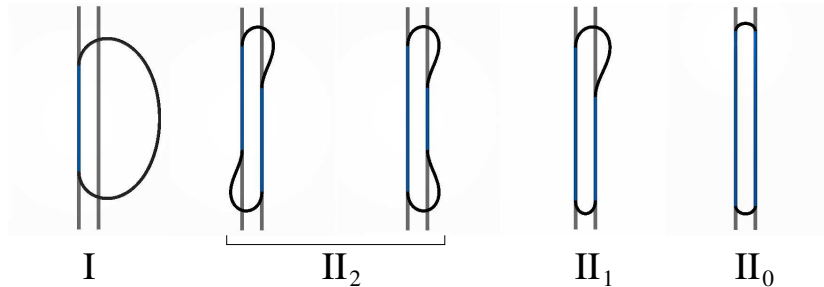
Figure 3.4: Top views of the four types of stable morphologies of a ring adhered to a surface with a topographical channel as obtained by energy minimization for contour lengths $L/a_{st} = 20$. There exist two realizations of conformation II_2, one being asymmetric (left) and one being symmetric (right) with respect to the horizontal axis. These two versions differ only in their stability, see Sections 3.2.6 and 3.2.7. The topographical surface steps are indicated by two thin grey lines and the ring segments that are adhered to the step edges are colored in blue.

which establishes a necessary condition for the local extrema of $E_{tot}(L_{st})$. The relation (3.10) implies that, in principle, for a particular shape one can read off the local slope of $E_b(L_{st})$, at which value of the adhesion strength $|W_{st}|$ the energy of this shape is extremal. Formally, this relation is used to eliminate L_{st} and, thus, to obtain the total energy of the local extrema of the projected energy landscape, which includes both minima and maxima. In this context, it is also necessary to examine the stability of the local extrema. A stability boundary is defined by the transition of a local minimum of the energy landscape into a saddle point. Therefore, at such a stability boundary a small change of the control parameters causes an abrupt change of the ring shape[2].

As a last step (iii), we study how the stable morphology, i.e. the position of the global minimum, changes with the control parameters and therefore divide the plane spanned by $\bar{L}$ and $|w_{st}|$ into regions representing the respective stable shapes of the system. For the *morphology boundaries* between these regions approximate relations between $\bar{L}$ and $|w_{st}|$ are found by demanding that the energies of the corresponding morphologies have to be equal. These relations are illustrated in the *morphological diagram*.

Finally, we would like to emphasize, that although some features of the system we are considering strongly resemble properties that are typical for thermodynamic systems, such as phase transitions etc., a single ring does *not* constitute a thermodynamic system. The problem is much better interpreted in the frame-

---

[2]Often the stability boundaries are directly included in the morphology diagram (see below), but for clarity, we chose to discuss the stability boundaries separately.

work of bifurcation theory, which was successfully applied to numerous elastic systems [100].

3.2.3   Analytical energy minimization

In this section, we minimize the bending energy of a ring for fixed adhered length L_{st} as described above. The relevant shapes are depicted in Fig. 3.4. There are obviously two different types of configurations, namely, those where the ring binds only to one of the step edges, denoted by I, and those where it binds to both step edges, denoted by II. The additional index for the conformations of type II refers to the number of *bulges*. Further, it should be mentioned, that all shapes shown in Fig. 3.4, except for the conformation II_0, are degenerate: A ring can assume shape I by adhering to either of the two edges. Moreover, the non-adhered segments of the ring can be located either to the left or to the right hand side of the edge the ring adheres to, which amounts in total to a degree of degeneracy of four. However, we would like to exclude those two configurations, where the ring does not overlap the second edge (unlike the one shown in Fig. 3.4), since they cannot undergo any morphological transitions, cf. the discussion in Section 3.2.6. The conformations with the same total energy as shape II_2 can be generated by flipping the conformation horizontally, whereas flipping shape II_1 horizontally and vertically leads in total to four equivalent conformations. Furthermore, there also exist two realizations of shape II_2, which have both bulges on the same side of the stripe and are, thus, symmetric with respect to the horizontal axis, see Fig. 3.4. The asymmetric and the symmetric version of shape II_2 differ only in their stability, see the discussion in Section 3.2.6. In general, we will refer to the asymmetric version as shape II_2, since it exists in a greater range of the control parameters, and distinguish between the two versions only in some places to point out differences.

The degree of degeneracy is irrelevant for the energy calculation, but it should influence the relative frequency of observing a particular conformation in experiments.

Conformations adhered to a single step edge (I)

For small $|L_{st}|$, the ring will attach only to one step edge and adopt the rather round toroidal configuration I, see Fig. 3.4. As the resulting shape is symmetric with respect to the horizontal axis, it is sufficient to calculate, say, only the upper half of the ring shape, as sketched in Fig. 3.5(a). The curved segment we are considering starts at the point where the ring adheres to the left edge ($s = L_{st}/2$) and ends where the contour and the symmetry axis cross each other ($s = L/2$). In order to assure that the final shape is smooth and closed, we

impose the boundary conditions $\theta(L_{st}/2) = 0$ and $\theta(L/2) = \pi$ at the ends and impose a constraint on the tangent vector component parallel to the channel, cf. Fig. 3.5(a), namely

$$\int_{L_{st}/2}^{L/2} ds \cos \theta(s) + \frac{L_{st}}{2} = 0, \tag{3.11}$$

which is enforced by a Lagrange multiplier called μ.

With these ingredients, we are ready to carry out the first step (i) of the minimization procedure. The first variation of (1.3) with respect to the tangent angles reads

$$\delta \mathcal{H} = \int_{L_{st}/2}^{L/2} ds \, \delta\theta \left\{ -\kappa \ddot{\theta} - \mu \sin \theta \right\} + \left[\kappa \dot{\theta} \, \delta\theta \right]_{L_{st}/2}^{L/2}, \tag{3.12}$$

where the first term yields the Euler-Lagrange equation for $\theta(s)$

$$\kappa \ddot{\theta}(s) + \mu \sin \theta(s) = 0, \tag{3.13}$$

while the second term vanishes, because the tangent angles are fixed at the end points of the curved segment we are considering. For our purpose, it is more convenient to use the integrated version of the Euler-Lagrange equation. It is obtained by multiplication with $\dot{\theta}(s)$ and integration over s, which leads to

$$\dot{\theta}(s) = \left\{ 2\frac{\mu}{\kappa} \left[\frac{c}{\mu} + \cos \theta(s) \right] \right\}^{1/2} \quad \text{or} \quad ds = d\theta \left\{ 2\frac{\mu}{\kappa} \left[\frac{c}{\mu} + \cos \theta(s) \right] \right\}^{-1/2}, \tag{3.14}$$

where c is an integration constant. A second integration of the above equation (3.14) yields

$$\begin{aligned}
\frac{L - L_{st}}{2} &= \left(\frac{\kappa}{2\mu} \right)^{1/2} \int_0^\pi d\theta \frac{1}{(q + \cos \theta)^{1/2}} \\
&= 2 \left(\frac{\kappa}{2\mu} \right)^{1/2} \frac{1}{(q-1)^{1/2}} K(2/[q-1])
\end{aligned} \tag{3.15}$$

with $q \equiv c/\mu$ and $K(x)$ being the complete elliptic integral of the first kind [83]. Then, by plugging the expressions of ds into the constraint (3.11), which gives

$$\frac{L_{st}}{2} = - \left(\frac{\kappa}{2\mu} \right)^{1/2} \int_0^\pi d\theta \frac{\cos \theta}{(q + \cos \theta)^{1/2}}, \tag{3.16a}$$

we find an implicit equation for q as a function of L_{st} using the integrated version of the Euler-Lagrange equation (3.15), namely

$$\frac{L_{st}}{L - L_{st}} = q \left\{ 1 - \left(1 - \frac{1}{q} \right) \frac{E(2/[q-1])}{K(2/[q-1])} \right\}, \tag{3.16b}$$

containing also the complete elliptic integral of the second kind $E(x)$ [83]. The solution of this equation can be calculated only numerically and was done using Newton's method, which is implemented in *Mathematica*® 5.2. The bending energy of the full conformation as a function of q and L_{st} can be calculated in a similar way as

$$
\begin{aligned}
E_b^{\mathrm{I}}(q, L_{st}) &= (2\kappa\mu)^{1/2} \int_0^\pi d\theta (q + \cos\theta)^{1/2} \\
&= 8\kappa(L - L_{st})^{-1} K(2/[q-1]) E(2/[q-1]).
\end{aligned}
\tag{3.17}
$$

In order to compute the bending energy E_b as a function of L_{st}, as depicted in Fig. 3.6(a), the corresponding value for q for each value L_{st} was determined using (3.16) and plugged into (3.17).

Conformations adhered to both step edges (II)

For $L_{st} \gtrsim L/2$, conformations, where the ring binds to both step edges, will become relevant. These shapes may be classified by the number of bulges or segments outside the channel and are referred to as II_0, II_1, and II_2, accordingly, see Fig. 3.4. These shapes are all composed of two types of curved segments – one with and one without bulge – as shown in Fig. 3.5(b) and (c). In order to compute the bending energy of shapes II_0, II_1, and II_2, we first consider curved segments of length L_* of each type[3]. These segments obey boundary conditions $\theta(0) = 0$ and $\theta(L_*) = \pi$, and they start on one edge and end on the other, which is enforced by a constraint on the tangent vector component perpendicular to the channel, see Fig. 3.5(b) and (c), namely

$$
\int_0^{L_*} ds \sin\theta(s) - a_{st} = 0,
\tag{3.18}
$$

via the Lagrange multiplier ν. The corresponding Euler-Lagrange equation is

$$
\kappa\,\ddot{\theta}(s) - \nu \cos\theta(s) = 0.
\tag{3.19}
$$

and the integrated form reads

$$
\dot{\theta}(s) = \pm \left\{ 2\frac{\nu}{\kappa} \left[\frac{c}{\nu} + \sin\theta(s) \right] \right\}^{1/2} \quad \text{or} \quad ds = \pm d\theta \left\{ 2\frac{\nu}{\kappa} \left[\frac{c}{\nu} + \sin\theta(s) \right] \right\}^{-1/2}.
\tag{3.20}
$$

For the bulged segment in Fig. 3.5(b) the sign of $\dot{\theta}(s)$ changes from plus to minus at the inflection point, whereas it is always positive for the segment depicted in

---

[3]Later on we will call the length of the bulged segment L_*^{B} and the length of the segment without bulge $L_*^{\cancel{\mathrm{B}}}$, respectively. This notation is already used in Fig. 3.5(b) and (c).
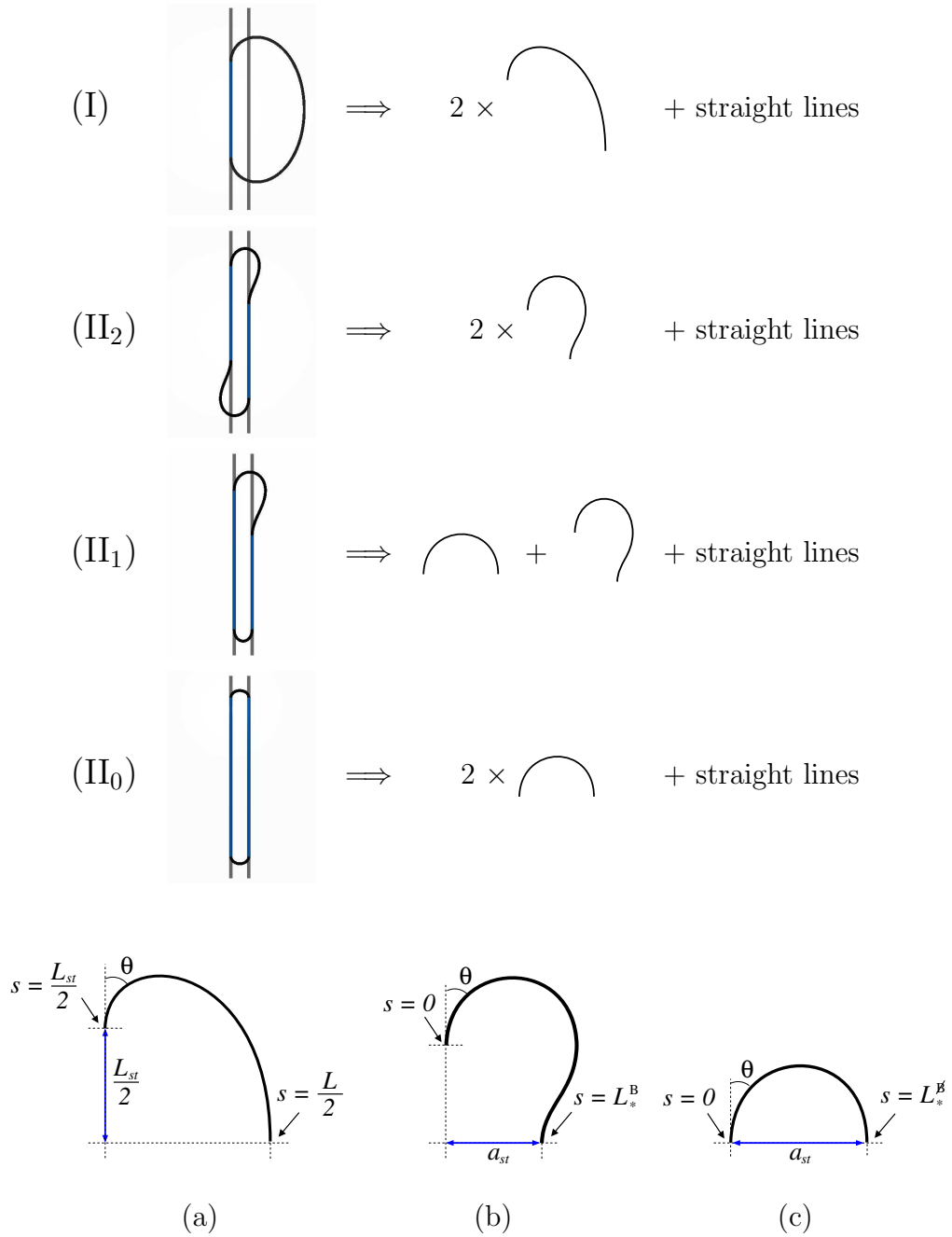
Figure 3.5: Shapes I, II$_0$, II$_1$ and II$_2$ in Fig. 3.4 can be divided into straight (adsorbed) and curved (desorbed) constituent parts. Accordingly, configuration I contains an axissymmetric curved segment, one half of which is depicted in (a), whereas shapes II$_0$, II$_1$ and II$_2$ are combinations of the appropriate curved parts (b) with and (c) without bulge.

Fig. 3.5(c). All in all, the system of equations that determines c, ν and E_b for both shapes is given by

$$L_* \left(\frac{2\nu}{\kappa}\right)^{1/2} = \left[\int_0^\pi +2\int_\pi^{\theta_{\text{inf}}}\right] d\theta \frac{1}{(p + \sin\theta(s))^{1/2}} \equiv f_1(p),$$

$$a_{st} \left(\frac{2\nu}{\kappa}\right)^{1/2} = \left[\int_0^\pi +2\int_\pi^{\theta_{\text{inf}}}\right] d\theta \frac{\sin\theta}{(p + \sin\theta(s))^{1/2}} \equiv f_2(p), \qquad (3.21)$$

$$E_b^{\text{II}} \left(\frac{2}{\kappa\nu}\right)^{1/2} = \left[\int_0^\pi +2\int_\pi^{\theta_{\text{inf}}}\right] d\theta (p + \sin\theta(s))^{1/2} \equiv f_3(p),$$

with $p \equiv c/\nu$, $\pi < \theta_{\text{inf}} = \arcsin(-c/\nu) < 3\pi/2$ for the bulged shape and $\theta_{\text{inf}} = \pi$ for the shape without bulge, so that, in this case, the second integral in each equation is absent. The explicit expressions of the functions f_1, f_2 and f_3 are rather lengthy, but can be found in App. B. There, quantities referring to the segment with or without bulge are indicated by an index B and $\cancel{\text{B}}$, respectively.

In the same manner as for the conformation I, the equations can be combined to give an implicit equation for p of the form

$$\frac{L_*}{a_{st}} = \frac{f_1(p)}{f_2(p)} \qquad (3.22)$$

and a formula for the bending energy of the curved segment depending on p

$$E_b^{\text{II}}(p, L_{st}) = \kappa(2L_*)^{-1} f_1(p) f_3(p). \qquad (3.23)$$

Now the different pieces have to be joined together to form the shapes II_0, II_1 and II_2. The conformations II_0 and II_2 are symmetric and, therefore, the bending energy is simply two times the contribution of the corresponding segment of length $L_* = (L - L_{st})/2$. For shape II_1, on the other hand, the non-adhered length $L - L_{st}$ has to be distributed between the two curved parts such that the sum of the bending energies $E_b^{\text{B}}(L_{st} + dL_{st}) + E_b^{\cancel{\text{B}}}(L_{st} - dL_{st})$ is minimized with respect to dL_{st}. One finds, that dL_{st} varies only weakly for the ranges of $L - L_{st}$ considered here and can thus be approximated by an appropriate constant value. The resulting bending energies for shapes I, II_0, II_1 and II_2 as functions of L_{st} are plotted and compared to numerical results in Fig. 3.6(a).

3.2.4 Numerical energy minimization

For some systems, that are considered in this chapter, the analytical energy minimization becomes very involved, so that we prefer to switch to a numerical treatment using the freely available program package SURFACE EVOLVER 2.26 [101]. As for the system with the topographical channel a numerical and an

analytical analysis are feasible, it offers the possibility to compare the results and thus to check the reliability of the numerical calculations for more complicated substrate structures.

The SURFACE EVOLVER was originally designed to minimize the energy of two-dimensional surfaces subject to constraints, but can also be applied to one-dimensional 'surfaces'. In this framework, the contour of the polymer is discretized and represented by a set of vertices and directed edges, which connect neighboring vertices. The contour length of a shape segment is identified with the sum over the length of the corresponding edges, which is a reasonable approximation, if the discretization is fine enough. Further, one may assign to each vertex a bending energy, which is identical to the interaction defined by (2.5) interpreting the edges as tangent vectors of length b. Therefore, it is necessary to assure, that the edges have approximately the same length, or, in other words, that the vertices are uniformly distributed along the contour. In addition, constraints on vertices and edges or quantities, such as the contour length, can be introduced.

The basic operations are the *refinement* of the discretization, the *vertex average* and, of course, an *iteration step*. The refinement operation subdivides each edge by two edges and a vertex in the middle. Constraints and energies defined for the original edge are inherited by the two new edges. Similarly, the properties of the new vertex are determined by the properties of its two neighboring vertices. Further, by performing a vertex average, one makes sure that the vertex positions are evenly spread out along the contour, which otherwise leads to wrong results e.g. for the bending energy. At each iteration step, all vertices are moved to reduce the overall energy, while satisfying the constraints, according to the gradient descent or the conjugate gradient method. In practice, one usually starts with only a few vertices and edges and successively refines, averages over vertex positions and iterates using the gradient descent method a few times until a regular shape is reached, which is reasonably close to an energy minimum. Then, one switches to the more efficient conjugate gradient method and occasionally averages over the vertex positions. When the energy ceases to change significantly, the refinement is further increased to enhance the precision of the energy. Snapshots of shapes resulting from this minimization procedure are shown in Fig. 3.4 and later on in Fig. 3.13.

In principle, we are repeating the minimization of the bending energy in analogy to the previous section, while the contour length L, the width of the topographical channel a_{st} and the bending rigidity κ are kept fixed. Then the bending energy is minimized at a given value for the adhered length L_{st}, which is achieved by constraining the x coordinate of the corresponding edges and vertices to $x = \pm a_{st}/2$. As already pointed out, the ring may bind to only one or to both edges corresponding to two different initial conditions. For conformations, that are adhered to both edges of the channel, such as the shapes II_0, II_1 and

II$_2$, the adhered (and likewise the non-adhered) segments can exchange length. The computation of the bending energy for different values of L_{st} is performed sequentially, by gradually increasing or decreasing L_{st}. Hereby the optimal shape for a given L_{st} serves as initial configuration for the subsequent minimization for slightly increased or decreased L_{st}.

The numerical data for $E_b(L_{st})$ are shown together with our analytical results in Fig. 3.6(a) and are found to be in excellent agreement. Consequently, in this case, it is sufficient to perform the remaining steps of the minimization procedure only with the analytical results, as the outcome should be identical in both cases.

Alternatively to constraining edges of lengths L_{st} to $x = \pm a_{st}/2$, and thus realizing a contact potential, a potential consisting of two thin potential wells, that model the surface steps according to Fig. 3.3, can be used. Then again the length located at the potential wells is kept constant. In practice, the potential wells have to be smooth and not too thin, since in the minimization algorithm of the SURFACE EVOLVER energy gradients are computed, which otherwise become infinite at the boundaries $|x \pm a_{st}| = l/2$. The position of the vertices and edges representing the ring contour need not to be fixed, but initially the ring has to be placed such that the contour overlaps the surface structure. The results obtained by this approach agree qualitatively with the data that is presented here, but exhibit artifacts that can be traced back to the flattened potential and the relatively big potential range l that has to be chosen.

3.2.5 Projected energy landscape

As an illustration of the above calculations, Fig. 3.6(a) shows the bending energy E_b, normalized by the typical energy scale

$$E_{st} \equiv \frac{\kappa}{a_{st}}, \tag{3.24}$$

plotted as a function of the adhered length in units of the channel width $\bar{L}_{st} \equiv L_{st}/a_{st}$. The dots and solid lines represent the numerical data and analytical results, respectively. Their different colors indicate different morphologies. A horizontal line, that marks the bending energy of a circle with $\bar{L} = 20$ as a lower bound, is also included. As was already mentioned in the previous section, the numerical and analytical results match perfectly.

As intuitively expected, for small L_{st}, conformation I has the smallest bending energy (3.17) starting at $L_{st} = 0$, where it is equivalent to a circle, but the energy diverges as L_{st} approaches $L/2$. At $L_{st} = 0$, also the asymmetric conformation with two bulges II$_2$ initiates, which corresponds to a ring conformation that is bound to each edge with a single contact point. The symmetric version of shape II$_2$ does not exist before $\bar{L}_{st} \simeq 6.30$ (not indicated explicitly), where the two

(a)

(b)
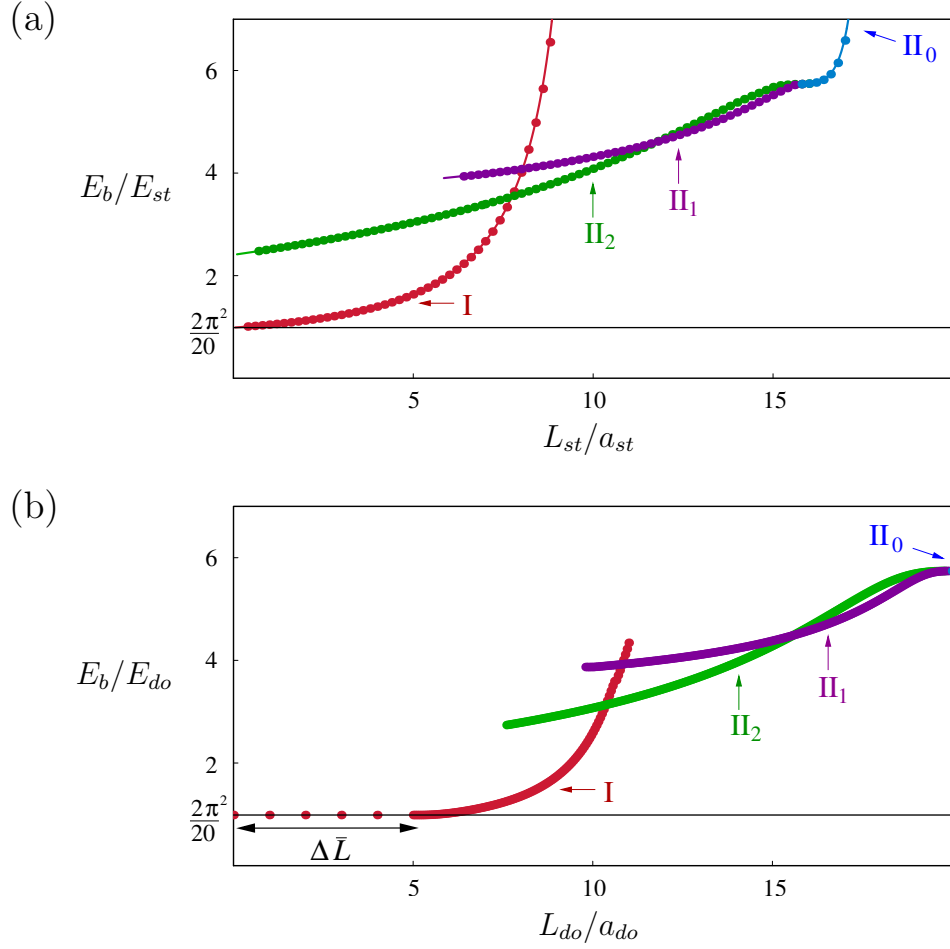
Figure 3.6: (a) The bending energy E_b of all relevant conformations to a topographical surface channel of width a_{st} (in units of $E_{st} = \kappa/a_{st}$) as a function of the adhered length L_{st} (in units of a_{st}) for a semiflexible ring with $L/a_{st} = 20$ adsorbing on a topographical surface channel of width a_{st}. The analytical results (solid lines) and the numerical data (dots) of the different shapes are shown in different colors. The arrows indicate, where the snapshots in Fig. 3.4 have been taken. (b) The corresponding graph for a ring with $L/a_{do} = 20$ adhering to a substrate with the chemically modified stripe of width a_{do} and adhesion strength $|W_{do}|$ is shown. In this case the bending energy E_b is normalized by the typical energy scale $E_{do} = \kappa/a_{do}$ and the adhered length L_{do} is measured in units of a_{do}. The numerical data are shown as dots. Apparently, there is an almost constant shift in the adhered length $\Delta\bar{L}$ compared to the results for the topographical structure in (a), which can be attributed to the fact that, in contrast to the channel, the stripe domain is also adhesive between its boundaries. The arrows point to shapes that are displayed in Fig. 3.13(a). The fact, that the red curve overlaps the green and the purple curve is discussed in detail in Section 3.2.7.

bulges touch, which are located on the same side of the striped structure in this case. For $\bar{L}_{st} > 6.30$, the energies of the asymmetric and the symmetric realizations of shape II_2 coincide.

On the other hand, in order to assume the conformation II_1, a minimal adhered length $L_{st} > 0$ is needed, which is required for a closed configuration, cf. Fig. 3.5(b) and Section 3.2.6. For the present case, i.e. $\bar{L} = 20$, this minimal length is approximately $\bar{L}_{st} \simeq 5.73$. The green (II_2) and the purple (II_1) curve merge in a single blue (II_0) curve at a value $\bar{L}_{st} \simeq 15.62$, which implies, that the segment with bulge and the one without become identical, i.e. $\theta_{\inf} = \pi$ and $p = 0$ in (3.21). Finally, the blue curve tends asymptotically to infinity as L_{st} approaches $\bar{L}_{st} = \bar{L} - 2 = 18$, where the ring assumes a rectangular shape with infinite bending energy.

The projected energy landscape $\bar{E}_{tot}(\bar{L}_{st}) \equiv E_{tot}(\bar{L}_{st})/E_{st}$ for a fixed set of control parameters, $\bar{L}$ and $|w_{st}|$, is obtained by subtracting $|w_{st}|\bar{L}_{st}$ from the dimensionless bending energy $E_b(L_{st})/E_{st}$, see (3.9). In this respect, the curves in Fig. 3.6(a) represent $\bar{E}_{tot}(\bar{L}_{st})$ for $\bar{L} = 20$ and $|w_{st}| = 0$. Taking these values as a starting point, a change in the reduced potential $|w_{st}|$ effects essentially a tilt of the curves in Fig. 3.6(a) with a slope $-|w_{st}|$, whereas a variation of $\bar{L}$ to bigger or smaller rings, can roughly be achieved by stretching or compressing the $\bar{L}_{st}$-axis by a factor of $\bar{L}_{new}/\bar{L}_{old}$. Both statements are not exactly correct, but give a useful intuitive idea of the qualitative behavior.

Depending on $\bar{L}$ and $|w_{st}|$, the projected energy landscape $\bar{E}_{tot}(\bar{L}_{st})$ exhibits up to four minima, one in each branch, and two maxima, which we will analyze in detail in the following section.

3.2.6 Energy minima

Unfortunately, in our results for the bending energy, see (3.17) and (3.23), the actual dependence of L_{st} is implicit through the parameters p and q, so that the variation of the total energy $E_{tot}(L_{st})$ with respect to L_{st} in the second step (ii) of the minimization procedure, cf. (3.10), can be performed only numerically, some results are shown in Fig. 3.9(a). Consequently, the functional dependence of the total energy of the extremal points of $E_{tot}(L_{st})$ on the control parameters is also *not* accessible in this way. On the other hand, one can circumvent the determination of $E_{tot}(L_{st})$ and directly obtain the total energy of the unconstrained equilibrium morphologies by varying $\mathcal{H}$, given in (3.4), with respect to θ and L_{st} simultaneously. This procedure has the advantage that $|W_{st}|$ explicitly appears in the calculations right from the start and that the functional dependence on the control parameters can be deduced at least approximately. The prize one has to pay in return is that L_{st} is unknown initially and yet to be determined. Therefore, in the following, we will derive these energy estimates for the conformations

I, II_0, II_1 and II_2 and compare them to the exact results, which are obtained numerically by applying the rule (3.10) to (3.17) and (3.23).

Again, we start with shape I. As an explicit example, we write down the variation of the Hamiltonian with respect to θ and L_{st}, which is

$$\delta\mathcal{H} = \int_{L_{st}/2}^{L/2} ds\, \delta\theta \left\{ -\kappa\ddot{\theta} - \mu\sin\theta \right\} + \left[\kappa\dot{\theta}\,\delta\theta \right]_{L_{st}/2}^{L/2} \\ + \frac{1}{2}\delta L_{st}\left\{ -\tfrac{1}{2}\kappa\dot{\theta}^2 - \mu + \mu - |W_{st}| \right\}. \tag{3.25}$$

The variation of θ at $s = L_{st}/2$ and $s = L/2$ has to vanish, since the angles are fixed at the ends, which leads for $s = L/2$ simply to $\delta\theta(L/2) = 0$. At the contact point of the ring and the step edge, the total variation of $\theta(L_{st}/2)$ is

$$\Delta\theta(L_{st}/2) = \delta\theta(L_{st}/2) + \frac{1}{2}\dot{\theta}(L_{st}/2)\delta L_{st} \overset{!}{=} 0, \tag{3.26}$$

which we solve with respect to $\delta\theta(L_{st}/2)$ and plug into (3.25). δH has to vanish for all possible $\delta\theta(s)$ and δL_{st}, so that we find two equations for $\theta(s)$ and L_{st}, namely, the Euler-Lagrange equation (3.13), the condition (3.11) to determine the Lagrange multiplier and a *transversality condition*, that fixes the curvature at $s = L_{st}/2$ as

$$\dot{\theta}^2(L_{st}/2) = 2\frac{|W_{st}|}{\kappa} \equiv \frac{1}{R_{co}^2}, \tag{3.27}$$

where R_{co} is sometimes called the contact radius. For fixed adhered length L_{st}, δL_{st} is zero and the original result in (3.12) is recovered.

Plugging (3.27) into (3.14) yields $c = |W_{st}| - \mu$ and

$$\dot{\theta}(s)R_{co} = \left\{ 1 - \frac{\mu}{|W_{st}|} + \frac{\mu}{|W_{st}|}\cos\theta(s) \right\}^{1/2} \tag{3.28}$$

We add (3.15) and (3.16) to obtain an equation for μ

$$\frac{L}{2R_{co}} = \int_0^\pi \frac{1 - \cos\theta}{(1 - \mu/|W_{st}| + \mu/|W_{st}|\cos\theta)^{1/2}} \tag{3.29}$$

and maintain (3.16) and (3.17), which can be written in a similar form as (3.29) using (3.28), to determine L_{st} and the bending energy.

For the special case $L = 2\pi R_{co}$ or $\bar{L} = \pi\sqrt{2/|w_{st}|}$, cf. Fig. 3.7(a), the above equation (3.29) gives $\mu = 0$, which likewise results in $L_{st} = 0$. Decreasing L further, even yields a negative and thus *unphysical* result for L_{st}. In other words, a semiflexible ring of length $L = 2\pi R_{co}$ adheres to the edge of a step only at a single point, whereas rings with $L < 2\pi R_{co}$ do not bind at all to the substrate

structure. This phenomenon is also known for vesicles adhering to a flat plane with an adhesion potential of very small range [102, 103]. The interplay between adhesion and bending energy leads to an *unbinding transition*, which is not driven by thermal fluctuations. It is one example mentioned in the introduction, where the calculation for vesicles is reduced to the minimization of the contour of the vesicle's cross section due to the axial symmetry, which is the reason for the great similarities to the above treatment.

If the contour length is well above $2\pi R_{co}$, we can assume, that the curvature at the contact point is much bigger than the curvature at $s = L/2$, see Fig. 3.7(a), which, if applied to (3.28), corresponds to $\mu \simeq |W_{st}|/2$. In this approximation, one finds the adhered length in units of a_{st}

$$\bar{L}_{st}^{\mathrm{I}} \equiv \frac{L_{st}^{\mathrm{I}}}{a_{st}} \simeq \frac{L}{2} - 4R_{co} = \frac{\bar{L}}{2} - 2\sqrt{\frac{2}{|w_{st}|}} \tag{3.30a}$$

and the total energy normalized by the typical energy scale E_{st}

$$\bar{E}_{tot}^{\mathrm{I}} \equiv \frac{E_{tot}^{\mathrm{I}}}{E_{st}} \simeq 2\sqrt{2|w_{st}|} - |w_{st}|\bar{L}_{st}^{\mathrm{I}} = 4\sqrt{2|w_{st}|} - |w_{st}|\frac{\bar{L}}{2}. \tag{3.30b}$$

If the extension of the segment perpendicular to the channel Δx is equal to the channel width a_{st}, compare Fig. 3.8(a), which happens at

$$\Delta x \simeq \frac{16}{3}R_{co} \overset{!}{=} a_{st} \quad \text{or} \quad |w_{st}| \simeq 14.22, \tag{3.31}$$

the ring touches the second edge at $s = L/2$ and the tangent vector at this point is oriented parallel to the structure. Thus, the ring can also bind to the second edge and conformation I becomes unstable. Note, that if the non-adhered part of shape I is on the 'wrong' side of the structure (rotate shape I around the edge it adheres to in Fig. 3.4), this will never happen and shape I remains (meta-)stable as $|w_{st}|$ goes to infinity.

We proceed in the same way as for the conformation I, to extract the approximate functional dependence of the total energy and the adhered length on the control parameters for both curved segments depicted in Fig. 3.5(b) and (c). Variation of $\mathcal{H}$ with respect to the adhered length, i.e. the length of the curved segment, imposes the same condition on the curvature as (3.27) at all contact points. This result plugged into (3.20) determines the integration constant $c = |W_{st}|$ and leads via

$$\dot{\theta}(s)R_{co} = \pm\left\{1 + \frac{\nu}{|W_{st}|}\sin\theta(s)\right\}^{1/2} \tag{3.32}$$
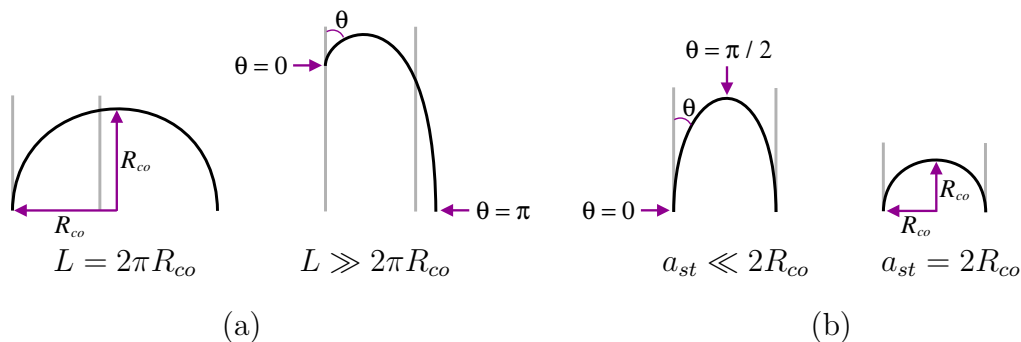
47

Figure 3.7: Two extreme cases for the segment depicted in Fig. 3.5(a) and (b) the segment without bulge shown Fig. 3.5(c), for which the energy is approximately calculated. The two outer pictures illustrate the special cases, where the contact radius R_{co} is equal to (a) the radius of the polymer ring and (b) half the stripe width. For the two inner pictures, the curvatures at different tangent angles θ are compared. The curvature at the contact point $1/R_{co}$ at $\theta = 0$ is in (a) much bigger than the curvature at $\theta = \pi$, whereas and in (b) it is much smaller than the curvature at the reference point at $\theta = \pi/2$.

and the second line of (3.21) to an equation of the form

$$\frac{a_{st}}{R_{co}} = F(\nu/|W_{st}|) \tag{3.33}$$

for the Lagrange multiplier ν, where F is a lengthy function, which is straightforward to compute, but is not explicitly shown here. Formulae for the length of the segment and the bending energy are obtained by using (3.32) to rewrite the first and the third equation in (3.21), respectively.

A special case for the shape without bulge is $a_{st} = 2R_{co}$, cf. Fig. 3.7(b), corresponding to $|w_{st}| = 2$, because then (3.33) yields $\nu = 0$ and the segment forms an exact semicircle, so that the length of the segment without bulge is given by

$$\frac{L_*^{\cancel{B}}}{a_{st}} = \frac{\pi}{2} \quad \text{for } |w_{st}| = 2 \tag{3.34a}$$

and its bending energy reads

$$\frac{E_b^{\cancel{B}}}{E_{st}} = \pi \quad \text{for } |w_{st}| = 2. \tag{3.34b}$$

On the other hand, if $|w_{st}| \ll 1$ or $a_{st} \ll 2R_{co}$, see Fig. 3.7(b), the curvature at the contact point is significantly smaller than the curvature at $\theta = \pi/2$ so that
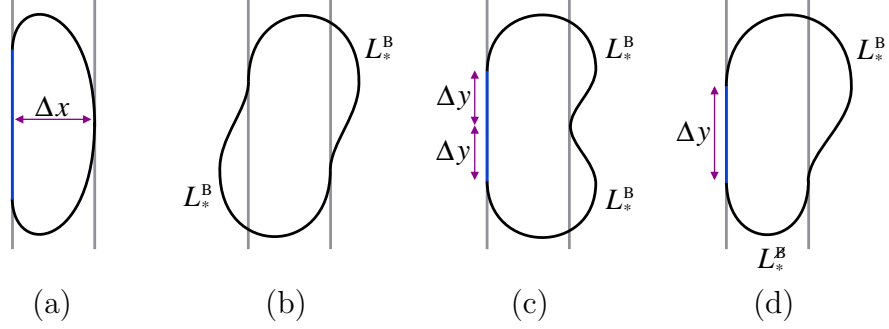
Figure 3.8: (a) Schematic picture of the configuration where shape I becomes unstable for large $|w_{st}|$ and the ring can bind to the second edge. The other schematic pictures illustrate the configurations at the stability boundary for small $|w_{st}|$ of the asymmetric and the symmetric versions of shape II_2 in (b) and (c), and of shape II_1 in (d).

both sides of the equation (3.32) are much bigger than one. Then, the equation (3.33) can be solved for $\nu/|W_{st}| \gg 1$ and one finds for the length of the segment without bulge

$$\frac{L_*^{\text{\sout{B}}}}{a_{st}} \simeq 2.19 \quad \text{for } |w_{st}| \ll 1 \tag{3.35a}$$

and for the resulting bending energy

$$\frac{E_b^{\text{\sout{B}}}}{E_{st}} \simeq 2.87 \quad \text{for } |w_{st}| \ll 1. \tag{3.35b}$$

For the bulged segment depicted in Fig. 3.5(b), a reasonable approximation for (3.33) is less obvious. The equation (3.33) gives rise to two solutions for $\nu/|W_{st}|$, that only exist for $0 < |w_{st}| < 0.35$, and an additional unphysical solution for $|w_{st}| > 0$, which is the only remaining, if $|w_{st}| > 0.35$. The latter solution can be excluded right from the beginning, whereas for the other two solutions, for $0 < |w_{st}| < 0.35$, we check the resulting behavior of the segment length. For one solution L_* decreases with increasing $|w_{st}|$, whereas for the other one L_* increases with increasing $|w_{st}|$. Accordingly, the former is the desired solution for the minimized bulged segment. The other solution is identified with the bulged segment belonging to the local maxima II_1^* and II_2^*, which we discuss in detail later on.

We expand the equation (3.33) in the corresponding region of $\nu/|W_{st}|$ and accordingly find for the length of the bulged segment

$$\frac{L_*^{\text{B}}}{a_{st}} \simeq \sqrt{\frac{2}{|w_{st}|}} \left(2.45 - 1.95|w_{st}| \right) \quad \text{for } |w_{st}| \ll 1 \tag{3.36a}$$

49

and for the bending energy

$$\frac{E_b^{\mathrm{B}}}{E_{st}} \simeq \sqrt{2|w_{st}|}\,(2.66 + 0.10|w_{st}|) \quad \text{for } |w_{st}| \ll 1. \tag{3.36b}$$

As a final step, the estimated total energies for the shapes II_0, II_1 and II_2 are computed by assembling the corresponding expressions for L_* and E_b. We obtain the total energies for conformation II_0

$$
\begin{aligned}
\bar{E}_{tot}^{\mathrm{II}_0} &\simeq 2\frac{E_b^{\mathrm{B}}}{E_{st}} - |w_{st}|\left(\bar{L} - 2\frac{L_*^{\mathrm{B}}}{a_{st}}\right) \\
&= \begin{cases} 5.74 - |w_{st}|(\bar{L} - 4.38) & \text{for } |w_{st}| \ll 1, \\ 2\pi - |w_{st}|(\bar{L} - \pi) & \text{for } |w_{st}| \simeq 2, \end{cases}
\end{aligned} \tag{3.37}
$$

and for conformation II_2

$$
\begin{aligned}
\bar{E}_{tot}^{\mathrm{II}_2} &\simeq 2\frac{E_b^{\mathrm{B}}}{E_{st}} - |w_{st}|\left(\bar{L} - 2\frac{L_*^{\mathrm{B}}}{a_{st}}\right) \\
&= |w_{st}|^{1/2}(14.45 - \bar{L}|w_{st}|^{1/2} - 5.23|w_{st}|) \quad \text{for } w_2(\bar{L}) < |w_{st}| < 0.35,
\end{aligned} \tag{3.38}
$$

with w_2 indicating the value of the reduced adhesion potential, where the adhered length becomes too small to maintain the stability of the shape. For the asymmetric version of shape II_2, this is the case if the adhered length is zero, see Fig. 3.8(b), i.e.

$$\bar{L} - 2\frac{L_*^{\mathrm{B}}(w_2)}{a_{st}} \overset{!}{=} 0. \tag{3.39}$$

If we set $w_2 = 0.35$ in relation (3.39), we find that for $\bar{L} < 8.45$ the local minimum corresponding the conformation II_2 vanishes. The symmetric realization of shape II_2, that has both bulges on the same side of the channel, becomes unstable if the bulges touch, see Fig. 3.8(c), i.e.

$$\bar{L} - 2\{L_*^{\mathrm{B}}(w_2) + \Delta y(w_2)\}/a_{st} \overset{!}{=} 0, \tag{3.40}$$

with Δy given by

$$\Delta y(|w_{st}|) \simeq \sqrt{\frac{2}{|w_{st}|}}(1.18 - 1.19|w_{st}|). \tag{3.41}$$

Again, by plugging $w_2 = 0.35$ into (3.40) we obtain that for $\bar{L} < 11.53$ this shape becomes unstable. The total energy of the remaining conformation II_1 can be written as

$$\bar{E}_{tot}^{\mathrm{II}_1} \simeq \frac{\bar{E}_{tot}^{\mathrm{II}_0} + \bar{E}_{tot}^{\mathrm{II}_2}}{2} \quad \text{for } w_1(\bar{L}) < |w_{st}| < 0.35, \tag{3.42}$$

There is also a lower limit of w_{st}, denoted by $w_1(\bar{L})$, which can be explained by the observation that this shape becomes unstable, if the bulged segment extends to the other curved segment on the other side of the ring, see Fig. 3.8(d), i.e.

$$\bar{L} - \{L_*^{\mathrm{B}}(w_1) + L_*^{\mathrm{B}}(w_1) + \Delta y(w_1)\}/a_{st} \stackrel{!}{=} 0, \qquad (3.43)$$

see Fig. 3.5(b). For $\bar{L} < 7.96$, the lower and the upper limit are equal, namely $w_1(\bar{L}) = 0.35$, also conformation II_1 ceases to exist as metastable state.

In Fig. 3.9(a), only the local minima of the projected energy landscape $\bar{E}_{tot}(\bar{L}_{st})$ as a function of $|w_{st}|$ for $\bar{L} = 20$ are shown. Note that likewise we could keep the reduced adhesion strength $|w_{st}|$ fixed and examine the functional dependence of the local energy minima on $\bar{L}$, which we will not show here, but the results are implicitly included in the morphology diagram, see Fig. 3.11(a). For the (exact) analytical results, we applied the same color code as before, while the energy estimates, given in equations (3.30b), (3.37), (3.38) and (3.42), are drawn as black dashed lines. For the elongated shape II_0, only the approximation for $|w_{st}| \ll 2$ is included. A comparison between the solid and the dashed lines demonstrates, that our energy estimates are very good for the morphologies containing bulges and good within their range of application for shapes I and II_0.

As long as $|w_{st}|$ is very small, the unbound ring is the stable conformation, while conformation II_0 is metastable. Then, at

$$\bar{L} = \bar{L}_{\mathrm{unb}} \equiv 2\pi \frac{R_{co}}{a_{st}} \quad \text{or} \quad |w_{st}| = |w_{st}|_{\mathrm{unb}} \equiv \frac{2\pi^2}{\bar{L}^2} \simeq 0.05, \qquad (3.44)$$

the curvature of the undeformed circle, is equal to the curvature required at the contact points, see (3.27), so that the ring can bind to the first edge. In other words, at $|w_{st}| = |w_{st}|_{\mathrm{unb}}$, the Hamiltonian (3.4) has two (equivalent) equilibrium configurations: the unbound circle and the circle binding to one edge with a single point. If $|w_{st}|$ is increased beyond $|w_{st}|_{\mathrm{unb}}$, the unbound circle (which touches the edge, but does not adhere) becomes unstable, whereas configuration I, with $L_{st} > 0$, represents the global minimum, and vice versa for $|w_{st}| < |w_{st}|_{\mathrm{unb}}$. Hence, at $|w_{st}| = |w_{st}|_{\mathrm{unb}}$ a *morphology transition* between the unbound circle and shape I occurs, and, at the same time, $|w_{st}| = |w_{st}|_{\mathrm{unb}}$ marks a *stability boundary* for the unbound circle and configuration I. Moreover, since the configuration I coincides with the circle at $|w_{st}| = |w_{st}|_{\mathrm{unb}}$, i.e. the internal parameter L_{st} is the same, we refer to this transition as *continuous*.

Apart from that, as naively expected, the round configuration I (red) is the state of minimal energy for small $|w_{st}|$, whereas the adhesion energy gain, and therefore the elongated shape II_0 (blue), dominates for large $|w_{st}|$ and, in fact, is the only remaining stable shape II_0 for $|w_{st}| \gtrsim 14.2$, see (3.31), which is not shown in the picture. The morphological transition between these two shapes is always accompanied by a jump in the adhered length L_{st} and is thus *discontinuous*. The transition point is determined approximately by equating the respective
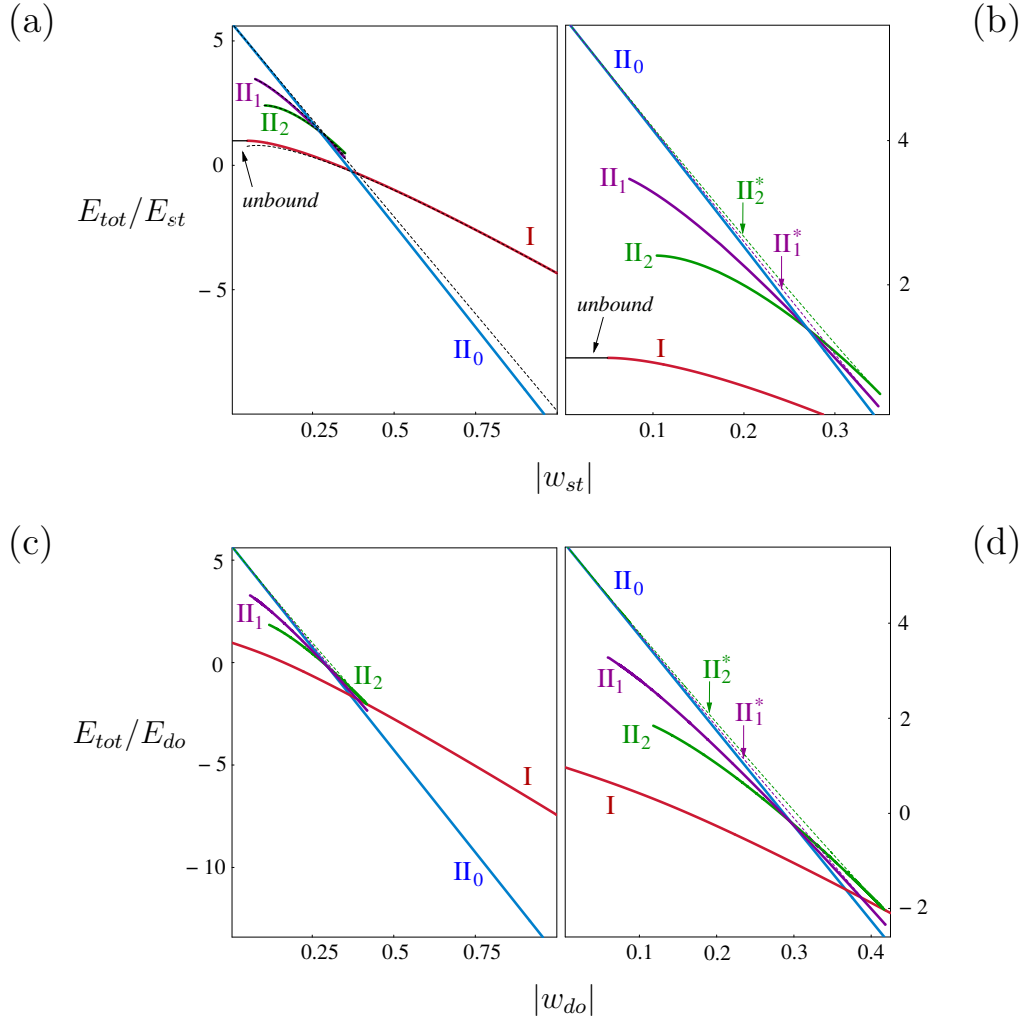
Figure 3.9: (a) Total dimensionless energy E_{tot}/E_{st} of all (meta-)stable states versus the reduced potential $|w_{st}|$ for a semiflexible ring of contour length $L/a_{st} = 20$ adsorbing on a topographical surface channel of width a_{st}. Analytical results for the metastable and stable shapes are shown as colored solid lines, whereas the estimates for these energy curves calculated in Section 3.2.2 are drawn as dashed lines and seem to match fairly well. (b) A magnification of the upper left corner of (a) including also the unstable states II_1^* and II_2^* as purple and green dashed line, respectively. The energy estimates are omitted for clarity. The analogous numerical results of the dimensionless total energy E_{tot}/E_{do} as a function of $|w_{do}|$ for a ring adhered to a chemical domain with $L/a_{do} = 20$ in (c) and magnified in (d). The unbound circle is never stable and therefore absent in this case.

Figure 3.10: Two schematic examples of how the energy curves as a function of the adhered length representing (a) shape II_2 and (b) shape I in the proje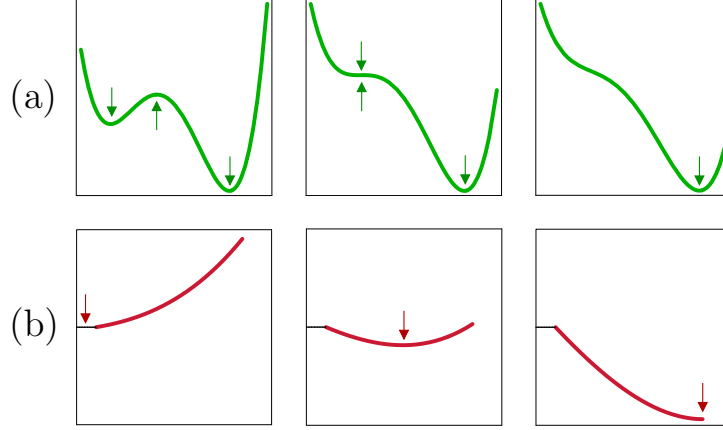cted energy landscape evolve, if $|w_{st}|$ is increased. The arrows indicate the locations of local minima and maxima. The minimum on the right in the green curve belongs already to shape II_0, which in Fig. 3.6 (a) is colored in blue. In (a) the transition state is identified with the local maximum in between the two local minima. At the stability boundary, the local maximum fuses with a local minimum to form a saddle point (middle). By contrast in (b), the transition state cannot be identified. Then, the stability boundaries are characterized by a horizontal slope at the end point of a curve (right).

energy estimates, see the next section. In the vicinity of this transition, namely, for $w_1, w_2 \lesssim |w_{st}| \lesssim 0.35$, also the shapes II_1 (purple) and II_2 (green) become metastable. Note, that the endpoint of the green curve at $w_2 \simeq 0.10$ refers to the asymmetric version of shape II_2. Its symmetric counterpart already ends at $w_2 \simeq 0.18$, which is not shown explicitly in Fig. 3.9.

3.2.7 Stability

Now we turn to the stability analysis. As we mentioned earlier, the number of curves, that are present for a particular value of $|w_{st}|$ in Fig. 3.9(a), reflects the number of local minima of the projected energy landscape. Accordingly, the start and end points of the curves in Fig. 3.9(a) mark those values of $|w_{st}|$, for which a new minimum arises or a current minimum disappears in $\bar{E}_{tot}(\bar{L}_{st})$. The local extrema of the projected energy landscape have to satisfy the necessary condition, that the local slope of $\bar{E}_{tot}(\bar{L}_{st})$ has to be equal to $|w_{st}|$. Furthermore, the

sufficient condition for an extremum of the projected energy landscape $\bar{E}_{tot}(\bar{L}_{st})$ to be a local minimum, $\partial^2_{\bar{L}_{st}}\bar{E}_{tot} > 0$, is found to be equivalent with the statement, that the adhered length of the (meta-)stable morphologies grows with increasing $|w_{st}|$.

In order to examine the other stability boundary for shapes II_1 and II_2 at $|w_{st}| \simeq 0.35$, we include also the two local maxima of the projected energy landscape, which we call II_1^* and II_2^*, shown as purple and green dashed lines in Fig. 3.9(b). In the projected energy landscape, see Fig. 3.6(a), the maximum related to shape II_1^* (II_2^*) emerges in the energy branch of conformation II_1 (II_2) for $0 < |w_{st}| \lesssim 0.35$ and is located between $\bar{L}_{st} = 13.58$ ($\bar{L}_{st} = 11.55$) and $\bar{L}_{st} = 15.62$, where the bending energy $\bar{E}_b(\bar{L}_{st})$ and, consequently, also $\bar{E}_{tot}(\bar{L}_{st})$ are concave. Accordingly, conformations II_1^* and II_2^* have qualitatively the same form as II_1 and II_2, but the bulges are smaller. In order to keep track of the various curves, the energy estimates are no longer displayed.

For the moment, let us trace the green solid curve representing shape II_2 and the green dashed curve representing shape II_2^* simultaneously approaching $|w_{st}| = 0.35$ from the left in Fig. 3.9(b). As we stated above, an increase in $|w_{st}|$ causes the two bulges of II_2 to become smaller, as more length adheres to the edges, so that the local minimum in the projected energy landscape belonging to the equilibrium shape II_2 is shifted to higher adhered length L_{st} as $|w_{st}|$ is increased. On the contrary, the adhered length of II_2^*, which is always greater than the one of II_2 *decreases* continuously as $|w_{st}|$ is increased, so that the corresponding maximum is shifted towards the minimum of II_2. At $|w_{st}| \simeq 0.35$, the two shapes are identical which indicates, that the local minimum and the local maximum of $\bar{E}_{tot}(\bar{L}_{st})$ corresponding to these shapes fuse into a saddle point, with $\partial_{\bar{L}_{st}}\bar{E}_{tot}(\bar{L}_{st}) = \partial^2_{\bar{L}_{st}}\bar{E}_{tot}(\bar{L}_{st}) = 0$, which is schematically shown in Fig. 3.10(a). Such a point is also called *bifurcation point*, because the energy in Fig. 3.9(b) forks into two branches, namely, a metastable and an unstable shape. If we increase $|w_{st}|$ beyond this point, the ring morphology changes abruptly to conformation II_0, which causes a jump in the adhered length L_{st}. In an analogous manner, the maximum belonging to shape II_1^* and the minimum belonging to shape II_1 merge at $|w_{st}| \simeq 0.35$, leading to another bifurcation point in Fig. 3.9(b), while at $|w_{st}| = 0$ both maxima fuse with the minimum of shape II_0, see Fig. 3.6(a). In Fig. 3.9(b) this corresponds to the point at $|w_{st}| = 0$, where the energy furcates into one stable (blue line) and two unstable states (purple and green dashed lines). In the context of thermodynamics, the triangle formed e.g. by the dashed green, the solid green and the solid blue energy curve is known as *Gibbs triangle* or *Gibbs wing*. The corners of the triangle are defined by the two bifurcation points and the transition point between the (meta-)stable shapes II_2 and II_0.

Before discussing the remaining stability boundaries, let us mention a peculiarity of the projected energy landscape. In Fig. 3.6(a) the red curve overlaps

the green and the purple curve, which is a result of the mapping of the full (continuous) energy landscape onto the adhered length. As a consequence, the curves of the shapes I, II$_1$ and II$_2$ are not connected and the respective transition states corresponding to local maxima in the full energy landscape cannot be resolved in this projection of the energy landscape. The determination of all local minima and their stability boundaries is, however, still possible as we will see below. In order to identify the missing transition states, more constraints would have to be imposed, e.g. on the center of mass coordinate perpendicular to the stripe axis. But since the knowledge of the transition states is not essential for our analysis, they will be omitted here.

For the disconnected curves in Fig. 3.6(a), the stability boundaries are found as follows. If we start with the projected energy landscape at $\bar{L} = 20$ and $|w_{st}| = 0$, shown in Fig. 3.6(a), and gradually increase $|w_{st}|$ (by gradually tilting the curves), the minimum in a particular branch, will initially occur at the starting point of the branch, when the local slope at this point is horizontal, then the position of the minimum will move to higher values of L_{st} towards the end point of the branch until the local slope at the end point is horizontal and the minimum vanishes. This means, e.g. for shape I represented by the red curve in Fig. 3.6(a), that at $|w_{st}| \simeq 0.05$, a minimum emerges at $L_{st} = 0$, which is shifted step by step towards the end of the curve at $\bar{L}_{st} \simeq 9.25$, where, for $|w_{st}| \simeq 14.2$, it disappears, which is schematically shown in Fig. 3.10(b). Consequently, $|w_{st}| = |w_{st}|_{\mathrm{unb}}$ and $|w_{st}| \simeq 14.2$ are the stability boundaries of shape I. If $|w_{st}|$ changes only weakly beyond these boundaries, a ring that assumes shape I either unbinds (which is caused by decreasing $\bar{L}$, too), or abruptly binds to both edges and adjusts is shape according to the only remaining minimum for $|w_{st}| > 14.2$, namely, shape II$_0$. In a similar fashion, the stability boundary $w_1(\bar{L})$ ($w_2(\bar{L})$) for configuration II$_1$ (II$_2$) is equivalent to the situation, where the purple (green) curve in Fig. 3.6(a) starts at $\bar{L}_{st} \simeq 5.73$ ($\bar{L}_{st} = 0$ for the asymmetric and $\bar{L}_{st} \simeq 6.30$ for the symmetric realization of shape II$_2$) with a horizontal slope, and this boundary can be crossed by decreasing either of the control parameters $\bar{L}$ and $|w_{st}|$.

All in all, there are up to four metastable states that should give rise to a rather complex shape hysteresis.

3.2.8 Morphology diagram

The full morphology diagram Fig. 3.11(a) shows how the equilibrium morphology is controlled by the parameters $|w_{st}|$ and $\bar{L}$. Morphology boundaries from the analytical minimization procedure are denoted by stars, triangles, dots and diamonds.

The main feature of the morphology diagram is the discontinuous transition between morphologies I and II$_0$, (stars). The location of this transition can be
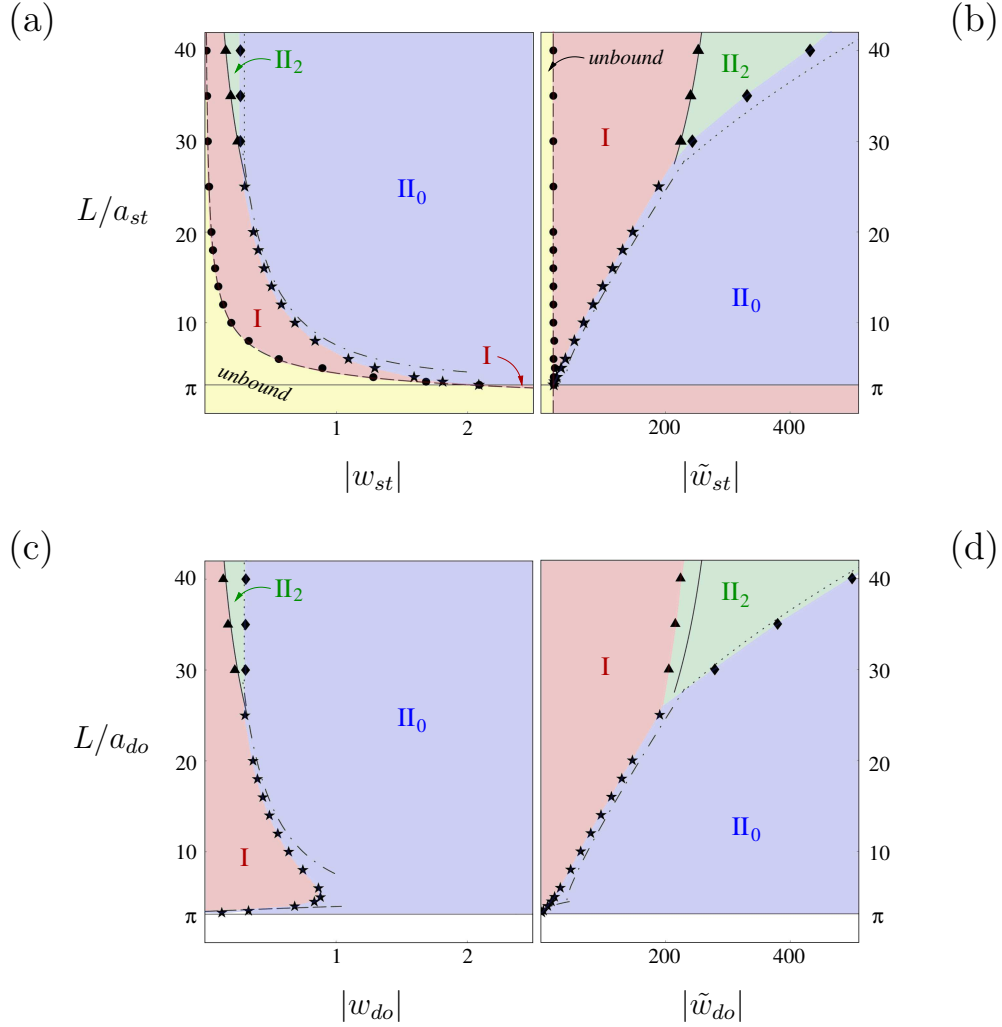
Figure 3.11: Morphology diagram for a ring of length L adhering to the topographical surface channel of width a_{st} as a function of (a) L/a_{st} and $|w_{st}| \equiv |W_{st}| a_{st}^2/\kappa$ and (b) L/a_{st} and $|\tilde{w}_{st}| \equiv |W_{st}| L^2/\kappa$. If the topographical structure is replaced by a chemical domain of width a_{do} and adhesion strength $|W_{do}|$, the system is characterized by (c) L/a_{do} and $|w_{do}| \equiv |W_{do}| a_{do}^2/\kappa$ or (d) L/a_{do} and $|\tilde{w}_{do}| \equiv |W_{do}| L^2/\kappa$. The parameter choice in (b) and (d) is advantageous if the structure width a_{st} and a_{do} is varied, while the other system parameters are kept constant. Morphological transitions as obtained from analytical energy minimization in (a) and (b) and from numerical energy minimization in (c) and (d) are represented by stars, triangles, diamonds and dots. The approximate results (3.45), (3.46), and (3.47) for these transitions are indicated as dot-dashed, dotted and solid lines, respectively. In (a) and (b) the dashed line marks the exact unbinding transition (3.44), whereas in (c) and (d) the dashed line signifies the estimated transition for small rings (3.61).

derived from the condition $\bar{E}_{tot}^{\mathrm{I}} = \bar{E}_{tot}^{\mathrm{II}_0}$. As $\bar{E}_{tot}^{\mathrm{I}}$ in (3.30b) is valid for $|w_{st}| \gg |w_{st}|_{\mathrm{unb}}$, we also choose in (3.37) the version of $\bar{E}_{tot}^{\mathrm{II}_0}$ for $|w_{st}| \simeq 2$, to deal in both cases with expressions that apply to $|w_{st}| \gg 1$. One obtains

$$\bar{L}_{\mathrm{I}-\mathrm{II}_0} \simeq 2\pi - 8\sqrt{\frac{2}{|w_{st}|}} + \frac{4\pi}{|w_{st}|}, \tag{3.45}$$

shown as dot-dashed line in Fig. 3.11(a). This transition line terminates at $\bar{L} = \pi$ and $|w_{st}| = 2$, where it intersects the unbinding transition line represented by the dots and the dashed line from the analytical minimization and the exact result (3.44), respectively. At this point, the ring is just large enough, that the undeformed circle fits exactly into the channel touching each edge with a single point, and, at the same time, the transversality condition (3.27) is fulfilled, so that the ring adheres to both edges. If $|w_{st}|$ is further increased, while the length is decreased, so that $\bar{L}_{\mathrm{unb}} < \bar{L} < \pi$, the ring will bind to one edge, but cannot reach the other without paying a large amount of bending energy. Consequently, shape I is stable in this region.

For rather large rings, $\bar{L} \gtrsim 27.52$, also configurations II_1 and II_2 are found to be stable. At the vertical boundary between configurations II_0 and II_2 (diamonds), it becomes energetically favorable for the confined shape II_0 to create bulges, i.e., $\bar{E}_{tot}^{\mathrm{II}_0} = \bar{E}_{tot}^{\mathrm{II}_2}$ or equivalently $\bar{E}_{tot}^{\mathrm{II}_0} = \bar{E}_{tot}^{\mathrm{II}_1}$, which gives

$$|w_{st}|_{\mathrm{II}_0-\mathrm{II}_2} \simeq 0.30, \tag{3.46}$$

shown as dotted line in Fig. 3.11(a). In fact, below this boundary, $|w_{st}| < |w_{st}|_{\mathrm{II}_0-\mathrm{II}_2}$, it is always preferable to form two and not only one bulge, such that shape II_1 is only stable on the boundary line and otherwise metastable. In addition, it is remarkable, that (3.46) is *independent* of $\bar{L}$ and that the bulges on the boundary have a fixed size, which can be calculated by plugging (3.46) into (3.36) and is found to be $L_*^{\mathrm{B}}/a_{st} \simeq 4.81$. Furthermore, we can obtain the transition line between shapes II_2 and I (triangles) using the condition $\bar{E}_{tot}^{\mathrm{I}} = \bar{E}_{tot}^{\mathrm{II}_2}$ resulting in

$$\bar{L}_{\mathrm{I}-\mathrm{II}_2} \simeq |w_{st}|^{-1/2}(17.59 - 10.47|w_{st}|) \tag{3.47}$$

shown as solid line in Fig. 3.11(a). All transition lines are in good agreement with the results calculated in Section 3.2.3.

The transition lines depend on the control parameters of the system, hence, measurements of these transition lines can be used to determine material parameters, such as $|W_{st}|$ or κ, experimentally. A fundamental difference compared to other experimental methods to determine the bending rigidity is, that no *external* forces, e.g. via an AFM tip, have to be applied to the polymer, but that the substrate pattern itself exerts forces on the ring. In an experiment, the transition

lines in the morphological diagram Fig. 3.11(a) could be crossed in horizontal direction by changing the adhesion strength $|W_{st}|$ of the substrate, e.g. for DNA rings adsorbed to mica this could be achieved by changing the charge density on the surface. Likewise, one could vary the bending rigidity κ by performing the experiment with different polymers, which is probably the least feasible option. The equilibrium energies for this type of experiment are described by Fig. 3.9(a). On the other hand, one could use rings of different length on the same substrate and thereby observe ring morphologies along a vertical line in Fig. 3.11(a). The last and maybe simplest idea would be to fabricate a substrate with several channels of different width a_{st}. In this case, one would change the ratio of the involved length scales $\bar{L}$ and the reduced adhesion strength $|w_{st}|$ at the same time, and therefore, it is much more convenient to characterize the ring/channel-system by $\bar{L}$ and the control parameter $|\tilde{w}_{st}| \equiv |W_{st}|L^2/\kappa$, which we introduced in (3.7). For the sake of completeness, the morphological diagram in terms of $\bar{L}$ and $|\tilde{w}_{st}|$ is depicted in Fig. 3.11(b). The symbols and lines are the *same* results as shown in Fig. 3.11(a), but rephrased according to (3.7). The ring morphologies recorded for different channel widths a_{st} would now lie on a vertical line in Fig. 3.11(b).

3.2.9 Thermal fluctuations

Finally, we turn to the influence of thermal fluctuations. Thermal fluctuations allow the polymer ring to overcome energy barriers $\Delta E < T$ ($k_B \equiv 1$), which is equivalent to $\Delta \bar{E} < 2a_{st}/L_p$ for a semiflexible polymer with a persistence length $L_p = 2\kappa/T$. In our system, the highest energy barriers[4] $\Delta \bar{E}$ arise between shape II_2 and the transition state II_2^* for small values of $|w_{st}|$, which can be read off from Fig. 3.9(b), and are of the order $\Delta \bar{E} \simeq 1$. Therefore, the influence of thermal fluctuations crucially depends on the ratio L_p/a_{st}, namely

$$\begin{aligned} \Delta E \gg T \ \ \text{for} \ L_p/a_{st} \gg 1, \\ \Delta E \ll T \ \ \text{for} \ L_p/a_{st} \ll 1. \end{aligned} \tag{3.48}$$

Our results apply for persistence lengths much larger than the stripe width, $L_p/a_{st} \gg 1$, where energy barriers are relevant. Then all four ring shapes are observable, and their morphological transitions exhibit a pronounced hysteretic behavior. For flexible polymers with $L_p/a_{st} \ll 1$, on the other hand, thermal fluctuations allow the polymer to change orientation within the channel such that the four morphologies can no longer be clearly distinguished.

Another effect that has to be considered is connected to the loss of configurational entropy for the adhered segments. If the adhered length is smaller or

---

[4]The energy barriers from the transition states that could not be identified due to the mapping of the energy landscape are not included in this analysis.
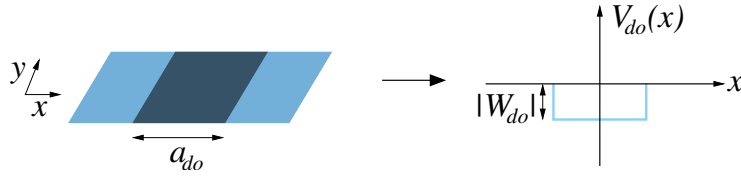
Figure 3.12: Schematic image of a substrate surface containing a chemically modified striped domain of width a_{do} and the corresponding adsorption potential $V_{do}(x)$. Polymer segments adsorbed to the striped domain gain the additional adsorption energy $W_{do} < 0$ per length, so that $V_{do}(x)$ is a broad square well with boundaries at $x = \pm a_{do}/2$.

comparable to the persistence length, we can basically use the results obtained in [104, 105]. In this case, the adsoption strength $|W_{st}|$ is replaced by the free adsorption energy per segment f_{st}, which is roughly given by

$$|f_{st}| \simeq |W_{st} - W_{c,st}|. \tag{3.49}$$

Here $W_{c,st}$ is the critical potential, which depends on the range of the width of the potential well l, the temperature and the persistence length. Consequently, in the morphological diagram all transition lines are essentially shifted by a constant $W_{c,st}$ towards smaller adsorption strengths. Thereby, the part of the morphological diagram for which $|W_{c,st}| > |W_{st}|$ becomes irrelevant.

3.3 Chemically striped surface domain

3.3.1 Substrate model

In this section, the surface channel is replaced by a chemically structured striped domain of width a_{do}, see Fig. 3.12. Again the overall adsorption is assumed to be so large, that the polymer is tightly bound to the substrate, without restraining its lateral motion. The energy contribution from the overall adsorption will be omitted, as we are only interested in the additional adhesion energy $W_{do} < 0$ per length, which a polymer segment gains on the striped domain. As illustrated in Fig. 3.12, such a substrate structure can be modelled by a generic square well adsorption potential of the form

$$V_{do}(x) = \begin{cases} W_{do} & \text{for } |x| \leq a_{do}/2, \\ 0 & \text{for } |x| > a_{do}/2, \end{cases} \tag{3.50}$$

and the Hamiltonian for this system is obtained by exchanging $V_{st}(x)$ by $V_{do}(x)$ in (3.3)

$$\mathcal{H}\{\theta(s)\} = \mathcal{H}_{\mathrm{wlc}}\{\theta(s)\} + \int_0^L ds V_{do}(x). \tag{3.51}$$

For a particular conformation, we denote the length of segments adhered to the domain by L_{do} and the adhesion energy is then given by $E_{ad} = -|W_{do}|L_{do}$.

3.3.2   Analytical energy minimization

In order to find the ring morphologies that extremize (3.51) we can in principle follow the same minimization procedure as described in Section 3.2.2. A small but crucial difference compared to the channel is, that the adhesive domain now also comprises the region between the boundaries $x = \pm a_{do}/2$, which implies, that the segments adhered to the domain no longer need to be straight and therefore contribute to the bending energy of the conformation. Remarkably, the ring shapes minimizing the bending energy are almost identical to the shapes of minimal energy for a topographical surface channel of the same width $a_{st} = a_{do}$, see Fig. 3.13. It is therefore adequate to use the same nomenclature for both types of surface structures.

As an example of a nontrivial ring morphology, we derive the resulting system of equations for a conformation similar to shape I, see Fig. 3.13(a) and (b). The boundary conditions are $\theta(0) = 0$ and $\theta(L/2) = \pi$ in this case, and the constraint (3.11) guaranteeing ring closure is replaced by

$$\int_0^{L/2} ds \cos\theta = 0. \tag{3.52}$$

In addition, we need to impose a constraint on the adhered segments

$$\int_0^{L_{do}/2} ds \sin\theta - a_{do} = 0 \tag{3.53}$$

to assure that they stay on the adhesive striped domain. Then, the corresponding Hamiltonian reads

$$\begin{aligned}
\mathcal{H} = &\int_0^{L_{do}/2} ds \left\{ \frac{1}{2} \kappa \dot{\theta}_<^2 + \mu \cos\theta_< + \rho \sin\theta_< \right\} \\
&+ \int_{L_{do}/2}^{L/2} ds \left\{ \frac{1}{2} \kappa \dot{\theta}_<^2 + \mu \cos\theta_> \right\} - |W_{do}| \frac{L_{do}}{2} - \rho a_{do},
\end{aligned} \tag{3.54}$$

which now contains two Lagrange multipliers μ and ρ. Further, we have introduced the tangent angles with subscripts to distinguish, whether they belong to

the adhered segment ($<$) or not ($>$). They have to obey $\theta_<(L_{do}/2) = \theta_>(L_{do}/2)$ at the stripe boundary to avoid a diverging curvature at this point. Again, we examine the response of the Hamiltonian to a small variation in θ and L_{do}[5], with $\delta\theta_<(L_{do}/2) = \delta\theta_>(L_{do}/2)$, leading to

$$\delta\mathcal{H} = \int_0^{L_{do}/2} ds\,\delta\theta_< \left\{ -\kappa\,\ddot{\theta}_< - \mu\sin\theta_< + \rho\cos\theta_< \right\}$$
$$+ \int_{L_{do}/2}^{L/2} ds\,\delta\theta_> \left\{ -\kappa\,\ddot{\theta}_> - \mu\sin\theta_> \right\}$$
$$+ \delta\theta_<(L_{do}/2)\,\kappa\left\{ \dot{\theta}_<(L_{do}/2) - \dot{\theta}_>(L_{do}/2) \right\}$$
$$+ \frac{1}{2}\delta L_{do}\left\{ \frac{1}{2}\kappa\,\dot{\theta}_<^2(L_{do}/2) + \rho\sin\theta_<(L_{do}/2) - \frac{1}{2}\kappa\,\dot{\theta}_>^2(L_{do}/2) - |W_{do}| \right\}.$$
$$(3.55)$$

In this case, δL_{do} and $\delta\theta_<(L_{do}/2)$ are independent, since there is no specific boundary condition at $s = L_{do}/2$. As a consequence, the curvature is continuous where the ring crosses the domain boundary, and the first and the third term in the last line of (3.55) cancel, leaving a condition on the tangent angle at the crossing point. It is interesting to see, that in the limit of small stripe widths the problem becomes equivalent to a ring adhering to a topographical channel.

All in all, demanding that $\delta\mathcal{H}$ should vanish for all possible variations of $\theta_{\gtrless}$, $\theta_<(L_{do}/2)$ and L_{do} together with the constraints for the Lagrange multipliers, (3.52) and (3.53), results in a system of six coupled equations. A further complication occurring for the shapes II_1 and II_2 is, that a decomposition into almost independent curved segments is no longer possible, see Fig. 3.13(a). As a consequence, we mainly restrict our analysis to a numerical treatment using the SURFACE EVOLVER, which is described in the next paragraph and gives very accurate results, as we have checked for the case of the topographical channel.

The only ring morphology, which is, in comparison to the topographical channel, actually easier to calculate, is the shape II_0, cf. Fig. 3.13: For the chemical domain shape II_0 comprises a unique ring conformation, where the ring is entirely confined to the striped domain. Hence, for this shape the adhesion energy is constant, namely $-|W_{do}|L$, and the only contribution to the bending energy arises from the curved segments, whose length is free to adjust. The computation of the minimal bending energy for $L_{do} = L$ is carried out in the same way as for the topographical channel structure, and we can use the equations (3.20) and (3.21)

---

[5]For the calculation of the projected energy landscape $E_{tot}(L_{do})$, the variation with respect to L_{do} is not needed, rather, L_{do} is kept fixed and hence $\delta L_{do} = 0$. Nevertheless we perform the variation here to demonstrate, that the transversality condition is different in this case.

for the curved segment depicted in Fig. 3.5(c), where $\theta_{\inf} = \pi$, a_{st} is replaced by a_{do} and L_* is yet to be determined. The transversality condition arising from the variation of the length of the curved part is independent of the adhesion energy and enforces $\dot{\theta} = 0$ at the contact points of the ring and the domain boundaries. This new boundary condition, applied to (3.20), yields $c = 0$, so that the approximate results for the length of the curved segment and the bending energy found for $|w_{st}| \ll 1$, see (3.35), become *exact* for a ring confined to a striped domain. Therefore we can write

$$\frac{(E_{tot}^{\mathrm{II}_0})_{do}}{E_{do}} = 5.74 - |w_{do}|\frac{L}{a_{do}} \tag{3.56}$$

with the typical energy scale E_{do} and the reduced adhesion strength for the chemical domain

$$E_{do} \equiv \frac{\kappa}{a_{do}} \quad \text{and} \quad |w_{do}| \equiv \frac{|W_{do}|a_{do}^2}{\kappa} \quad \text{or} \quad |\tilde{w}_{do}| \equiv \frac{|W_{do}|L^2}{\kappa}. \tag{3.57}$$

3.3.3 Numerical energy minimization

The numerical analysis using the SURFACE EVOLVER proceeds analogously to the computation described in Section 3.2.4, replacing the surface structure, which is achieved in the following way: Adhered segments start and end on the domain boundaries so that the x component of the vertices, which separate adhered and non-adhered parts, is fixed to $x = \pm a_{do}/2$. Moreover, the vertices and edges belonging to an adhered segment are constrained to stay on the striped domain by demanding $|x| < a_{do}/2$.

The energy extrema for a given value of $|w_{do}|$ as well as the morphology boundaries are found in the same way as described in Section 3.2.2. The results for all three steps in the minimization procedure are illustrated exemplarily for $L/a_{do} = 20$ in Figs. 3.6(b), 3.9(c) and (d) and 3.11(c) and (d), respectively.

Also in this case, one can directly include a smooth, flattened version of the potential well, see Section 3.2.4, which leads qualitatively to the same results, but also produces artifacts as a consequence of the finite slopes at the boundaries of the domain.

3.3.4 Projected energy landscape

In Fig. 3.6(b), the numerical results for the minimized bending energy E_b of the shapes I , II_2, II_1 and II_0 normalized by E_{do} for $L/a_{do} = 20$, are plotted as a function of the adhered length L_{do}, which is measured in units of the stripe width a_{do}. A comparison of the two graphs, Figs. 3.6(a) and (b), demonstrates, that not only the morphologies a ring assumes, when adhering to a topographical channel
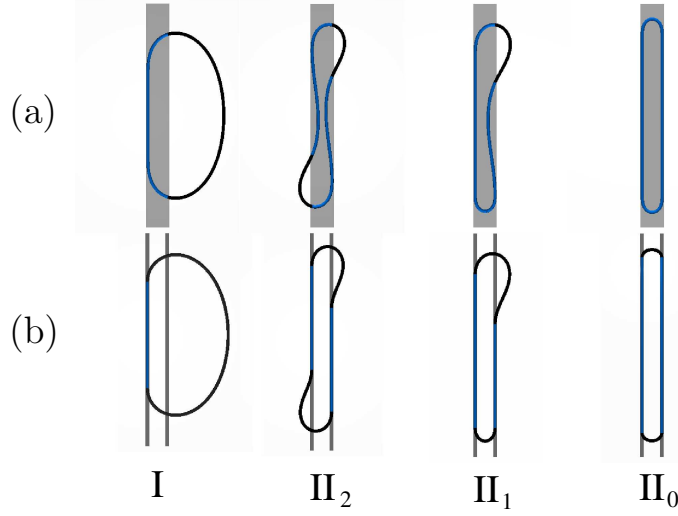
Figure 3.13: (a) Top views of all four stable morphologies of a ring adhered to a substrate with a chemically modified stripe as obtained by energy minimization for contour lengths $L/a_{do} = 20$. In comparison, the corresponding ring morphologies for the topographical stripe are shown in (b). In principle, there exists a realization of shape II_2, which is symmetric with respect to the horizontal axis, for the chemical stripe, too, see Fig. 3.4. Also in this case, the two realizations are (almost) equivalent, which is why we omit the symmetric version here.

or a chemical stripe (of the same width) are very much alike, cf. Fig. 3.13(a) and (b), but that the similarities sustain for the resulting energies, despite minor differences.

One immediately observes, that the bending energy curves computed for the chemical stripe appear to be shifted by a constant value compared to those for the topographical channel. The shift, which we denote by $\Delta \bar{L} = L_{do}/a_{do} - L_{st}/a_{st}$, can be attributed to the fact, that, in contrast to the channel, the stripe domain is also adhesive between its boundaries for $|x| < a_{do}/2$. Consequently, for the same ring shape adhered to either surface structure, L_{do} is always larger than L_{st}. For instance, a circular ring can adhere to the chemical domain with adhered length

$$(L_{do})_{circle} = 2R \arccos \left(1 - \frac{a_{do}}{R}\right) \qquad (3.58)$$

with $R = L/2\pi$ being the radius of the ring, whereas for the same ring adhered to a topographical stripe L_{st} is zero. For the circular ring morphology, the shift is thus maximal, namely $\Delta \bar{L} \simeq 5.19$, whereas it amounts to $\Delta \bar{L} \simeq 4.38$ for the morphology II_2, compare (3.37) with (3.56).

63

The last example already alludes to the rather different behavior as the adhered length becomes comparable to the contour length L. While the ring can adhere with its full length to the chemical stripe reaching a plateau in the bending energy, the maximal length adhered to the edges of the topographical stripe is $L - 2a_{st}$, where the ring is deformed into a rectangle of side length a_{st}, which gives rise to a diverging bending energy for L_{st}/a_{st} reaching $L/a_{st} - 2$ from below.

The projected energy landscape for a system characterized by the control parameters L/a_{do} and $|w_{do}|$ is obtained again by including the adhesion energy as

$$\frac{E_{tot}(L_{do}/a_{do})}{E_{do}} = \frac{E_b(L_{do}/a_{do})}{E_{do}} - |w_{do}|\frac{L_{do}}{a_{do}}. \tag{3.59}$$

3.3.5 Energy minima and stability

Fig. 3.9(c) shows, how the energies of the local extrema of the projected energy landscape in Fig. 3.6(b) for the system with the chemically striped substrate evolve as a function of the control parameter $|w_{st}|$ for $L/a_{do} = 20$. As a consequence of the observation, that one can almost reproduce Fig. 3.6(b) by shifting the curves in Fig. 3.6(a) by a constant value $\Delta\bar{L}$, the energy estimates obtained in Section 3.2.6 should also present a rough approximation of the system with a chemical domain, if supplemented by a term $-|w_{do}|\Delta L$ and if we substitute a_{st} by a_{do} and $|w_{st}|$ by $|w_{do}|$, respectively. This assumption is supported by the great resemblance of Figs. 3.9(a) and (c), and (b) and (d), respectively, apart from one exception: There is no unbinding transition for the chemical stripe.

This fact can be traced back to the following observation: For the topographical channel, the unbinding transition is a consequence of the transversality condition, which leads to a minimal value for $|w_{st}|$ above which a ring can gain energy by binding with a straight segment of length $L_{st} > 0$ to the edge of a step. As a consequence, the bending energy of shape I in Fig. 3.6(a) starts with small, but nonvanishing slope at $L_{st} = 0$. On the contrary, a ring can bind to the chemical domain without creating straight segments, and in particular, without deforming the circular conformation preferred by the bending energy, which is also reflected in the weaker form of the transversality condition for the chemical stripe (compare the results in (3.55) with those in (3.25)). This, in turn, produces a *continuous* rise of the slope of the bending energy of shape I starting at $L_{st} \simeq 5.19$ in Fig. 3.6(b). Consequently, the stability boundary of shape I is shifted compared to the channel to $|w_{st}| = 0$.

It is hard to analyze the stability of conformation I using the SURFACE EVOLVER, as soon as conformation II_1 becomes energetically favorable and vice versa. In this range of L_{do}, only a rather small deformation of the ring contour is sufficient to induce a transition between the two shapes, which can only partially be prevented by increasing the refinement of the discretization and by decreasing

the step size dL_{do} between subsequent conformations. This problem did not occur in the corresponding numerical analysis of shape I for the channel, because the second adhesive line was not included, so that the instability in the presence of the second edge could not be studied at all. Although explicit evidence is missing, one should expect that, unlike its counterpart for the topographical channel, the conformation I adhered to the chemical domain ceases to exist before $\Delta x = a_{do}$, see Fig. 3.5(a), which would correspond to $L_{do} = L$. Apart from that, the stability boundaries for the chemical stripe and for the topographical channel should be approximately the same.

3.3.6 Morphology diagram

Also the morphology diagram in the plane spanned by the reduced potential strength $|w_{do}|$ and L/a_{do}, as shown in Fig. 3.11(c) and (d), looks very similar to the morphology diagram for a topographical surface channel. In the previous section, we argued that the energy estimates for the equilibrium morphologies of the ring/channel-system derived in Section 3.2.6 should roughly apply to the system with the chemical domain, if a correction $-|w_{do}|\Delta\bar{L}$ is included that accounts for the additional adhered length of the ring segments that are located in between the boundaries of the chemical domain. Further we found, that $\Delta\bar{L}$ is approximately constant, which implies that this additional term is irrelevant when considering morphological transitions.

In fact, our results (3.45) for the transition between shapes I and II_0 (dot-dashed line), (3.46) for the appearance of bulged states (dotted line), and (3.47) for the transition between shapes I and II_2 (solid line) agree well with the numerical results (indicated by various black symbols). As already mentioned, the unbinding transition of shape I is absent for the chemical stripe domain.

Furthermore, the two morphology diagrams differ in the behavior of small rings. Rings with $L/a_{do} = \pi$ can fully bind to the chemical stripe without deformation and shapes I and II_0 become equivalent. The re-entrance of shape II_0 close to $L/a_{do} = \pi$ can be estimated by the following simple argument. For small rings, shape I can be approximated by a circle, so that its energy can be written as

$$\frac{(E_{tot}^{\mathrm{I}})_{do}}{E_{do}} \simeq 2\pi^2 \frac{a_{do}}{L} - |w_{do}|\frac{(L_{do})_{circle}}{a_{do}}. \tag{3.60}$$

Equating this energy with $(E_{tot}^{\mathrm{II}_0})_{do}/E_{do}$ given in (3.56) yields

$$|w_{do}|_{\mathrm{I-II}_0} \simeq \pi \left(2\pi^2 - 5.74\frac{L}{a_{do}}\right) \left(\frac{L}{a_{do}}\right)^{-2} \arccos\left(\frac{2\pi}{\bar{L}} - 1\right)^{-1} \tag{3.61}$$

shown as dashed line in Fig. 3.11(c).

Also in this case, we can reparametrize the ring/domain-system by exchanging $|w_{do}|$ with $|\tilde{w}_{do}|$, which is particularly convenient for applications where the polymer rings of a fixed size L adhere to a substrate with various domains of different widths a_{do}. The resulting morphology diagram is shown in Fig. 3.11(d).

3.4 Periodic surface stripes

An important generalization of our system, which can serve as a model for the atomic lattice structure of substrates, is the replacement of a single stripe or channel by a *periodic* chemical or topographical stripe pattern. However, we restrict our analysis to surfaces with equidistant step patterns, thereby the surface steps do not necessarily have to form channels, but could likewise be arranged e.g. as stairs.

Such surface structures drastically increase the number of metastable polymer shapes, so that, before presenting some general statements on the shapes arising on periodic patterns, let us start by adding just a single step to the structure shown in Fig. 3.3. We assume that the additional step is parallel to the other two steps and that the distance between neighboring steps is a_{st}, so that effectively, we only have to extend the adhesion potential (on top of the overall adhesion of the substrate), cf. Fig. 3.3, by a third thin potential well at $x = 3a_{st}/2$ or $x = -3a_{st}/2$. The resulting ring morphologies can be classified into conformations that adhere to one (I), two (II) and three (III) edges plus the unbound circular shape. Clearly, the shapes I are the same as for the single stripe, as the remaining steps (up to small corrections) do not contribute to the energy and also the unbinding transition applies without modifications to the three-step-system.

Moreover, if the ring binds to two edges, it should attain shapes that correspond to the morphologies II_0 and II_2 we found before[6], but now the ring can adhere either to two neighboring steps (at a distance a_{st}) or to the two outer steps (at a distance $2a_{st}$). Formally, we will distinguish these two cases via a superscript that indicates the distance between the relevant edges in units of a_{st}, for instance II_0^1, II_0^2 etc. The surface structure effectively contains two different 'stripe widths', namely, a_{st} and $2a_{st}$, which implies that the parametrization using $|\tilde{w}_{st}|$ instead of $|w_{st}|$ is more convenient. By analyzing the corresponding energy estimates $E_{tot}(|\tilde{w}_{st}|)$ one finds, that shape II_0^2 is always energetically favorable compared to shape II_2^1. Furthermore, II_2^2 becomes only stable for very large rings, i.e. $L/(2a_{st}) \gtrsim 27$, so that to a good approximation shapes with bulges can be neglected altogether.

---

[6]As in this section we are only interested in the stable morphologies of the system, we can safely neglect II_1, because even for two steps it is merely stable on the morphology boundary between conformations II_2 and II_0, see (3.46).
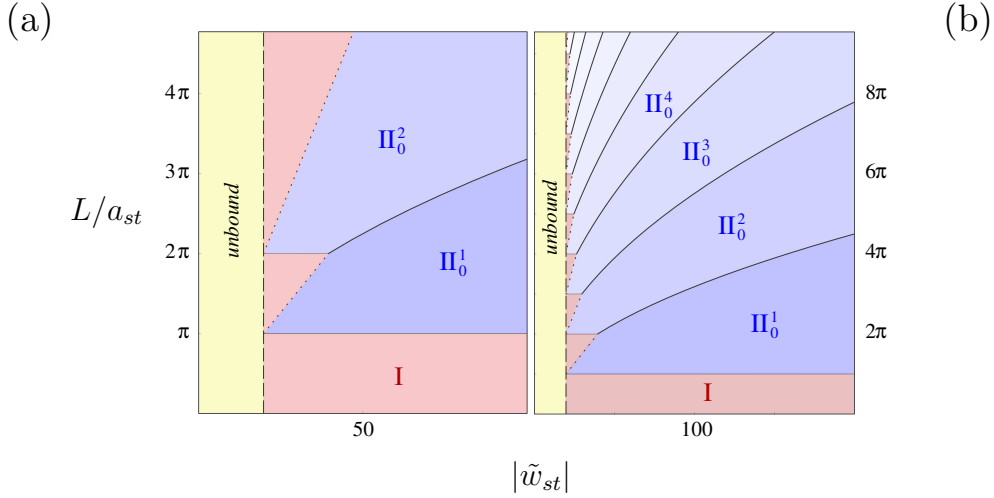
(a) (b)

Figure 3.14: Morphology diagrams of a ring adhered to a substrate with (a) three and (b) n surface equidistant steps at a distance a_{st} as a function of L/a_{st} and $|\tilde{w}_{st}|$. In comparison to the morphology diagram in Fig. 3.11, there are additional shapes II_0^n, with $n \geq 2$, that are stable in the regions colored in different nuances of blue. The dashed line marks the unbinding transition at $|\tilde{w}_{st}| = 2\pi^2$ and the solid and dotted lines indicate the morphology transitions estimated in (3.68) and (3.69), respectively.

The number of shapes can be further reduced by noticing that it should be always favorable to distribute the adhered length only among two instead of three edges, simply because the cost of bending energy is too high. As a consequence, conformations III are also ignored in our analysis.

To summarize, we end up with the unbound circular shape and the conformations I, II_0^1 and II_0^2 as possible stable morphologies of the three-step-system. For rather small rings with $L/a_{st} \leq 2\pi$, shape II_0^2 is inaccessible, so that the analysis in Section 3.2 and, in particular, the morphology diagram shown in Fig. 3.11(b) applies. Hence, in order to see an effect of the third step edge, the ring has to be larger than

$$L/a_{st} = 2\pi. \tag{3.62}$$

This relation therefore appears as horizontal morphology boundary in the morphological diagram. The dominating morphologies for large and small $|\tilde{w}_{st}| > 2\pi^2$ remain the shapes II_0^1 and I, respectively, but, in addition, there is an intermediate regime, where shape II_0^2 becomes stable, see Fig. 3.14(a). The corresponding morphology boundaries are roughly given by

$$|\tilde{w}_{st}|_{\text{I}-\text{II}_0^2} \simeq \pi\bar{L} \tag{3.63}$$

67

and

$$|\tilde{w}_{st}|_{\mathrm{II}_0^1 - \mathrm{II}_0^2} \simeq \bar{L}^2, \tag{3.64}$$

where, for simplicity, we approximated shape I by a circle

$$\frac{E_{tot}^{\mathrm{I}}}{\tilde{E}_{st}} \simeq 2\pi^2 \quad \text{with} \quad \tilde{E}_{st} \equiv \frac{\kappa}{L}, \tag{3.65}$$

which is justified for values of $|\tilde{w}_{st}|$ close to the unbinding transition at $|\tilde{w}_{st}| = 2\pi^2$, and likewise used the estimate for shape II_0 in (3.37) with the curved segments being described as semicircles of diameter a_{st} and $2a_{st}$, i.e.

$$\frac{E_{tot}^{\mathrm{II}_0^n}}{\tilde{E}_{st}} \simeq \frac{n}{\bar{L}} \left\{ 2\pi \frac{\bar{L}^2}{n^2} - |\tilde{w}_{st}| \left[\frac{\bar{L}}{n} - \pi \right] \right\} \quad \text{with } n = 1, 2. \tag{3.66}$$

The generalization to n equidistant steps is now straightforward. Again only the unbound circle and those shapes that bind to one (I) and two step edges (II_0^n) need to be considered. In accordance with the above convention, II_0^n refers to the shape a ring attains if bound to two edges, which are na_{st} apart. For a ring of contour length L, only states with $\bar{L} \geq \pi n$ are accessible, which is reflected in horizontal morphology boundaries

$$\bar{L} = \pi n \tag{3.67}$$

in the morphological diagram. The transition between shape I and the conformation II_0^n with the largest $n = n_{max}$ is found to be

$$|\tilde{w}_{st}|_{\mathrm{I} - \mathrm{II}_0^{n_{max}}} \simeq 2\pi \frac{\bar{L}}{n_{max}} \tag{3.68}$$

and the criterion $\bar{E}_{tot}^{\mathrm{II}_0^n} = \bar{E}_{tot}^{\mathrm{II}_0^{n-1}}$ gives a cascade of $n_{max} - 1$ further morphological transitions from shape II_0^n into shape II_0^{n-1} taking place at

$$|\tilde{w}_{st}|_{\mathrm{II}_0^n - \mathrm{II}_0^{n-1}} \simeq 2\pi \frac{\bar{L}^2}{n(n-1)} \quad (2 \leq n \leq n_{\max}). \tag{3.69}$$

The resulting morphology diagram is shown in Fig. 3.14(b).

3.5 Ring condensation

Finally, let us briefly comment on the application of our model to the widely studied field representing the condensation of semiflexible polymers, such as DNA and F-actin. In poor solvent or in the presence of condensing agents (charged)

Figure 3.15: Metastable racquet shape of a condensed ring with total energy (3.73). If the racquet-shaped segments become small, these conformations resemble rods, which is why in some cases they are referred to as rodlike shapes. The segments, that adhere to each other, are colored in blue.

semiflexible polymers can exhibit an effective interpolymer attraction, which can roughly be modelled by a condensation energy gain $W_{con} < 0$ per contact length. The effective potential describing the attraction between polymer segments, that are located at $\mathbf{r}(s_1)$ and $\mathbf{r}(s_2)$, with $0 \leq s_1 < s_2 \leq L$, now takes the form

$$V_{con}(|\mathbf{r}(s_1) - \mathbf{r}(s_2)|) = \begin{cases} W_{con} & \text{for } |\mathbf{r}(s_1) - \mathbf{r}(s_2)| < l, \\ 0 & \text{otherwise,} \end{cases} \tag{3.70}$$

where $|\mathbf{r}(s_1) - \mathbf{r}(s_2)|$ is the distance between the respective polymer segments. The range l is again of the order of the polymer diameter D. In comparison to the ring adsorbed to the striped structures, the length scale of the stripe width is absent, and the morphologies in the presence of a condensing potential are characterized by only *one* parameter, namely,

$$|\tilde{w}_{con}| = \frac{|W_{con}|L^2}{\kappa} \tag{3.71}$$

(if L_p is large such that thermal unbinding can be neglected [104]).

As for open polymers [14, 37], one expects the polymer ring to form a toroid, but with radius $L/2\pi n$, where n is the winding number, i.e. $n = 1$ is the trivial circular shape and $n = 2$ is the first condensed toroidal state with a total energy

$$\frac{(E_{tot})_{toroid}}{\tilde{E}_{con}} = 8\pi^2 - \frac{|\tilde{w}_{con}|}{2} \quad \text{with} \quad \tilde{E}_{con} = \frac{\kappa}{L}. \tag{3.72}$$

In addition, there is a class of metastable shapes with racquets, which were treated in detail in [95, 96]. Again, we consider only the shape with the least packing, see Fig. 3.15, whose energy can be calculated exactly in a very similar way as the conformations II. Its total energy reads

$$\frac{(E_{tot})_{rod}}{\tilde{E}_{con}} \simeq 18.18\sqrt{\frac{|\tilde{w}_{con}|}{2}} - \frac{|\tilde{w}_{con}|}{2} \quad \text{for } |\tilde{w}_{con}| \gtrsim 73.45, \tag{3.73}$$

where the lower bound for $|\tilde{w}_{con}|$ is again a result of the requirement that the adhered length has to be positive. Comparing the energies (3.72) and (3.73), one observes that the toroidal shape is always energetically favorable. The transition from a ring to this first condensed toroidal state occurs at

$$|\tilde{w}_{con}| = 12\pi^2. \tag{3.74}$$

For toroids with $n > 2$ the packing structure, which is commonly assumed to be hexagonal [14, 37, 95, 96], has to be taken into account, which goes beyond the scope of this thesis.

3.6 Conclusion and Outlook

As an example of how controlled adsorption of semiflexible polymers can be achieved by a structured substrate, we presented a complete classification of the morphologies of an adsorbed semiflexible polymer ring on a substrate containing an adhesive topographically or chemically striped domain. Both types of structures lead to a very similar behavior with a *discontinuous morphological transition* between the two dominant shapes I and II_0 and with intermediate bulged shapes II_1 and II_2 for large contour lengths. Estimates for all transition lines were derived, which could serve to determine material properties of the substrate or the polymer ring experimentally. The discontinuous transitions display shape hysteresis and are observable for persistence lengths exceeding the stripe width. For a periodic array of topographic steps we find a cascade of morphological shape transitions. Furthermore, the application of our model to the condensation of semiflexible polymer rings is briefly discussed.

The adhesion contrasts created by the surface structures considered in this chapter are equivalent to localized forces at the stripe boundaries, which pull the polymer into the region of higher adsorption strength. Therefore, the morphological transitions can also be interpreted as packaging transitions for semiflexible rings, e.g. into viral capsids [106]. An interesting two-dimensional system related to this problem is the adsorption of a semiflexible polymer ring on a substrate containing a chemically modified circular domain. Using similar techniques as in this chapter, one can study for instance under which conditions the ring fully adheres to the domain. Similar packaging effects have been examined for cylindrical sheets leading to spiral configurations [107].

Chapter 4

Conformations of zipped filaments

We study the zipping of two filaments with an attractive interaction and pinned filament ends based on experiments using microscopic pillar arrays. For the cases of weak and strong attraction between filaments, we analyze the influence of the filaments' stiffness and thermal fluctuations on the zipped equilibrium shape. Thereby we propose a scheme, by which the magnitude of the attraction between the filaments can be deduced from experimentally observed conformations. Our results should be applicable to actin filaments bundles induced by various crosslinker proteins and multivalent cations, but also to bundles formed by other types of semiflexible polymers.

4.1   Introduction

Eukaryotic cells contain a thin shell of crosslinked actin filaments only a few hundred nanometers thick just beneath the cell membrane. This so-called *actin cortex* is attached via pointwise anchors to the plasma membrane and accounts for the shape and the mechanical properties of a cell. Its internal structure is not uniform, but exhibits essentially two types of assemblies: There are networks of randomly linked filaments and bundles composed of aligned filaments, which are crosslinked by actin binding proteins, such as filamin, α-actinin or myosin, or by multivalent cations [3]. Actin bundles play a prominent role in filopodia, stress fibers and muscles and have been extensively studied experimentally focussing on various aspects, see e.g. Refs. [108, 109, 110, 111, 43, 44]. Besides *in vivo* studies, one way to explore the structural properties of the actin networks and bundles, quantitatively, is to construct *in vitro* model systems, which can be exposed to controlled mechanical or biochemical stimuli [112, 113, 114, 115, 116]. Following this strategy, it has been achieved to self-assemble a freely suspended actin network on arrays of microscopic pillars [116, 54], which mimic the focal contacts between the actin cortex and the membrane. In comparison to earlier experiments, e.g. Refs. [112, 113, 114, 115], the architecture of the resulting network is transparent and quasi two-dimensional reflecting the small thickness of the actin cortex, cf. Fig. 4.1.
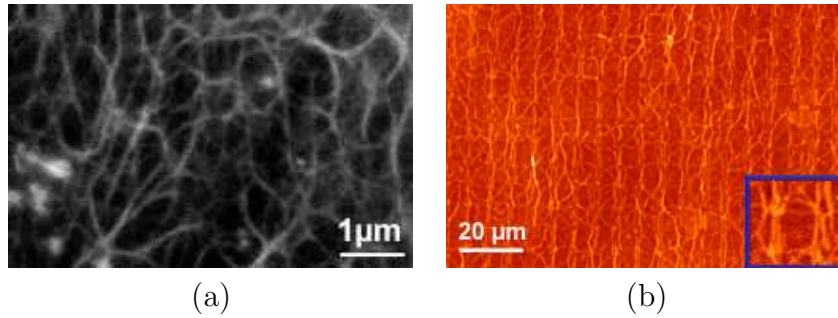
(a)   (b)

Figure 4.1: Fluorescence images of (a) a part of the actin cortex of a fibroblast and (b) an actin network suspended on a pillar array. Both images are taken from Ref. [116].

In this chapter, we study the bundling of single filaments, based on experiments described in Ref. [116] and ongoing experiments in the group of J. P. Spatz, see Fig. 4.1(b) and Fig. 4.2. In these experiments, the filaments are locally pinned to the heads of micron-sized pillars, which are several micrometers apart, imitating the confining boundary conditions of filaments within real networks. By addition of crosslinkers, the process of bundle formation can be initiated and directly be observed. After the first crosslink between two filaments is established, thermal shape fluctuations decay in the vicinity of the binding site, which enhances further nearby crosslinking. The length of the bundle grows bit by bit, and the filaments are *zipped up* [117].

In the limit of large binding energy and in the absence of thermal fluctuations, the zipping process only terminates, if the available contour length, which is constrained by the attachment to the pillar heads, is used up. In this state the zipped filaments assume a fork- or 'Y'-like shape with straight branches and sharp bends at the zipping point. For a real filament, however, even in the regime of strong attraction the conformational entropy will act against complete zipping resulting in small fluctuations around the 'Y'-like shape. On the other hand, for weak attraction one expects a rounded configuration governed by the bending rigidity. Consequently, the equilibrium conformation depends on the bending rigidities of the isolated and the bundled filaments, the crosslinker mediated attraction between the filaments, the temperature, and geometric constraints imposed by the experimental setup. By examining the equilibrated, partially zipped shape, it should be possible to extract the magnitude of the interfilament attraction which is an important characteristic of filament bundles. We present a theoretical description of the configurations arising in the regimes of weak and strong attraction, and develop methods to analyze experimental data on configurations of zipped filaments, which we expect to become available in the future.
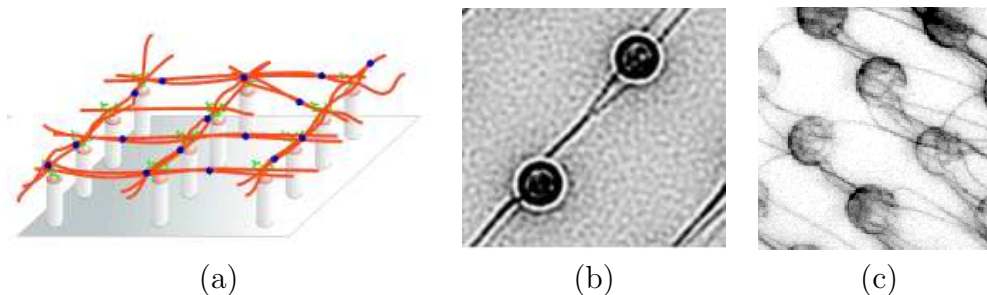
Figure 4.2: (a) Schematic setup of the experiments considered here [116]. The deactivated myosin, the actin filaments and the crosslinkers are shown in green, red and blue, respectively. (b) and (c) Micrographs of partially zipped configurations. [Figures (b) and (c) courtesy of Simon Schulz, University of Heidelberg]

The term 'zipping' occurs also in other biological contexts. In cells proteins unzip the double-stranded DNA, which has been studied experimentally e.g. in Refs. [118, 119, 120, 121]. The crucial difference, compared to actin filaments, is that the separated DNA strands are rather flexible, whereas actin filaments as well as actin bundles are semiflexible. On the other hand, a closely related effect is observed for stiff HbS fibers [122, 123], which has been used in [123] to estimate the involved attraction via a similar method as is presented here.

This chapter is organized as follows. Firstly, we will explain the experimental setup in more detail to elucidate the assumptions made in our calculations. After that, we discuss theoretically how the magnitude of the interfilament attraction can be extracted from the equilibrium conformation. In particular, the two cases of strong and weak attraction and the influence of thermal fluctuations are discussed. We end with a conclusion and an outlook on future work.

4.2 Experiments

The main motivation for the analysis presented in this chapter are experiments that were and are at present performed mainly by W. Roos and S. Schulz in the group of J. P. Spatz at the University of Heidelberg and the MPI for metals research in Stuttgart. The key issue of these experiments is the application of so-called microscopic pillar arrays [54], to which the actin filaments are pinned, leading to a network with a transparent architecture and well-defined, fixed boundary conditions.

The pillars are made of various materials, such as silicon, PDMS or epoxy, which differ in their optical and elastic properties, to act as templates for cell and filament adhesion, but also as force sensors. However, the forces detectable by the

pillars are well above the piconewton force range, which one expects to be relevant in zipping experiments, so that the deformation of pillars can be neglected. The pillars are typically a few micrometers in diameter, about $15\,\mu$m high and can be arranged on the underlying substrate according to the experimental needs, where lattice spacings are usually less than $10\,\mu$m.

In order to attach filaments irreversibly to the pillars, the pillar heads are coated with NEMHMM, a fragment of the motor protein myosin, which contains only the head and the neck and where the ATPase-function has been deactivated. In addition to this coating, the pillar heads and the supporting substrate are chemically treated to prevent unspecific binding of actin to the pillar array. The already polymerized actin filaments are either flown into the chamber containing the pillar array, where they bind to the pillar heads at random, or they are directly polymerized with one end attached to a pillar head. To visualize their contour the filaments are labeled with the fluorescent dye TRITC that also inhibits depolymerization. In a final step, the addition of crosslinkers, such as proteins like filamin or myosin II or simply multivalent cations, initiates the spontaneous formation of a quasi two-dimensional network, see Fig. 4.1(b) and Fig. 4.2. As can be seen in Fig. 4.1(b) and Fig. 4.2(c), the bundles exhibit a preferred direction due to the flow, by which the crosslinkers are injected. The images are taken via fluorescent (or confocal) microscopy.

For the following analysis, we are interested in the equilibrated bundle configurations within the established network. In particular, we are looking for configurations, where the bundle formation is restricted by the attachment of the filaments to the pillar heads, which provide definite boundary conditions for calculations. These partially zipped conformations result from the competition between the bending energy and the crosslinker-induced attraction between filaments, and, thus, encode information about the material properties. The procedure, how this information can be extracted, is the subject of the remaining sections of the present chapter.

4.3   Model

We consider an array of pillars, the fixed positions of which are denoted by P_i, $i \in \mathbb{N}$. The configurations we are particularly interested in are those, where two filaments are attached with one end to the same pillar head, say P_3, see Fig. 4.3. The two inextensible filaments are characterized by their bending rigidities κ_1 and κ_2 and the contour lengths between the attachment points, L_1 and L_2. As the anchorage of the filaments via the myosin fragment is irreversible, L_1 and L_2 are fixed. We can further assume, that the tangent orientations at the pillars are likewise predefined by this anchoring. Moreover, also the zipping of bundles
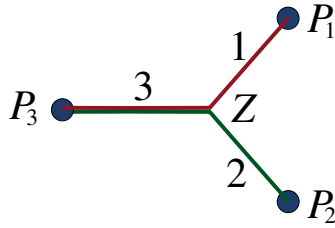
Figure 4.3: Schematic image of a configuration of two zipped filaments (shown in red and green), whose ends are attached to the pillar heads P_1, P_2 and P_3. The configuration consists of three branches (1, 2 and 3), which meet at the zipping point Z.

composed of a few filaments can occur. If we suppose that the bundles are stable and therefore well-defined during a zipping event, one can treat these bundles, in a first approximation, as single filaments with effectively larger bending rigidities.

The contour lengths L_1 and L_2 and the distances between the pillar heads $\overline{P_1 P_3}$ and $\overline{P_2 P_3}$ should be of the same order or smaller than the persistence length, so that interactions with the substrate can be neglected. This assumption is supported by the observation stated in Ref. [124], that the persistence length of the actin filaments might present an upper limit for the lattice spacing of pillar arrays, on which the formation of networks can take place.

By addition of crosslinker proteins or multivalent cations one can induce the partial zipping of the two filaments over a length L_{zip}, which gives rise to an adhesive energy gain $W_{zip} < 0$ per zipped length. We describe the crosslinker mediated attraction V_{zip} between the segments of two filaments, which are parametrized by position vectors $\mathbf{r}_1(s_1)$ and $\mathbf{r}_2(s_2)$, respectively, in the same manner as the effective potential used for the condensation in (3.70), namely by

$$V_{zip}(|\mathbf{r}_1(s_1) - \mathbf{r}_2(s_2)|) = \begin{cases} W_{zip} & \text{for } |\mathbf{r}_1(s_1) - \mathbf{r}_2(s_2)| < l, \\ 0 & \text{otherwise.} \end{cases} \tag{4.1}$$

The range l of the attractive potential depends on the molecular architecture of crosslinker proteins or the screening length l_{DH} for multivalent cations, respectively, cf. Chapter 1 for details. Filament segments, that are linked to each other by more than one crosslinker protein, are oriented parallel to each other.

In practice, the potential range l is very small compared to the other length scales involved, so that the zipped segment can be treated effectively as a single filament branch. The bending rigidity of the zipped segment κ_3 results from the bending rigidities of the separated filaments κ_1 and κ_2 either via

$$\kappa_3 = \kappa_1 + \kappa_2, \tag{4.2}$$

if the bound filaments are able to slide past each other, or via

$$\kappa_3 = (\kappa_1^{1/2} + \kappa_2^{1/2})^2, \tag{4.3}$$

if the zipped segment is modeled by a homogeneous cylinder, whose cross section area is equal to the sum of the single filaments cross section areas [125].

All in all, the configurations under consideration consist of three filament branches characterized by the parameters $\{\kappa_1, L_1 - L_{zip}\}$, $\{\kappa_2, L_2 - L_{zip}\}$ and $\{\kappa_3, L_{zip}\}$, which meet at the *zipping point Z*. For simplicity, we will refer to theses branches in the following as branch 1, 2 and 3, respectively, see Fig. 4.3. As the pillars have all the same height, the equilibrium conformation of the system is essentially planar and lies in the plane defined by the three pillar heads. However, the thermal shape fluctuations are not confined to this plane. Furthermore, the resulting configuration of the system strongly depends on the relative magnitude of three length scales, namely, the involved contour lengths L_i, the persistence lengths $L_{i,p}$ and the typical contact curvature radii at the zipping point $R_{i,co} \sim \sqrt{\kappa_i/|W_{zip}|}$, $(i = 1, 2)$, which already appeared in the preceding chapter. As already stated above, the experimental setup is such that the contour lengths L_i are always smaller than the persistence lengths $L_{i,p}$. In addition, if the persistence lengths $L_{i,p}$ are comparable to the contact radii $R_{i,co}$, i.e. $|W_{zip}|L_{i,p} \sim T$, zipped configurations should become rather unstable. We therefore demand that $L_{i,p} > R_{i,co}$. Finally, only two generic cases remain: If $R_{i,co}$ is small compared to L_i, the zipping induces sharp bends, whereas if $R_{i,co}$ is large compared to L_i, the conformations are rounded. We refer to these two regimes as strong and weak attraction, respectively. For both regimes, we first discuss the case of zero temperature or, equivalently, infinitely large persistence length $L_{i,p}$ and then include the influence of thermal fluctuations.

4.4 Strong attraction

4.4.1 Conformations at $T = 0$

If the attraction between the two filaments is so strong that it dominates over stiffness effects, i.e. if the contact radii are small compared to the contour lengths,

$$R_{i,co} \sim \sqrt{\kappa_i/|W_{zip}|} \ll L_i \quad i = 1, 2, \tag{4.4}$$

we can neglect the bending energy of the filaments. This is the easiest, but also roughest approximation that can be made. Under these conditions, the Hamiltonian of the system contains only the energy contribution due to attraction and is simply given by

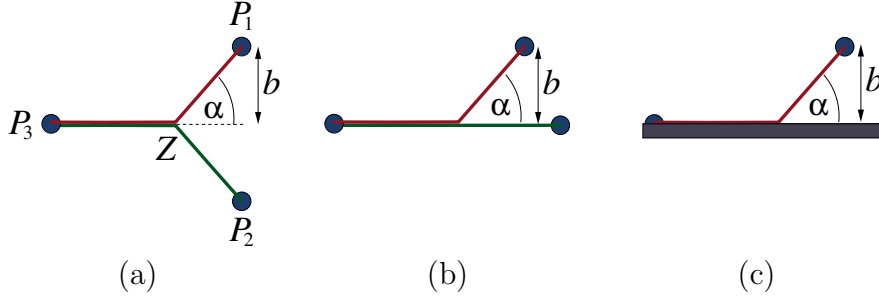$$\mathcal{H} \simeq -|W_{zip}|L_{zip}. \tag{4.5}$$

Figure 4.4: (a) Schematic image of a symmetric configuration of two partially zipped filaments, which are attached to the pillar heads P_1, P_2 and P_3, for the case of strong attraction. This scenario is closely related to the situations, (b) where one filament is very stiff or fully stretched between the pillars and (c) where one filament fixed at P_1 and P_3 adsorbs to a surface.

The mechanical equilibrium is reached, for the maximal value of L_{zip} subject to geometric constraints, that is, the positions of the pillar heads P_i as well as the contour lengths L_1 and L_2.

As mentioned in the introduction of this chapter, the influence of the bending rigidity as well as thermal fluctuations treated in the following causes the filaments to resist zipping. In this sense, the values for L_{zip} obtained in this section represent an upper limit $(L_{zip})_{max}$ for subsequent calculations that include the bending rigidity and thermal fluctuations. On the other hand, the results for L_{zip} are purely based on geometric considerations, which makes this scenario also the least desired in experiments, since it is not suited to determine material parameters, apart from the contour lengths of the filaments.

Symmetric setup

Suppose, the two filaments are identical and the pillars they are attached to are arranged symmetrically, such that

$$L_1 = L_2 \equiv L \ \text{ and } \ \kappa_1 = \kappa_2 \equiv \kappa \ \text{ and } \ \overline{P_1 P_3} = \overline{P_2 P_3}. \tag{4.6}$$

Then the adsorbed length L_{zip} becomes maximal, if all branches are tightened and the adsorbed segment of length $L_{zip} = \overline{P_3 Z}$ and, therefore, also the zipping point Z lie on the symmetry axis, which is defined by P_3 and the midpoint of the line $\overline{P_1 P_2}$, see Fig. 4.4(a).

If we define $b \equiv \overline{P_1 P_2}/2$, L_{zip} is found to be

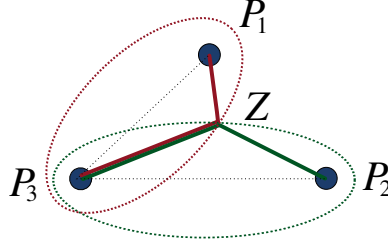$$(L_{zip})_{max} = L - \frac{b}{\sin \alpha}. \tag{4.7}$$

Figure 4.5: Schematic example of an asymmetric configuration of two partially zipped filaments as a result of strong attraction. The zipping point Z is identical to the crossing point of the two ellipses, which is the farthest apart from P_3.

The same result for L_{zip} is obtained for the setups shown in Fig. 4.4(b) and (c). In the first case, one of the filaments is infinitely stiff or, equivalently, $L_2 = \overline{P_2 P_3}$, which replaces the symmetry axis in Fig. 4.4(a). On the other hand, one can substitute the second filament altogether by an adhesive substrate surface, see Fig. 4.4(c), to which a filament with one end fixed at P_1 adsorbs. The angle α is then either a result of an attachment of the other end at the surface at P_3, or it arises because of infinite friction of the polymer at the surface [126][1].

Also for the other regimes examined in this chapter, the conformation arising in a symmetric setup is closely related to the constrained adsorption of a single filament to a wall with appropriate boundary conditions, see e.g. [105].

Asymmetric setup

Already for the general case, where $L_1 \neq L_2$ and $\overline{P_1 P_3} \neq \overline{P_2 P_3}$, the determination of L_{zip} is much more involved. Geometrically, one can interpret the zipping point Z as the crossing point of two ellipses, cf. Fig. 4.5(b). The two ellipses share one focus, namely P_3, while the other is P_1 and P_2, which is located at a distance

$$2c_1 \equiv \overline{P_1 P_3} \quad \text{and} \quad 2c_2 \equiv \overline{P_2 P_3}, \tag{4.8}$$

respectively. Their semimajor axes a_1 and a_2 are defined via the contour lengths as

$$2a_1 \equiv L_1 \quad \text{and} \quad 2a_2 \equiv L_2. \tag{4.9}$$

whereas the semiminor axes b_1 and b_2 are determined via the equation

$$b_1 \equiv \sqrt{(L_1/2)^2 - (\overline{P_1 P_3}/2)^2} \quad \text{and} \quad b_2 \equiv \sqrt{(L_2/2)^2 - (\overline{P_2 P_3}/2)^2}. \tag{4.10}$$

---

[1]If the polymer could glide over the surface and is not attached at a specific point at the surface, the angle α will adjust to ninety degrees to assume the maximal value for $L_{zip} = L_1 - b$.

With these definitions and by identifying P_3 with the origin of our coordinate system, so that P_3 and P_2 lie on the x-axis, we can parametrize the ellipses using the polar coordinates t_1 and t_2, $t_1, t_2 \in [0, 2\pi]$. Their crossing points are obtained by solving the equations

$$
\begin{aligned}
\cos\beta(c_1 + a_1 \cos t_1) + b_1 \sin\beta \sin t_1 &\overset{!}{=} c_2 + a_2 \cos t_2 \\
-\sin\beta(c_1 + a_1 \cos t_1) + b_1 \cos\beta \sin t_1 &\overset{!}{=} b_2 \sin t_2
\end{aligned}
\tag{4.11}
$$

for the variables t_1 and t_2, where β denotes the tilt angle between the ellipses. Finally, the adsorbed length L_{zip} is given by

$$
\begin{aligned}
(L_{zip})_{max} &= \max_i \sqrt{(c_1 + a_1 \cos t_1^i)^2 + (b_1 \sin t_1^i)^2} \\
&= \max_i \sqrt{(c_2 + a_2 \cos t_2^i)^2 + (b_2 \sin t_2^i)^2}
\end{aligned}
\tag{4.12}
$$

where $\{t_1^i, t_2^i\}$ is the set of solutions to (4.11).

4.4.2 Conformations at $T > 0$

Configurations, where filaments are maximally zipped together, as discussed in Section 4.4.1, involve a straightening of all three filament branches, which drastically reduces the entropy of the system as there exists only one possible configuration. If thermal fluctuations are taken into account, the persistence length also has to be included, namely,

$$
\sqrt{\kappa_i/|W_{zip}|} \ll L_i < L_{i,p} \quad i = 1, 2,
\tag{4.13}
$$

and the entropy, that causes thermally fluctuating filaments to resist full extension and therefore to act against the zipping, can no longer be neglected. As a result, the length along which the filaments are zipped together will become smaller, i.e. $L_{zip} < (L_{zip})_{max}$, to allow small shape fluctuations around the 'Y'-shaped configuration obtained in the previous section. Each branch is then additionally characterized by the distance between its end points called the end-to-end distance, which in our case is denoted by $L_{i,\parallel}$, for $i = 1, 2$, and by $L_{zip,\parallel}$ for the zipped branch, respectively. Accordingly, the three branches are described by $\{\kappa_i, L_i - L_{zip}, L_{i,\parallel}\}$, for $i = 1, 2$, and $\{\kappa_3, L_{zip}, L_{zip,\parallel}\}$, with $L_i - L_{zip} \geq L_{i,\parallel}$ and $L_{zip} \geq L_{zip,\parallel}$. The geometric constraints discussed in the previous section now apply to the end-to-end distances instead of the contour lengths.

The equilibrium configuration is found by minimizing the free energy of the system, which is given by

$$
T^{-1}\mathcal{F} = -\sum_{i=1,2} \log \mathcal{G}(L_i - L_{zip}, L_{i,\parallel}, L_{i,p}) - \log \mathcal{G}(L_{zip}, L_{zip,\parallel}, L_{3,p}) - T^{-1}|f_{zip}|L_{zip}.
\tag{4.14}
$$

The last term is the free energy due to attraction, where, in the presence of thermal fluctuations, the adhesion strength W_{zip} is replaced by free adhesion energy per crosslinked segment f_{zip}, see Refs. [104, 105]. Analogously to Section 3.2.9 it is approximately given by

$$|f_{zip}| \simeq |W_{zip} - W_{c,zip}|, \quad W_{c,zip} \sim \frac{T}{l^{2/3} L_{p,red}^{1/3}} \qquad (4.15)$$

where the critical potential strength $W_{c,zip}$ depends on the range of the potential well l, the temperature T and the reduced persistence length $L_{p,red}$ as given by

$$L_{p,red} \equiv \frac{1}{T} \frac{\kappa_1 \kappa_2}{\kappa_1 + \kappa_2}. \qquad (4.16)$$

We will assume that we are far from the thermal unbundling transition so that, even if W_{zip} is replaced by f_{zip}, the condition (4.13) still holds. Further, $\mathcal{G}$ is the radial distribution function of a polymer of contour length L, end-to-end distance $L_{\parallel}$ and persistence length L_p. Note that, in contrast to the free energy used in conventional stretching experiments, e.g. [22], where an external force couples to the end-to-end distance parallel to the force direction, the attraction strength W_{zip} couples here to the contour length of the zipped part. Hence, the end-to-end distances are tuned here by the adjustment of the zipped contour length.

The explicit expressions for $\mathcal{G}$ are usually rather complicated and the calculation becomes even more involved, if the coupling of the tangent vectors at the zipping point is included to assure continuity. As a simple approximation, we therefore neglect the bending energy contributions around the zipping point Z and assume free tangent orientations at the ends of all branches. Then we can use the estimate of $\mathcal{G}$ calculated in Ref. [127]

$$-\log \mathcal{G}(L, L_{\parallel}, L_p) \simeq \frac{1}{4L_p} \frac{L^2}{L - L_{\parallel}} \qquad (4.17)$$

valid for $L_{\parallel}/L$ close to one, which, according to the classification of force regimes presented e.g. in [32], is justified for the conditions (4.13). This approximation should altogether be reasonable for large $|W_{zip}|$ and $|f_{zip}|$ and small angle α, see Fig. 4.6.

Symmetric setup

We consider the symmetric setup specified in (4.6) and displayed in Fig. 4.6 so that the contributions to the free energy from branch 1 and 2 become identical, namely,

$$T^{-1}\mathcal{F} \simeq -2\log \mathcal{G}(L - L_{zip}, L_{\parallel}, L_p) - \log \mathcal{G}(L_{zip}, L_{zip,\parallel}, L_{3,p}) - T^{-1}|f_{zip}|L_{zip}. \quad (4.18)$$
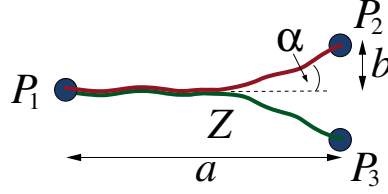
Figure 4.6: Schematic example of a symmetric configuration of two fluctuating filaments, which are partially zipped together and are attached to the pillar heads P_1, P_2 and P_3. For the case of strong attraction, the filaments weakly fluctuate around the 'Y'-shaped configuration illustrated in Fig. 4.4(a).

In principle, (4.18) contains four variables, i.e. the contour lengths and end-to-end distances of the two identical and the zipped branches, where we already eliminated one variable by imposing the conservation of the contour length L of the two filaments. On the other hand, the two end-to-end distances also depend on each other as they have to satisfy the condition

$$a = L_{zip,\shortparallel} + \sqrt{L_{\shortparallel}^2 - b^2} \tag{4.19}$$

generated by the relative positions of the pillar heads, cf. Fig. 4.6. For the variation of the free energy it is further useful to know how the above conditions relate the variations $\delta L_{\shortparallel}$ and $\delta L_{zip,\shortparallel}$, which is extracted from the variation of the above equation (4.19) as

$$\delta L_{zip,\shortparallel} = -\delta L_{\shortparallel}\frac{L_{\shortparallel}}{\sqrt{L_{\shortparallel}^2 - b^2}} = -\delta L_{\shortparallel}\frac{1}{\cos\alpha}. \tag{4.20}$$

The first variation of free energy (4.18) then reads

$$\delta\mathcal{F} = \delta L_{zip,\shortparallel}\left\{-\cos\alpha\frac{\delta\mathcal{F}}{\delta L_{\shortparallel}} + \frac{\delta\mathcal{F}}{\delta L_{zip,\shortparallel}}\right\} + \delta L_{zip}\left\{-\frac{\delta\mathcal{F}}{\delta(L - L_{zip})} + \frac{\delta\mathcal{F}}{\delta L_{zip}}\right\} \tag{4.21}$$

yielding two equations for $L_{zip,\shortparallel}$ and L_{zip}, which are given by

$$
\begin{aligned}
-\frac{a - L_{zip,\shortparallel}}{L_{\shortparallel}}\frac{(L - L_{zip})^2}{2L_p(L - L_{zip} - L_{\shortparallel})^2} + \frac{L_{zip}^2}{4L_{3,p}(L_{zip} - L_{zip,\shortparallel})^2} &\overset{!}{=} 0 \\
-\frac{(L - L_{zip})(L - L_{zip} - 2L_{\shortparallel})}{2L_p(L - L_{zip} - L_{\shortparallel})} + \frac{L_{zip}(L_{zip} - 2L_{zip,\shortparallel})}{4L_{3,p}(L_{zip} - L_{zip,\shortparallel})^2} - T^{-1}|f_{zip}| &\overset{!}{=} 0,
\end{aligned}
\tag{4.22}
$$

where $L_{\shortparallel}$ can be expressed via (4.19). The first equation in (4.22) from the variation with respect to the projected length represents the balance of the horizontal

component of the resulting forces at the zipping point, whereas the vertical component of the forces vanishes automatically due to the symmetry of the system. Furthermore, the second equation in (4.22) from the variation with respect to the contour length resembles the transversality conditions, which we derived in the previous chapter and which we will encounter again in the following section.

In experiments, $L_{zip,\shortparallel}$ can be measured, which, together with the knowledge of the contour length L and the persistence lengths L_p and $L_{3,p}$, suffices to determine L_{zip} and f_{zip} via (4.22).

Asymmetric setup

The general setup should be treated equivalently to the symmetric case replacing (4.19) by the condition that the zipping point coincides with the crossing point of two ellipses, cf. the second paragraph in Section 4.4.1. These conditions complicate the explicit analysis significantly, but should not introduce qualitatively new aspects, which is why we deliberately omit detailed calculations for this case.

4.5   Weak attraction

4.5.1   Conformations at $T = 0$

In this section, we analyze the case where the bending energy of the filaments governs the zipping of the filaments, i.e. where the contact radii become larger than the contour lengths,

$$L_i \ll R_{i,co} \sim \sqrt{\kappa_i/|W_{zip}|} \quad i = 1, 2. \tag{4.23}$$

Therefore, we have to supplement the Hamiltonian by adding a worm-like chain Hamiltonian for each of the three branches, namely

$$\mathcal{H} = \mathcal{H}^1_{\mathrm{wlc}} + \mathcal{H}^2_{\mathrm{wlc}} + \mathcal{H}^3_{\mathrm{wlc}} - |W_{zip}|L_{zip}. \tag{4.24}$$

Now the bending energies act against the zipping mechanism and thus against the maximization of L_{zip}. Heuristically, the sharp bends in the 'Y'-shaped configuration considered in Section 4.4.1, are now rounded by the bending rigidity. At equilibrium, the attraction energy and the sum of the bending energies are balanced through the adjustment of L_{zip}, so that the variation of $\mathcal{H}$ with respect to L_{zip} results in a relation by which the crosslinker strength $|W_{zip}|$ can be determined, if the involved bending rigidities are known.

For the minimization of $\mathcal{H}$, the attachment of the filament ends to the pillar heads, the fixed contour lengths of the filaments and (potentially) a fixed orientation of the filament ends have to be incorporated into the calculations as boundary conditions and constraints. In the parametrization via tangent angles, that we used in the previous chapter, the relative positions of the pillar heads introduce four constraints, which are imposed via Lagrange multipliers. On the other hand, the overall contour lengths of the filaments are automatically kept fixed by defining the ranges of the respective arc length variables s_i as $s_i \in [L_{zip}, L_i - L_{zip}]$ for $i = 1, 2$ and $s_3 \in [0, L_{zip}]$, whereas the tangent orientation at each pillar head is specified by the boundary values of the tangent angles. Alternatively, in the parametrization by displacement fields, see (1.4), the positions of the filament contours are measured as displacements $z_i(x)$ with respect to a reference axis. Hence, the positions and orientations of the filament ends are implied as boundary values of the displacement fields $z_i(x)$ and their derivatives $\partial_x z_i(x)$, whereas the constant contour lengths L_1 and L_2 have to be enforced by two Lagrange multipliers. Consequently, for this application the parametrization by displacement fields is more convenient, because it requires less Lagrange multipliers, that have to be determined in the end.

As mentioned in Chapter 1, the parametrization by displacement fields is only suitable for filament conformations without overhangs, i.e. the mapping between points on the reference axis and on the polymer backbone has to be unique. In addition, it is commonly assumed, that the displacement field changes only weakly along the reference axis so that terms of higher than quadratic order in the displacement field and its derivatives become negligible. The conditions (4.23) we are considering comply with these requirements.

Symmetric setup

As a first step, we assume the same symmetric setup as given in (4.6). The special feature of this setup is, that at equilibrium the zipped branch is straight defining a natural reference axis

$$z_3(x) = 0, \;\; x \in [0, L_{zip}], \tag{4.25}$$

where we identified P_3 with the origin of our coordinate system, while the position of the zipping point on the axis L_{zip} is yet to be determined. In order to inhibit kinks at the zipping point, we demand $z_i(L_{zip}) = 0$ and $\partial_x z_i(L_{zip}) = 0$ (i=1,2,3). As remaining boundary conditions for z_1 and z_2, we specify the positions of the remaining pillar heads as

$$P_1 = (a, b) \equiv (a, z_1(a)) \;\; \text{and} \;\; P_2 = (a, -b) \equiv (a, z_2(a)), \tag{4.26}$$

cf. Fig. 4.7(a) and, concerning the tangent orientation at the pillar heads, we choose the special case $\partial_x z_1(a) = -\partial_x z_2(a) = v$, if the tangents are fixed, and
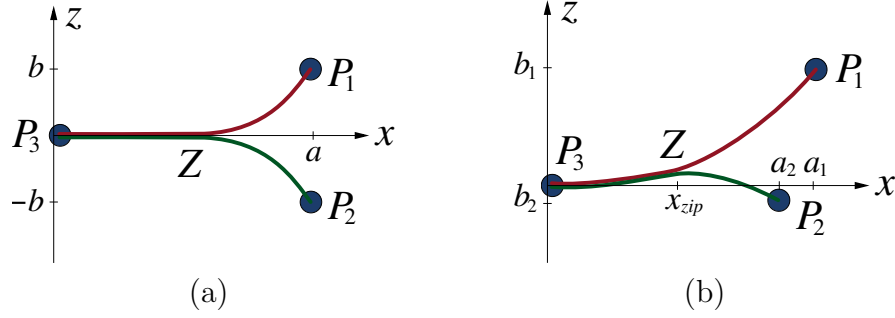
Figure 4.7: Schematic image of (a) a symmetric and (b) an asymmetric setup of two semiflexible filaments attached at the pillar heads P_i, that are zipped together between P_3 and Z. As indicated in the pictures, for weak interfilamental attraction, the resulting curvature radius at the zipping point is bigger than the contour lengths of the filaments.

demand $\partial_x^2 z_i(a) = 0$, $i = 1, 2$, if the tangent orientations are free. Furthermore, z_1 and z_2 have to obey the constraint

$$L - L_{zip} \overset{!}{=} \int_{L_{zip}}^a dx \sqrt{1 + (\partial_x z_i(x))^2} \simeq a - L_{zip} + \frac{1}{2} \int_{L_{zip}}^a (\partial_x z_i(x))^2, \quad i = 1, 2, \quad (4.27)$$

to conserve the contour length in either branch. Since the Hamiltonian (1.4) as well as the above constraints depend only on the absolute value of the displacement fields z_1 and z_2, the contributions from branch 1 and 2 to the Hamiltonian are identical and we can write

$$\mathcal{H}\{z\} \simeq \int_{L_{zip}}^a dx \{\kappa(\partial_x^2 z(x))^2 + \mu(\partial_x z(x))^2\} - \mu(L - a) - |W_{zip}| L_{zip} \quad (4.28)$$

with

$$z_1(x) = -z_2(x) \equiv z(x), \quad x \in [L_{zip}, a]. \quad (4.29)$$

Here, the Lagrange multiplier μ can be interpreted as a force in x-direction, which enforces the horizontal confinement of the filaments. The variation with respect to z yields the Euler-Lagrange equation for the displacement field z

$$\partial_x^4 z(x) - k^2 \partial_x^2 z(x) = 0 \quad \text{with } k^2 \equiv \mu/\kappa, \quad (4.30)$$

which is solved by the Ansatz

$$z(x) = \frac{A_1}{k^2} \sinh(kx) + \frac{A_2}{k^2} \cosh(kx) + A_3 x + A_4, \quad (4.31)$$

where the constants A_i, $i = 1, ..., 4$, are determined by imposing the boundary conditions, see App. C. In addition, $\mathcal{H}$ has to be varied with respect to L_{zip} to obtain the transversality condition

$$\partial_x^2 z(L_{zip}) = \sqrt{|W_{zip}|/\kappa} \tag{4.32}$$

where we have applied the same method as in the previous chapter, cf. (3.26), to set $\delta z(L_{zip}) = -\delta L_{zip}\partial_x z(L_{zip})$. In this case, equation (4.32) establishes a relation between the equilibrium shape $z(x)$ of the filaments, in particular, the curvature at the zipping point, and the ratio between W_{zip} and κ, which can be used to determine the effective crosslinker strength W_{zip}, if κ is known. In App. C the explicit results for the transversality condition for fixed (C.3) and free (C.6) tangent orientation at the ends are given. These relations and likewise the displacement field z still depend on the unknown variable k, see (4.30), which is either calculated numerically by solving the constraint (4.27) or by fitting experimentally observed conformations.

Asymmetric setup

For the general asymmetric case, which is schematically shown in Fig. 4.7(b), we fix the ends of the filaments as

$$z_i(a_i) = b_i, \quad i = 1, 2, \quad \text{and} \quad z_3(0) = 0, \tag{4.33}$$

while again, if the setup is such that the tangents are fixed at the ends, we set $\partial_x z_i(a_i) = v_i$, $i = 1, 2$, and $\partial_x z_3(0) = 0$, and postulate that $\partial_x^2 z_i$ has to vanish at the ends, if the tangent orientations are free. At the zipping point, we postulate the continuity of the displacement field and its derivative

$$z_i(x_{zip}) \equiv z_{zip} \quad \text{and} \quad \partial_x z_i(x_{zip}) \equiv v_{zip}, \quad i = 1, 2, 3, \tag{4.34}$$

but x_{zip}, z_{zip} and v_{zip} are free to adjust. Accordingly, the constraints (4.27) now take the form

$$L_i - a_i \simeq \tfrac{1}{2} \int_0^{x_{zip}} dx (\partial_x z_3)^2 + \tfrac{1}{2} \int_{x_{zip}}^{a_i} dx (\partial_x z_i)^2, \quad i = 1, 2, \tag{4.35}$$

where we have already expanded the square root, and the corresponding Hamiltonian is given by

$$\begin{aligned}
\mathcal{H} = \sum_{i=1,2} &\left\{ \tfrac{1}{2} \int_{x_{zip}}^{a_i} dx \{ \kappa_i (\partial_x^2 z_i)^2 + \mu_i (\partial_x z_i)^2 \} - \mu_i(L_i - a_i) \right\} \\
&+ \tfrac{1}{2} \int_0^{x_{zip}} dx \{ \kappa_3 (\partial_x^2 z_3)^2 + (\mu_1 + \mu_2 - |W_{zip}|)(\partial_x z_3)^2 \} - |W_{zip}| x_{zip}.
\end{aligned} \tag{4.36}$$

Here, the approximate zipped length

$$L_{zip} \simeq x_{zip} + \tfrac{1}{2} \int_0^{x_{zip}} dx (\partial_x z_3)^2 \qquad (4.37)$$

appears in the Hamiltonian via x_{zip} and an extra term in the integral in the second line. The variation of the Hamiltonian results in the same type of Euler-Lagrange equation for the z_i as before (4.30), in which k is to be replaced by the respective k_i with

$$k_1^2 \equiv \mu_1/\kappa_1, \quad k_2^2 \equiv \mu_2/\kappa_2 \quad \text{and} \quad k_3^2 \equiv (\mu_1 + \mu_2 - |W_{zip}|)/\kappa_3. \qquad (4.38)$$

Furthermore, the transversality condition associated with the variation of x_{zip} is found to be

$$|W_{zip}| = \{\kappa_3(\partial_x^2 z_3(x_{zip}))^2 - \kappa_1(\partial_x^2 z_1(x_{zip}))^2 - \kappa_2(\partial_x^2 z_2(x_{zip}))^2\}/\{2 + v_{zip}^2\} \quad (4.39)$$

and two conditions that originate from the demand that $\delta\mathcal{H}$ has to vanish for all possible variations δz_{zip} and δv_{zip}, namely,

$$|W_{zip}|v_{zip} = \kappa_1\partial_x^3 z_1(x_{zip}) + \kappa_2\partial_x^3 z_2(x_{zip}) - \kappa_3\partial_x^3 z_3(x_{zip}) \qquad (4.40a)$$

and

$$\kappa_1\partial_x^2 z_1(x_{zip}) + \kappa_2\partial_x^2 z_2(x_{zip}) - \kappa_3\partial_x^2 z_3(x_{zip}) = 0, \qquad (4.40b)$$

respectively. In terms of mechanical quantities, these conditions are interpreted as the balance of forces in x- and z-direction and the balance of torques perpendicular to the xz-plane at the zipping point. For the symmetric setup we had $\delta z_{zip} = 0$, which implies that (4.40a) is absent, and $\delta(\partial_x z_i(x_{zip})) = -\delta x_{zip}\partial_x^2 z_i(x_{zip})$ leading to a combination of (4.39) and (4.40b), that strongly resembles (4.39), but has the opposite sign on the left hand side. In this way, the results for the symmetric case discussed in the previous paragraph are recovered.

In order to determine W_{zip}, one has to proceed just as in the previous paragraph: With the ansatz (4.31) and the boundary conditions specified above one obtains the $z_i(x, k_i)$ with coefficients very similar to those given in App. C. The k_i can then be extracted from a fit of the experimentally observed equilibrium conformations. In principle, the knowledge of the k_i already suffices for the determination of W_{zip} in this case, since

$$\kappa_1 k_1^2 + \kappa_2 k_2^2 - \kappa_3 k_3^2 = |W_{zip}|. \qquad (4.41)$$

For the symmetric case, this relation reduces to the definition of k in eq. (4.30).

4.5.2 Conformations at $T > 0$

If the influence of thermal fluctuations is taken into account we have to replace again the crosslinker-mediated adhesion strength W_{zip} by the free adhesion energy per crosslinked segment f_{zip} given in eq. (4.15). Assuming that

$$L_i \ll \sqrt{\kappa_i/|f_{zip}|} < L_{i,p} \quad i = 1, 2,\tag{4.42}$$

the results of the preceding calculation remain to be valid also for $T > 0$.

4.6 Conclusion and Outlook

We considered the configurations of two partially zipped actin filaments, whose ends are locally pinned to pillar arrays, for the cases of strong and weak attraction, which can be mediated, for example, by crosslinker proteins or counterions. The different regimes were classified according to the relative magnitude of involved contour lengths L_i, the persistence lengths $L_{i,p}$ and the typical contact curvature radii at the zipping point $R_{i,co}$, which are related to the square root of the ratio between the bending rigidities and the effective attraction strength: The strong attraction regime was thereby identified with the case, where the contact radii are small compared to the contour lengths, $R_{i,co} \ll L_i$, whereas the weak attraction regime was characterized by $R_{i,co} \gg L_i$. For both regimes, we established methods to extract the effective interfilament attraction strength from the experimentally observable equilibrium shapes for the zero temperature case and discussed the influence of thermal fluctuations.

The motivation of this theoretical analysis are experiments in the group of J. P. Spatz, to which our results shall be applied in the future. In these experiments, the filaments are locally pinned to microscopic pillar arrays, which give rise to well-defined boundary conditions advantageous for a comparison with theoretical calculations. By means of the results presented in this chapter, it should be possible to measure the attraction strength mediated by multivalent cations, such as Mg^{2+}, and various actin binding proteins, such as fimbrin or α-actinin, which is an important property of actin bundles. It is also straightforward to apply our results to bundles formed by other types of semiflexible polymers, e.g. protein fibers or microtubules. Furthermore, in an alternative experimental setup, the filaments are attached to optically trapped beads instead of pillars, so that the arising forces can directly be measured, which is easily incorporated in our theoretical analysis. Finally, it would also be interesting to extend this work to active crosslinkers, such as myosin II, focusing more on dynamic aspects.

Chapter 5

Summary and Outlook

In the preceding chapters, various aspects concerning the conformations of individual semiflexible polymers were considered. We discussed the concept of the persistence length for the classification of semiflexible polymers and how it can be related to the renormalization of the bending rigidity. On the basis of two examples, namely, the adsorption of polymer rings on structured substrates and the constrained bundling of actin filaments, we demonstrated how the resulting morphologies can be controlled for technological applications and how they can be used to extract information about biological systems.

The topic of Chapter 2 was the relation between the persistence length of semiflexible polymers and bending rigidity renormalization. Therefore, we first reviewed existing definitions for the persistence length based on tangent correlations for polymers and on the perturbatively renormalized bending rigidity for membranes, see Section 2.2. A comparison of both definitions for semiflexible polymers demonstrated their incompatibility. In order to analyze this discrepancy in more detail, we described semiflexible polymers by a discretized worm-like chain model, which is equivalent to the one-dimensional classical Heisenberg model as explained in Section 2.3. The advantage of this description is, that the renormalization of the bending rigidity and the tangent correlation function are exactly computable in arbitrary dimensions. The renormalization of the bending rigidity was obtained using an exact real-space functional renormalization group (RG) transformation, see Section 2.4. The RG flows (2.25) or (2.26), as illustrated in Fig. 2.4, cover the behavior of a semiflexible polymer from the rigid regime on short length scales to the flexible regime on large length scales, where the renormalized bending rigidity vanishes exponentially, cf. (2.26). We defined the persistence length by the asymptotic behavior on large length scales. This definition generalizes the conventional definition based on the exponential decay of the two-point tangent correlation function (2.1) and gives identical results for the persistence length, compare (2.1) with (2.27). Furthermore, it is qualitatively different from the definition commonly used for the persistence length of fluid membranes based on a perturbative renormalization of the bending rigidity: Our definition reflects the behavior on large length scales, whereas the one used in [73, 74, 75, 76, 77, 78, 79, 80] contains only the short range behavior accessible by perturbative RG techniques. For semiflexible polymers, this discrepancy was

demonstrated explicitly by the comparison between our result for the persistence length (2.27) and the one deduced from a renormalized bending rigidity, which was obtained via a perturbative momentum-shell RG analysis of the worm-like chain model, see (2.3).

The application of the renormalization procedure, which was presented here, to two-dimensional fluid membranes is impeded by the more involved differential geometry of two-dimensional surfaces and remains a challenge for the future. However, our analysis suggests that the behavior of the RG flow of the bending rigidity on large length scales is essential for the determination of the persistence length for membranes as well.

In Chapter 3, we studied an example of how a systematic shape control of adsorbed semiflexible polymers can be achieved by making use of surfaces containing affinity patterns. In particular, we considered semiflexible polymer rings adsorbed to substrate surfaces containing (i) a topographical channel and (ii) a chemically modified stripe, schematically shown in Figs. 3.3 and 3.12. For either type of structure, we presented a complete classification of all equilibrium morphologies, cf. the snapshots in Fig. 3.13, by calculating a projection of the energy landscape, see Sections 3.2.5 and 3.3.4, determining its local minima in Sections 3.2.6 and 3.3.5 and discussed their stability in Sections 3.2.7 and 3.3.5. The results for the two systems were found to be very similar and were summarized in morphology diagrams, shown in Fig. 3.11: In both cases, the morphology diagrams are dominated by discontinuous morphological transitions between the weakly deformed circular shape I and the confined elongated shape II_0. The intermediate shapes with one and two bulges II_1 and II_2 become stable for rings that are large compared to the stripe width. In addition, the system with the topographical stripe leads to an unbinding transition, which is also known for vesicles adhering to a planar substrate with an adhesion potential of very small range [102, 103]. We derived analytical estimates for all transition lines, see Sections 3.2.8 and 3.3.6, which provide the basis to determine material parameters of the polymer ring or the adhesive domain experimentally. Furthermore, they demonstrate how the ring shapes can be manipulated systematically by the control parameters in (bio-)nanotechnological applications. Including thermal fluctuations it was found, that the transitions display a complex shape hysteresis, if the persistence length of the polymer ring is larger than the stripe width, cf. Section 3.2.9.

We extended our analysis to periodic arrays of topographic steps in Section 3.4, for which a cascade of transitions between elongated shapes was found, see Fig. 3.14. Furthermore, in Section 3.5, we briefly discussed the application of our model to condensation transitions of closed semiflexible polymers induced by attractive interactions.

An interesting system to study in the future is the adsorption of a semiflexible polymer ring onto a surface with a small circular adhesive domain. The adhesion

contrast at the domain boundaries generates local forces, which pull the ring into the region of higher adsorption strength. These forces can be compared with those involved in packaging transitions, which are relevant for the packaging of DNA into viral capsids [106]. Moreover, the resulting polymer morphologies should be similar to those observed for cylindrical semiflexible sheets confined into cylindrical tubes [107].

Finally, in the Chapter 4, we focused on the theoretical description of experiments, which investigate the zipping of actin filaments using a biomimetic model of the actin cortex. In the experiments performed in the group of J. P. Spatz, see Section 4.2, the filaments are locally anchored to the heads of micron-sized pillars mimicking the confining boundary conditions of filaments within real networks. The pillars are arranged with a lattice spacing of several micrometers resulting in a quasi two-dimensional network and have a height which is comparable or greater than the filament length. By adding crosslinkers or multivalent cations, the zipping of neighboring filaments can be initiated.

The aim of our theoretical analysis was to show how one can extract the magnitude of the attraction between the filaments from experimentally observable conformations. Therefore, we considered the configurations of two partially zipped actin filaments distinguishing between the cases of strong and weak attraction, see Section 4.3. These two regimes were characterized by the ratio of the involved contour lengths of the filaments and the typical contact curvature radii at the zipping point, which are proportional to the square root of the bending rigidities of the filaments divided by the effective attraction strength: For strong attraction, the contour lengths are large in comparison to the typical contact curvature radii resulting in conformations with sharp bends, cf. Section 4.4. By contrast, the conformations are rounded for weak attraction, which is specified by large contact curvature radii compared to the contour lengths of the filaments, see Section 4.5. Both regimes were discussed for the zero temperature case and in the presence of thermal fluctuations.

With the help of our results, it should be possible to determine the attraction strength of various actin binding proteins, e.g. fimbrin or α-actinin, or multivalent cations like Mg^{2+}. However, they should also apply to bundles formed by other types of semiflexible polymers, such as protein fibers or microtubules. The forces generated by the zipping of the filaments could be measured directly using an alternative experimental setup, where the pillars are replaced by optically trapped beads. Likewise, the zipping caused by active crosslinkers, such as myosin II, would be an interesting extension of our system including also active processes.

Appendix

Appendix A

Differential geometry of membranes

The conformation of a membrane is mathematically described by the embedding functions $\mathbf{R}(s_1, s_2)$ defining a surface in three-dimensional space. s_1 and s_2 constitute the two-dimensional (internal) coordinate system, such as s or x for the case of a filament. To each point (s_1, s_2), one can assign two tangent vectors, $\mathbf{R}_1$ and $\mathbf{R}_2$, and a normal vector $\mathbf{N}$ as

$$\mathbf{R}_i = \partial_{s_i} \mathbf{R} \quad \text{with } i = 1, 2 \quad \text{and} \quad \mathbf{N} = \frac{\mathbf{R}_1 \times \mathbf{R}_2}{|\mathbf{R}_1 \times \mathbf{R}_2|}. \tag{A.1}$$

The metric tensor

$$g_{ij} = \mathbf{R}_i \cdot \mathbf{R}_j, \tag{A.2}$$

its inverse g^{ij} and its determinant g complete the list of quantities needed to define the quantities contained in the Hamiltonian (1.9): The infinitesimal area element is given by

$$dA = \sqrt{g} ds_1 ds_1. \tag{A.3}$$

From the curvature tensor h_{ij}

$$h_{ij} = \mathbf{N} \cdot (\partial_{s_i} \partial_{s_j} \mathbf{R}) \tag{A.4}$$

one obtains the mean curvature M as its trace and the Gaussian curvature G as its determinant, namely

$$M = \frac{1}{2} \text{tr}(g^{ik} h_{kj}), \ G = \det(g^{ik} h_{kj}). \tag{A.5}$$

In this convention the mean curvature of a sphere is negative. This is why sometimes M is defined with a negative sign.

The metric tensor g_{ij} and the curvature tensor h_{ij} are both symmetric, so that altogether there are six functions of the coordinates (s_1, s_2) characterizing g_{ij} and h_{ij}. For a given surface $\mathbf{R}(s_1, s_2)$, these functions satisfy the compatibility equations of Mainardi, Codazzi and Gauss. If the diagonal components of the metric and its determinant are positive, these equations constitute even sufficient conditions for the surface to be uniquely determined by $\mathbf{R}(s_1, s_2)$, except for global rotations and translations (Bonnet Theorem). By contrast, a one-dimensional space curve is in this sense simply determined by its set of unit tangent vectors $\mathbf{t}(s)$. For a comprehensive introduction into the differential geometry of surfaces, see e.g. Ref. [128].

Appendix B

Explicit expressions for the configurations II

In this Appendix, the explicit expressions for the functions $f_1(p)$, $f_2(p)$ and $f_3(p)$ occurring in equations (3.22) and (3.23) in the analytical minimization of the segments depicted in Fig. 3.5(b) and (c) are provided. The functions for the case of a segment with or without bulge, cf. Fig. 3.5(b) and (c), are decorated with an index B and $\not{B}$, respectively. For the bulged shape one finds

$$f_1^{\mathrm{B}}(p) = \frac{2}{(1+p)^{1/2}} K\left(\frac{2}{1+p}\right) - \frac{1}{p^{3/2}} {}_3F_2[\mathcal{B}_1(p)] + 4p^{1/2} {}_3F_2[\mathcal{B}_2(p)]$$

$$f_2^{\mathrm{B}}(p) = -\frac{\pi}{(4p)^{3/2}} {}_2F_1[\mathcal{B}_3(p)] + \frac{2}{p^{1/2}} {}_3F_2[\mathcal{B}_4(p)] - \frac{8p^{3/2}}{3} {}_3F_2[\mathcal{B}_5(p)] \qquad \text{(B.1)}$$

$$f_3^{\mathrm{B}}(p) = \pi p^{1/2} {}_2F_1[\mathcal{B}_6(p)] + \frac{1}{p^{1/2}} {}_3F_2[\mathcal{B}_7(p)] + \frac{4p^{3/2}}{3} {}_3F_2[\mathcal{B}_8(p)]$$

and for the shape without bulge

$$f_1^{\not{B}}(p) = 4\left(1 + \frac{1}{p}\right)^{-1/2} F\left(\frac{\pi}{4}, \frac{2}{1+p}\right)$$

$$f_2^{\not{B}}(p) = -\frac{\pi}{4p} {}_2F_1[\mathcal{A}_1(p)] + 2 {}_3F_2[\mathcal{A}_2(p)] \qquad \text{(B.2)}$$

$$f_3^{\not{B}}(p) = 4\left(1 + \frac{1}{p}\right)^{1/2} E\left(\frac{\pi}{4}, \frac{2}{1+p}\right)$$

containing the elliptic integral of the first kind and the second kind, $F(\phi, k)$ and $E(\phi, k)$, and the hypergeometric functions ${}_mF_n[(a_1, ..., a_m), (b_1, ..., b_n); z]$, for definitions see e.g. Ref. [83]. For the bulged segment the arguments of the hypergeometric functions are given by

$$\mathcal{B}_1(p) = \{(\tfrac{3}{4}, 1, \tfrac{5}{4}), (\tfrac{3}{2}, \tfrac{3}{2}); \tfrac{1}{p^2}\} \qquad \mathcal{B}_5(p) = \{(\tfrac{1}{2}, 1, \tfrac{3}{2}), (\tfrac{5}{4}, \tfrac{7}{4}); p^2\}$$

$$\mathcal{B}_2(p) = \{(\tfrac{1}{2}, \tfrac{1}{2}, 1), (\tfrac{3}{4}, \tfrac{5}{4}); p^2\} \qquad \mathcal{B}_6(p) = \{(-\tfrac{1}{4}, \tfrac{1}{4}), 1; \tfrac{1}{p^2}\}$$

$$\mathcal{B}_3(p) = \{(\tfrac{3}{4}, \tfrac{5}{4}), 2; \tfrac{1}{p^2}\} \qquad \qquad \mathcal{B}_7(p) = \{(\tfrac{1}{4}, \tfrac{3}{4}, 1), (\tfrac{3}{2}, \tfrac{3}{2}); \tfrac{1}{p^2}\} \qquad \text{(B.3)}$$

$$\mathcal{B}_4(p) = \{(\tfrac{1}{4}, \tfrac{3}{4}, 1), (\tfrac{1}{2}, \tfrac{3}{2}); \tfrac{1}{p^2}\} \qquad \mathcal{B}_8(p) = \{(\tfrac{1}{2}, \tfrac{1}{2}, 1), (\tfrac{5}{4}, \tfrac{7}{4}); p^2\}.$$

For the segment without bulge they are

$$\mathcal{A}_1(p) = \{(\tfrac{3}{4}, \tfrac{5}{4}), 2; \tfrac{1}{p^2}\}$$

$$\mathcal{A}_2(p) = \{(\tfrac{1}{4}, \tfrac{3}{4}, 1), (\tfrac{1}{2}, \tfrac{3}{2}); \tfrac{1}{p^2}\}. \qquad \text{(B.4)}$$

Appendix C

Coefficients of the displacement field $z(x)$

In this Appendix, the explicit expressions for the displacement field $z(x)$ in (4.31) are given. For fixed tangent orientation $\partial_x z(a) = v$, the boundary conditions yield the following coefficients

$$
\begin{aligned}
A_1 = &-\tfrac{k}{\Delta_1}\{-kb\sinh(ka) + k(b - [a - L_{zip}]v)\sinh(kL_{zip}) \\
& + v\,(\cosh(ka) - \cosh(kL_{zip}))\} \\
A_2 = &\tfrac{k}{\Delta_1}\{-kb\cosh(ka) + k(b - [a - L_{zip}]v)\cosh(kL_{zip}) \\
& + v\,(\sinh(ka) - \sinh(kL_{zip}))\} \\
A_3 = &\tfrac{2}{\Delta_1}\sinh(\tfrac{1}{2}k[a - L_{zip}])\{-bk\cosh(\tfrac{1}{2}k[a - L_{zip}]) \\
& + v\sinh(\tfrac{1}{2}k[a - L_{zip}])\} \\
A_4 = &\tfrac{1}{k\Delta_1}\{-k(b - av) + k(b - L_{zip}v)\cosh(k[a - L_{zip}]) \\
& + (bk^2 L_{zip} - v)\sinh(k[a - L_{zip}])\}
\end{aligned}
\tag{C.1}
$$

where

$$
\Delta_1 \equiv 2\sinh(\tfrac{1}{2}k[a - L_{zip}])\{k(a - L_{zip})\cosh(\tfrac{1}{2}k[a - L_{zip}]) - 2\sinh(\tfrac{1}{2}k[a - L_{zip}])\}.
\tag{C.2}
$$

The corresponding transversality condition (4.32) reads

$$
\sqrt{W_{zip}/\kappa} \overset{!}{=} \tfrac{k}{\Delta_1}\{k(b - [a - L_{zip}]v) - kb\cosh(k[a - L_{zip}]) + v\sinh(k[a - L_{zip}])\}. \tag{C.3}
$$

For completeness, we also discuss the case, where the tangent orientation is not restricted by the attachment of the filament ends to the pillar heads, i.e. $\partial_x^2 z(a) = 0$. One finds for the coefficients

$$
\begin{array}{ll}
A_1 = -k^2 b\cosh(ka)/\Delta_2 & A_3 = -kb/\Delta_3 \\
A_2 = k^2 b\sinh(ka)/\Delta_2 & A_4 = b + kab/\Delta_3
\end{array}
\tag{C.4}
$$

with

$$
\begin{aligned}
\Delta_2 &\equiv k(a - L_{zip})\cosh(k[a - L_{zip}]) - \sinh(k[a - L_{zip}]) \\
\Delta_3 &\equiv -k(a - L_{zip}) + \tanh(k[a - L_{zip}]),
\end{aligned}
\tag{C.5}
$$

which finally reduces the transversality condition (4.32) to

$$
\sqrt{W_{zip}/\kappa} \overset{!}{=} k^2 b/\{k(a - L_{zip})\coth(k[a - L_{zip}]) - 1\}. \tag{C.6}
$$

List of Symbols

I	conformation adhering to one step edge or analogous conformation for the striped domain; Chap. 3
II_i	conformation with i bulges adhered to two step edges at a distance a_{st} or analogous conformation for the striped domain; Chap. 3
II_i^n	conformation with i bulges adhered to two steps at a distance na_{st} or analogous conformation for the striped domain; Chap. 3
III	conformation adhering to three step edges; Chap. 3
A	area of the membrane surface
A_i	coefficients of the displacement field z ($i = 1, ..., 4$); App. C
a	length scale characterizing substrate structure; (3.1)
	geometric distance characterizing a pillar configuration; Chap. 4
a_i	geometric distance characterizing a pillar configuration ($i = 1, 2$); Chap. 4
a_{do}	width of a striped domain on the substrate surface; (3.50)
a_{st}	distance between two parallel topographical surface steps; (3.2)
α	angle characterizing two zipped filaments; Chap. 4
b	geometric distance characterizing a pillar configuration; Chap. 4
b_0	bare bond length; (2.5)
b_1	renormalized bond length after 1st RG step; Chap. 2
b_N	renormalized bond length after Nth RG step; Chap. 2
b_i	geometric distance characterizing a pillar configuration ($i = 1, 2$); Chap. 4
β	angle characterizing a pillar configuration; Chap. 4
C_1, C_2	principal curvatures of a membrane; (1.10)
c	integration constant; (3.14), (3.20)
c_i	geometric distance characterizing a pillar configuration ($i = 1, 2$); Chap. 4
c_s	concentration of salt ions; (1.6)
D	approximate diameter of a semiflexible polymer
d	dimension of embedding space
$\partial_s \equiv \frac{\partial}{\partial s}$	partial derivative with respect to s
$\delta_{i,j}$	Kronecker symbol
δ_θ	infinitesimal variation with respect to θ; (3.8)

E	Young's modulus; (1.1)
	complete elliptic integral of the second kind; Chap. 3
ΔE	energy barrier; (3.48)
$\Delta \bar{E}$	dimensionless energy barrier; Chap. 3
E_{ad}	adsorption energy gain induced by surface structure; Chap. 3
E_b	bending energy; Chap. 3
$E_b^{\mathrm{I}}, E_b^{\mathrm{II}}$	bending energy of a shape of type I, II; (3.17), (3.23)
$E_b^{\mathrm{B}}, E_b^{\not{\mathrm{B}}}$	bending energy of a polymer segment with/without bulge;
	(3.36), (3.34), (3.35)
$\tilde{E}_{con}$	typical energy scale for a ring condensate; (3.72)
E_{do}	typical energy scale for a ring adsorbed to a striped domain; (3.57)
E_{st}	typical energy scale for a ring adsorbed to a channel; (3.24)
$\tilde{E}_{st}$	typical energy scale for a ring adsorbed to a periodic array of steps;
	(3.65)
E_{tot}	total energy; Chap. 3
$\bar{E}_{tot}$	dimensionless total energy normalized by E_{st}; Chap. 3
$\bar{E}_{tot}^{\mathrm{I}}$	dimensionless total energy of shape I; (3.30b)
	analogously $\bar{E}_{tot}^{\mathrm{II}_0}, \bar{E}_{tot}^{\mathrm{II}_1}, \bar{E}_{tot}^{\mathrm{II}_2}, ...$
e_0	elementary charge; (1.7)
ϵ, ϵ_0	dielectric constants of the solution and vacuum; (1.7)
F	functionsarising in calculation of energy estimates; (3.33)
$\mathcal{F}$	free energy; Chap. 4
f_1, f_2, f_3	functions arising in minimization procedure; (3.21), App. B
f_{st}	free adsorption energy per segment for a ring adsorbed to a
	channel; (3.49)
f_{zip}	free energy per zipped length; (4.15)
G	Gaussian curvature of a membrane; (1.10), (A.5)
$\mathcal{G}$	radial distribution function; Chap. 4
g_{ij}, g^{ij}, g	metric tensor, its inverse and its determinant; (A.2)
$g^{(0)}$	energy shift arising in 1st RG step; (2.18), (2.19)
$\mathcal{H}$	Hamiltonian
$\mathcal{H}_{\mathrm{dwlc}}$	discrete worm-like chain Hamiltonian; (2.5)
$\mathcal{H}_{\mathrm{mem}}$	membrane Hamiltonian; (1.9)
$\mathcal{H}_{\mathrm{wlc}}$	worm-like chain Hamiltonian of a semiflexible polymer, e.g. (1.2)
h	arbitrary interaction function; Chap. 2
h^*	fixed point interaction function; Chap. 2
$h^{(0)}$	initial interaction function of the semiflexible chain; (2.7)
$h^{(1)}$	renormalized interaction function after 1st RG step; (2.18), (2.19)
$h^{(N)}$	renormalized interaction function after Nth RG step; Fig. 2.3
h_{ij}	curvature tensor of a membrane; (A.5)

I	inertia of a rod's cross section; (1.1)
I_k	modified Bessel function of the first kind; Chap. 2
K	arbitrary interaction parameter; Chap. 2
	complete elliptic integral of the first kind; Chap. 3
K_0	bare interaction parameter of the semiflexible chain; (2.7)
K_1	renormalized interaction parameter after 1st RG step; (2.23)
K_N	renormalized interaction parameter after Nth RG step; Fig. 2.3
k_B	Boltzmann constant, here: $k_B \equiv 1$
k	parameter arising in minimization procedure; (4.30)
k_i	parameters arising in minimization procedure ($i = 1, 2, 3$); (4.38)
κ	mesoscopic bending rigidity; (1.1)
	renormalized bending rigidity; Chap. 2, (2.26), (2.28)
$\bar{\kappa}$	Gaussian bending modulus; (1.9)
κ_0	(bare) bending rigidity at b_0; Chap. 2
κ_1	renormalized bending rigidity after 1st RG step at b_1; (2.24)
κ_N	renormalized bending rigidity after Nth RG step at b_N; (2.25)
κ_i	bending rigidity of the ith filament ($i = 1, 2, 3$); Chap. 4
L	contour length of a semiflexible polymer
$\bar{L}$	contour length of a polymer ring L over the channel width a_{st}; (3.5)
$\bar{L}_{\mathrm{unb}}$	$\bar{L}$ at unbinding transition; (3.44)
$\bar{L}_{\mathrm{I-II}_0}$	$\bar{L}$ at transition between shapes I and II_0; (3.45)
$\bar{L}_{\mathrm{I-II}_2}$	$\bar{L}$ at transition between shapes I and II_2; (3.47)
$\Delta\bar{L}$	dimensionless shift between L_{do} and L_{st}; Fig. 3.6(b)
L_{do}	length of polymer segments adhered to the striped domain; Chap. 3
L_i	contour length of the ith filament ($i = 1, 2$); Chap. 4
$L_{i,p}$	persistence length of the ith filament ($i = 1, 2, 3$); Chap. 4
$L_{i,\shortparallel}$	end-to-end distance of ith filament branch ($i = 1, 2$); Chap. 4
L_{OSF}	additive correction to the persistence length of polyelectrolytes; (1.8)
L_p	persistence length (several definitions); (2.1), (2.27)
$L_{p,red}$	reduced persistence length; (4.16)
L_p^*	persistence length of polyelectrolytes; (1.8)
L_{st}	polymer length adhered to a topographical channel; Chap. 3
$\bar{L}_{st}$	L_{st} in units of the channel width a_{st}; Chap. 3
$\bar{L}_{st}^{\mathrm{I}}$	L_{st} in units of a_{st} of shape I; (3.30a)
L_x	projected length (parametrization by displacement fields; Chap. 1)
L_{zip}	contour length along which two filaments are zipped together; Chap. 4
$L_{zip,\shortparallel}$	end-to-end distance of the zipped filament branch; Chap. 4
L_*	length of curved segments of conformations II; Chap. 3
$L_*^{\mathrm{B}}, L_*^{\cancel{\mathrm{B}}}$	length of a polymer segment with/without bulge; (3.36), (3.34), (3.35)
$L_{\shortparallel}$	end-to-end distance; (4.17)

l	potential range
l_B	Bjerrum length; (1.7)
l_{DH}	screening length; (1.6)
ℓ	length scale
ℓ_x	projected length scale; Chap. 2
Λ_0	high momentum cut-off; (2.2)
Λ	momentum $< \Lambda_0$; (2.2)
λ_k	kth eigenvalue of the transfer matrix T_{ij}; (2.8)
$\lambda_k^{(0)}$	kth initial eigenvalue of the semiflexible chain; (2.14)
$\lambda_k^{(N)}$	kth eigenvalue after Nth RG step; (2.20)
M	mean curvature of a membrane; (1.10), (A.5)
	total number of segments in a semiflexible chain; (2.5)
μ	Lagrange multiplier; (3.12), Chap. 4
μ_i	Lagrange multiplier conserving the contour length of the
	ith filament ($i = 1, 2$); Chap. 4
$\mathbf{N}$	d-dimensional normal vector to a point on the
	membrane surface; (A.1)
ν	Lagrange multiplier; (3.19)
P_i	position of ith pillar head ($i = 1, 2, 3$); Chap. 4
P_l	Legendre polynomial; Chap. 2
p, q	parameters arising in minimization procedure; (3.15), (3.21)
q_s	valency of salt ions; (1.6)
$\Theta_{i,i-1}$	azimuthal angle difference between tangents in $3d$; (2.9)
$\theta_{i,i-1}$	azimuthal angle difference between tangents in $2d$; (2.9)
θ, ϕ	polar/spherical coordinates parametrizing the tangent vector $\mathbf{t}$
$\theta_<, \theta_>$	tangent angles of adhered and non-adhered segments; (3.55)
θ_{inf}	tangent angle at inflection point in a bulged segment; (3.21)
$\mathbf{R}$	d-dimensional position vector to a point on the membrane surface
$\mathbf{R}_i$	d-dimensional tangent vector in s_i direction to a point on the
	membrane surface; (A.1)
R_{co}	contact radius or inverse contact curvature at contact points; (3.27)
$R_{i,co}$	contact radius of the ith filament at the zipping point ($i = 1, 2, 3$);
	Chap. 4
$\mathbf{r}$	d-dimensional position vector to a point on the contour of
	a semiflexible polymer
$\mathbf{r}_i$	position vector of the ith filament contour ($i = 1, 2, 3$); Chap. 4
r	spatial distance; Chap. 1
ρ	Lagrange multiplier; (3.54)
S_{cr}	area of a rod's cross section; (1.1)
s, s'	arc length parametrizing the contour of a semiflexible polymer

s_i	arbitrary coordinates ($i = 1, 2$) parametrizing the membrane; App. A
	arc length parametrizing the ith filament ($i = 1, 2$); Chap. 4
T	temperature in energy units ($k_B \equiv 1$)
$T_{i,j}$	transfer matrix; (2.7)
$\mathbf{t}$	d-dimensional tangent vector to a point on the contour of a semiflexible polymer
t_i	polar coordinates ($i = 1, 2$); Chap. 4
u	scalar product of tangents; Chap. 2
V_{con}	potential describing the effective attraction between polymer segments causing condensation; (3.70)
V_{do}	effective lateral adsorption potential induced by a chemically striped domain; (3.50)
V_{st}	effective lateral adsorption potential induced by two parallel topographical surface steps; (3.2)
V_{zip}	potential describing the interfilamental attraction; (4.1)
v_{zip}	derivative of the displacement field z at the zipping point; (4.34)
W	adsorption or attraction energy gain per length
W_{con}	energy gain per length from condensation; (3.70)
W_{do}	adsorption energy gain per length at a chemically striped domain; (3.50)
W_{st}	adsorption energy gain per length at a topographical step; (3.2)
$W_{c,st}$	critical potential strength; (3.49)
W_{zip}	energy gain per zipped length; (4.1)
$W_{c,zip}$	critical potential strength; (4.15)
w_1	lower stability boundary of shape II_1; (3.43)
w_2	lower stability boundary of shape II_2; (3.39), (3.40)
$\tilde{w}_{con}$	reduced potential strength of condensation; (3.71)
w_{do}	reduced adsorption strength of a striped domain; (3.57)
$|w_{do}|_{\mathrm{I-II}_0}$	$|w_{do}|$ at transition between shapes I and II_0; (3.61)
$\tilde{w}_{do}$	reduced adsorption strength of a striped domain; (3.57)
w_{st}	reduced adsorption strength of a topographical channel; (3.6)
$\tilde{w}_{st}$	reduced adsorption strength of a topographical channel; (3.7)
$|w_{st}|_{\mathrm{unb}}$	$|w_{st}|$ at unbinding transition; (3.44)
$|w_{st}|_{\mathrm{II}_0-\mathrm{II}_2}$	$|w_{st}|$ at transition between shapes II_0 and II_2; (3.46)
	analogously $|w_{st}|_{\mathrm{I-II}_0^{\mathrm{nmax}}}$, $|w_{st}|_{\mathrm{II}_0^{\mathrm{n}}-\mathrm{II}_0^{\mathrm{n-1}}}$, ...
Ω	solid angle in $3d$; (2.13)
x, y	Euclidean coordinates parametrizing a polymer or a membrane (parametrization by displacement fields; Chap. 1)
$\Delta x, \Delta y$	distances in x- and y-direction; Fig. 3.8(a),(c),(d)
x_{zip}	x-coordinate of the zipping point; (4.34)

Y_{lm} spherical harmonic; Chap. 2

ψ_k kth eigenfunction of the transfer matrix T_{ij}; (2.8)

Z position of the zipping point; Chap. 4

$\mathcal{Z}_M$ partition function of a semiflexible chain with M segments; (2.6)

z $(d-1)$-dimensional displacement vector for semiflexible polymers
$(d-2)$-dimensional height vector for fluid membranes
(parametrization by displacement fields; Chap. 1)

z_i one-dimensional displacement field describing the ith filament
branch ($i = 1, 2, 3$); Chap. 4

z_{zip} z-coordinate of the zipping point; (4.34)

List of Figures

List of Figures

Bibliography

[1] C. Dekker. Carbon nanotubes as molecular quantum wires. *Physics Today*, 52:22–28, 1999.

[2] H. Lodish, A. Berk, S.L. Zipursky, P. Matsudaira, D. Baltimore, and J.E. Darnell. *Molecular Cell Biology*. W.H. Freeman and Company, New York, 2000.

[3] B. Alberts, D. Bray, J. Lewis, M. Raff, K. Roberts, and J.D. Watson. *Molecular Biology of the Cell*. Garland Publishing, New York, 1994.

[4] http://www.physics.drexel.edu/ferrone/Frank_Ferrone_Research.html.

[5] M. Sano, A. Kamino, J. Okamura, and S. Shinkai. Ring Closure of Carbon Nanotubes. *Science*, 293:1299–1301, 2001.

[6] W.H. Taylor and P.J. Hagerman. Application of the method of phageT4 DNA ligase-catalyzed ring-closure to the study of DNA structure. II. NaCl-dependence of DNA flexibility and helical repeat. *J. Mol. Biol.* , 212:363–376, 1990.

[7] J. Käs, H. Strey, and E. Sackmann. Direct imaging of reptation for semi-flexible actin filaments. *Nature*, 368:226–229, 1994.

[8] J.C. Wang, M.S. Turner, G. Agarwal, S. Kwong, R. Josephs, F.A. Ferrone, and R.W. Briehl. Micromechanics of isolated sickle cell hemoglobin fibers: bending moduli and persistence lengths. *J. Mol. Biol.* , 315:601–612, 2002.

[9] F. Gittes, B. Mickey, J. Nettleton, and J. Howard. Flexural Rigidity of Microtubules and Actin Filaments Measured from Thermal Fluctuations in Shape. *J. Mol. Biol.* , 120:923–934, 1993.

[10] A. Amzallag, C. Vaillant, M. Jacob, M. Unser, J. Bednar, J.D. Kahn, J. Dubochet, A. Stasiak, and J.H. Maddocks. 3D reconstruction and comparison of shapes of DNA minicircles observed by cryo-electron microscopy. *Nucl. Acid Res.* , 34:e125, 2006.

Bibliography

[11] D.M. Hatters, C.A. MacRaild, R. Daniels, W.S. Gosal, N.H. Thomson, J.A. Jones, J.J. Davis, C.E. MacPhee, C.M. Dobson, and G.J. Howlett. The circularization of amyloid fibrils formed by apolipoprotein C-II. *Biophys. J.*, 85:3979–3990, 2003.

[12] R. Martel, H.R. Shea, and P. Avouris. Rings of single-walled carbon nanotubes. *Nature*, 398:299–299, 1999.

[13] J.X. Tang, J.A. Käs, J.V. Shah, and P.A. Janmey. Counterion-induced actin ring formation. *Eur. Biophys. J.*, 30:477–484, 2001.

[14] V.A. Bloomfield. Condensation oDNAna by multivalent cations - considerations on mechanism. *Biopolymers*, 31:1471–1481, 1991.

[15] P.G. de Gennes. *Scaling Concepts in Polymer Physics*. Cornell University Press, Ithaca, 1979.

[16] M. Doi and S.F. Edwards. *The Theory of Polymer Dynamics*. Clarendon, Oxford, 1986.

[17] A.Y. Grosberg and A.R. Khokhlov. *Statistical Physics of Macromolecules*. American Institute of Physics Press, New York, 1994.

[18] E.M. Lifshitz and L.D. Landau. *Theory of Elasticity*. Pergamon Press, New York, 1986.

[19] O. Kratky and G. Porod. Röntgenuntersuchung aufgelöster Fadenmoleküle. *Recl. Trav. Chim. Pays-Bas*, 68:1106–1122, 1949.

[20] E.M. Lifshitz and L.D. Landau. *Statistical Physics, Part 1*. Pergamon Press, New York, 1969.

[21] H. Kleinert. *Path integrals in quantum mechanics, statistics, polymer physics, and financial markets*. World Scientific Publishing, Singapore, 2004.

[22] J.F. Marko and E.D. Siggia. Stretching DNA. *Macromolecules*, 28:8759–8770, 1995.

[23] P. Cluzel, A. Lebrun, C. Heller, R. Lavery, J.L. Viovy, D. Chatenay, and F. Caron. DNA: An Extensible Molecule. *Science*, 271:792–794, 1996.

[24] X. Liu and G.H. Pollack. Mechanics of F-Actin Characterized with Microfabricated Cantilevers. *Biophys. J.*, 83:2705–2715, 2002.

[25] T. Hugel, M. Grosholz, H. Clausen-Schaumann, A. Pfau, H. Gaub, and M. Seitz. Elasticity of single polyelectrolyte chains and their desorption from solid supports studied by AFM based single molecule force spectroscopy. *Macromolecules*, 34:1039–1047, 2001.

[26] N. Saito, K. Takahashi, and Y. Yunoki. The Statistical Mechanical Theory of Stiff Chains. *J. Phys. Soc. Jpn.* , 22:219–226, 1967.

[27] T. Odijk. Stiff Chains and Filaments under Tension. *Macromolecules*, 28:7016–7018, 1995.

[28] M.D. Wang, H. Yin, R. Landick, J. Gelles, and S.M. Block. Stretching DNA with optical tweezers. *Biophys. J.* , 72:1335–1346, 1997.

[29] C. Bouchiat, M.D. Wang, J.F. Allemand, T. Strick, S.M. Block, and V. Croquette. Estimating the Persistence Length of a Worm-Like Chain Molecule from Force-Extension Measurements. *Biophys. J.* , 76:409–413, 1999.

[30] R. Goetz and R. Lipowsky. Computer simulations of bilayer membranes: Self-assembly and interfacial tension. *J. Chem. Phys.*, 108:7397–7409, 1998.

[31] R.R. Netz. Strongly stretched semiflexible extensible polyelectrolytes and DNA. *Macromolecules*, 34:7522–7529, 2001.

[32] J. Kierfeld, O. Niamploy, V. Sa-yakanit, and R. Lipowsky. Stretching of semiflexible polymers with elastic bonds. *Eur. Phys. J. E*, 14:17–34, 2004.

[33] J.L. Barrat and J.F. Joanny. Theory of polyelectrolyte solutions. In I. Prigogine and S.A. Rice, editors, *Advances in chemical physics, Vol. XCIV.* John Wiley & Sons, New York, 1996.

[34] T. Odijk. Polyelectrolytes near the rod limit. *J. Polym. Sci.* , 15:477–483, 1977.

[35] J. Skolnick and M. Fixman. Electrostatic persistence length of a wormlike polyelectrolyte. *Macromolecules*, 10:944–948, 1977.

[36] J.F. Marko. Introduction to single-DNA micromechanics. In D. Chatenay, S. Cocco, R. Monasson, D. Thieffry, and J. Dalibard, editors, *Multiple Aspects of DNA and RNA: from Biophysics to Bioinformatics, Session LXXXII.* Elsevier, Amsterdam, 2005.

[37] V.A. Bloomfield. DNA condensation by multivalent cations. *Biopolymers*, 44:269–282, 1991.

[38] P. Janmey, J.X. Tang, and C.F. Schmidt. *Actin Filaments* in *Biophysics Textbook online.* http://www.biophysics.org/btol/.

[39] G.S. Manning. The molecular theory of polyelectrolyte solutions with applications to the electrostatic properties of polynucleotides. *Q. Rev. Biophys.* , 11:179–246, 1978.

[40] A. Naji, S. Jungblut, A.G. Moreira, and R.R. Netz. Electrostatic interactions in strongly coupled soft matter. *Physica A*, 352:131–170, 2005.

[41] N.V. Hud and K.H. Downing. Cryoelectron microscopy of lambda phage DNA condensates in vitreous ice: The fine structure of DNA toroids. *Proc. Nat. Acad. Sci. USA*, 98:14925–14930, 2001.

[42] http://en.wikipedia.org/wiki/Cytoskeleton.

[43] K.R. Ayscough. In vivo functions of actin-binding proteins. *Curr. Opin. Cell Biol.* , 10:102–11, 1998.

[44] S.J. Winder. Structural insights into actin-binding, branching and bundling proteins. *Curr. Opin. Cell Biol*, 15:14–22, 2003.

[45] R.R. Netz and D. Andelman. Neutral and charged polymers at interfaces. *Physics reports*, 380:1–95, 2003.

[46] S.S. Sheiko and M. Möller. Visualization of Macromolecules - A first step to manipulation and controlled response. *Chem. Rev.* , 101:4099–4123, 2001.

[47] T. Hertel, R.E. Walkup, and P. Avouris. Deformation of carbon nanotubes by surface van der Waals forces. *Phys. Rev. B*, 58:13870–13873, 1998.

[48] M. Burghard, G. Duesberg, G. Philipp, J. Muster, and S. Roth. Controlled Adsorption of Carbon Nanotubes on Chemically Modified Electrode Arrays. *Adv. Mater.* , 10:584–588, 1998.

[49] J. Kierfeld and R. Lipowsky. Unbundling and desorption of semiflexible polymers. *Europhys. Lett.* , 62:285–291, 2003.

[50] S.B. Smith, L. Finzi, and C. Bustamante. Direct mechanical measurements of the elasticity of single DNA molecules by using magnetic beads. *Science*, 258:1122–1126, 1992.

[51] A. Ashkin. Applications of Laser Radiation Pressure. *Science*, 210:1081–1088, 1980.

[52] G. Binnig, C.F. Quate, and C. Gerber. Atomic force microscope. *Phys. Rev. Lett.* , 56:930–933, 1986.

[53] C. Bustamante, J.F. Marko, E.D. Siggia, and S.B. Smith. Entropic elasticity of lambda-phage DNA. *Science*, 265:1599–1600, 1994.

[54] J.P. Spatz, S. Gräter, W.H. Roos, and J. Ulmer. Oberfläche mit einer Anordnung einer Vielzahl säulenförmiger Erhebungen und deren Anwendungen, German patent pending, 2004.

[55] http://www.mpikg.mpg.de/lipowsky/res/rmem/image01.html.

[56] P.B. Canham. The minimum energy of bending as a possible explanation of the biconcave shape of the human red blood cell. *J. Theor. Biol.* , 26:61–81, 1970.

[57] W. Helfrich. Elastic properties of lipid bilayers: theory and possible experiments. *Z. Naturforsch.* , 28c:693–703, 1973.

[58] E. Evans. Bending moments and chemically induced moments in membrane bilayers. *Biophys. J.* , 14:923–931, 1974.

[59] R. Lipowsky. The conformation of membranes. *Nature*, 349:475–481, 1991.

[60] H.P. Duwe, J. Käs, and E. Sackmann. Bending elastic-moduli of lipid bilayers - modulation by solutes. *J. Phys. Fr.* , 51:945–962, 1990.

[61] M. Mutz and W. Helfrich. Bending rigidities of some biological model membranes as obtained from the fourier-analysis of contour sections. *J. Phys. Fr.* , 51:991–1002, 1990.

[62] P.G. de Gennes and C. Taupin. Microemulsions and the Flexibility of Oil/Water Interfaces. *J. Phys. Chem.* , 86:2294–2304, 1982.

[63] R. Lipowsky and E. Sackmann. *Structure and Dynamics of Membranes: from Cells to Vesicles (Handbook of Biological Physics vol 1)*. Elsevier, Amsterdam, 1995.

[64] U. Seifert. Configurations of fluid membranes and vesicles. *Advances in Physics*, 46:13–137, 1997.

[65] P. Gutjahr, R. Lipowsky, and J. Kierfeld. Persistence length of semiflexible polymers and bending rigidity renormalization. *Europhys. Lett.* , 76:994–1000, 2006.

[66] J. Kierfeld, P. Gutjahr, T. Kühne, P. Kraikivski, and R. Lipowsky. Buckling, Bundling, and Pattern Formation: From Semi-Flexible Polymers to Assemblies of Interacting Filaments. *J. Comput. Theor. Nanosci.* , 3:898–911, 2006.

[67] R. Capovilla and J. Guven. Helfrich-Canham bending energy as a constrained nonlinear sigma model. *J. Phys. A: Math. Gen.* , 38:2593–2597, 2005.

[68] L. Fadeev and V.N. Popov. Feynman diagrams for the Yang-Mills field. *Phys. Lett. B*, 25:29–30, 1967.

[69] V.N. Popov. *Functional Integrals in Quantum Field Theory and Statistical Physics*. Kluwer Academic Publisher, Dordrecht, 1983.

[70] F. David. Geometry and field theory of random surfaces and membranes. In D. Nelson, T. Piran, and S. Weinberg, editors, *Statistical Mechanics of Membranes and Surfaces*. World Scientific, Singapore, 1989.

[71] P. Nelson and T. Powers. Renormalization of chiral couplings in tilted bilayer membranes. *J. Phys. France II*, 3:1535–1569, 1993.

[72] W. Cai, T.C. Lubensky, P. Nelson, and T. Powers. Measure factors, tension, and correlations of fluid membranes. *J. Phys. II France*, 4:931–949, 1994.

[73] W. Helfrich. Effect of thermal undulations on the rigidity of fluid membranes and interfaces. *J. Physique*, 46:1263–1268, 1985.

[74] W. Helfrich. Size distributions of vesicles: the role of the effective rigidity of membranes. *J. Physique*, 47:321–329, 1986.

[75] W. Helfrich. Measures of integration in calculating the effective rigidity of fluid surfaces. *J. Physique*, 48:285–289, 1987.

[76] L. Peliti and S. Leibler. Effects of Thermal Fluctuations on Systems with Small Surface Tension. *Phys. Rev. Lett.* , 54:1690–1693, 1985.

[77] D. Förster. On the scale dependence, due to thermal fluctuations, of the elastic properties of membranes. *Phys. Lett.* , 114A:115–120, 1986.

[78] H. Kleinert. Thermal softening of curvature elasticity in membranes. *Phys. Lett.* , 114A:263–268, 1986.

[79] W. Helfrich. Stiffening of fluid membranes and entropy loss of membrane closure: Two effects of thermal undulations. *Eur. Phys. J. B*, 1:481–489, 1998.

114

[80] H. Pinnow and W. Helfrich. Effect of thermal undulations on the bending elasticity and spontaneous curvature of fluid membranes. *Eur. Phys. J. E*, 3:149–157, 2000.

[81] A.M. Polyakov. *Gauge Fields and Strings*. Harwood Academic Publishers, Chur, 1987.

[82] L. Livadaru, R.R. Netz, and H.J. Kreuzer. Stretching response of discrete semiflexible polymers. *Macromolecules*, 36:3732–3744, 2003.

[83] M. Abramowitz and A.I. Stegun. *Handbook of Mathematical functions*. Natl. Bur. Stand. , Washington, 1965.

[84] M.E. Fisher. Magnetism in One-Dimensional Systems: The Heisenberg Model for Infinite Spin. *Am. J. Phys.* , 32:343–346, 1964.

[85] G.S. Joyce. Classical Heisenberg Model. *Phys. Rev.* , 155:487–491, 1967.

[86] Th. Niemeijer and Th.W. Ruijgrok. Renormalization Group Solution of the One-Dimensional Classical Heisenberg Model. *Physica*, 81A:427–440, 1975.

[87] M. Nauenberg. Renormalization group solution of the one dimensional Ising model. *J. Math. Phys.* , 16:703–705, 1975.

[88] F. Jülicher, R. Lipowsky, and H. Müller-Krumbhaar. Exact functional renormalization group for wetting transitions in $1 + 1$ dimensions. *Europhys. Lett.* , 11:657–662, 1990.

[89] H. Spohn. Fixed points of a functional renormalization group for critical wetting. *Europhys. Lett.* , 14:689–692, 1991.

[90] P. Samori. Scanning probe microscopies beyond imaging. *J. Mater. Chem.* , 14:1353–1366, 2004.

[91] J. Muster, M. Burghard, S. Roth, G.S. Duesberg, E. Hernández, and A. Rubio. Scanning force microscopy characterization of individual carbon nanotubes on electrode arrays. *J. Vac. Sci. Technol. B*, 16:2796–2801, 1998.

[92] J. Liu, M.J. Casavant, M. Cox, D.A. Walters, P. Boul, W. Lu, A.J. Rimberg, K.A. Smith, D.T. Colbert, and R.E. Smalley. Controlled deposition of individual single-walled carbon nanotubes on chemically functionalized templates. *Chem. Phys. Lett.* , 303:125–129, 1999.

[93] Y. Wang, D. Maspoch, S. Zou, G.C. Schatz, R.E. Smalley, and C.A. Mirkin. Controlling the shape, orientation, and linkage of carbon nanotube features with nano affinity templates. *Proc. Nat. Acad. Sci. USA*, 103:2026–2031, 2006.

[94] N. Severin, W. Zhuang, C. Ecker, A.A. Kalachev, I.M. Sokolov, and J.P. Rabe. Blowing DNA bubbles. *Nano Lett.* , 6:2561–2566, 2006.

[95] B. Schnurr, F.C. MacKintosh, and D.R.M. Williams. Dynamical intermediates in the collapse of semiflexible polymers in poor solvents. *Europhys. Lett.* , 51:279–285, 2000.

[96] B. Schnurr, F. Gittes, and F.C. MacKintosh. Metastable intermediates in the condensation of semiflexible polymers. *Phys. Rev. E.* , 65:061904, 2002.

[97] A. Cēbers, Z. Dogic, and P.A. Janmey. Counterion-mediated attraction and kinks on loops of semiflexible polyelectrolyte bundles . *Phys. Rev. Lett.* , 96:247801, 2006.

[98] Y. Fang, J.H. Hoh, and O. Journals. Surface-directed DNA condensation in the absence of soluble multivalent cations. *Nucl. Acids Res.* , 26:588–593, 1998.

[99] R. Golan, L.I. Pietrasanta, W. Hsieh, and H.G. Hansma. DNA toroids: stages in condensation. *Biochemistry*, 38:14069–14076, 1999.

[100] V.I. Arnold. *Catastrophe Theory.* Springer-Verlag, Berlin, 2004.

[101] K.A. Brakke. The Surface Evolver. *Exp. Math.* , 1:141–165, 1992.

[102] U. Seifert and R. Lipowsky. Adhesion of vesicles. *Phys. Rev. A*, 42:4768–4771, 1990.

[103] U. Seifert. Adhesion of vesicles in 2 dimensions. *Phys. Rev. A*, 43:6803–6814, 1991.

[104] J. Kierfeld and R. Lipowsky. Unbundling and desorption of semiflexible polymers. *Europhys. Lett.* , 62:285–291, 2003.

[105] J. Kierfeld. Force-Induced Desorption and Unzipping of Semiflexible Polymers. *Phys. Rev. Lett.* , 97:58302, 2006.

[106] I. Ali, D. Marenduzzo, and J.M. Yeomans. Polymer packaging and ejection in viral capsids: Shape matters. *Phys. Rev. Lett.* , 96:208102, 2006.

[107] L. Boué, M. Adda-Bedia, A. Boudaoud, D. Cassani, Y. Couder, A. Eddi, and M. Trejo. Spiral Patterns in the Packing of Flexible Structures. *Phys. Rev. Lett.* , 97:166104, 2006.

[108] J.X. Tang and P.A. Janmey. The Polyelectrolyte Nature of F-actin and the Mechanism of Actin Bundle Formation. *J. Biol. Chem.* , 271:8556–8563, 1996.

[109] M. Tempel, G. Isenberg, and E. Sackmann. Temperature-induced sol-gel transition and microgel formation in α-actinin cross-linked actin networks: A rheological study. *Phys. Rev. E*, 54:1802–1810, 1996.

[110] O. Pelletier, E. Pokidysheva, L.S. Hirst, N. Bouxsein, Y. Li, and C.R. Safinya. Structure of Actin Cross-Linked with α-Actinin: A Network of Bundles. *Phys. Rev. Lett.* , 91:148102, 2003.

[111] M.L. Gardel, J.H. Shin, F.C. MacKintosh, L. Mahadevan, P. Matsudaira, and D.A. Weitz. Elastic Behavior of Cross-Linked and Bundled Actin Networks. *Science*, 304:1301–1305, 2004.

[112] P.A. Janmey, S. Hvidt, J. Käs, D. Lerche, A. Maggs, E. Sackmann, M. Schliwa, and T.P. Stossel. The mechanical properties of actin gels. Elastic modulus and filament motions. *J. Biol. Chem.* , 269:32503–32513, 1994.

[113] E. Helfer, S. Harlepp, L. Bourdieu, J. Robert, F.C. MacKintosh, and D. Chatenay. Buckling of Actin-Coated Membranes under Application of a Local Force. *Phys. Rev. Lett.* , 87:88103, 2001.

[114] E. Helfer, S. Harlepp, L. Bourdieu, J. Robert, F.C. MacKintosh, and D. Chatenay. Viscoelastic properties of actin-coated membranes. *Phys. Rev. E*, 63:21904, 2001.

[115] D. Humphrey, C. Duggan, D. Saha, D. Smith, and J. Käs. Active fluidization of polymer networks through molecular motors. *Nature*, 416:413–416, 2002.

[116] W.H. Roos, A. Roth, J. Konle, H. Presting, E. Sackmann, and J.P. Spatz. Freely Suspended Actin Cortex Models on Arrays of Microfabricated Pillars. *ChemPhysChem*, 4:872–877, 2003.

[117] J. Uhde, M. Keller, E. Sackmann, A. Parmeggiani, and E. Frey. Internal Motility in Stiffening Actin-Myosin Networks. *Phys. Rev. Lett.*, 93:268101, 2004.

[118] B. Essevaz-Roulet, U. Bockelmann, and F. Heslot. Mechanical separation of the complementary strands of DNA. *Proc. Nat. Acad. Sci. USA*, 94:11935–11940, 1997.

[119] D.K. Lubensky and D.R. Nelson. Pulling Pinned Polymers and Unzipping DNA. *Phys. Rev. Lett.* , 85:1572–1575, 2000.

[120] S. Cocco, R. Monasson, and J.F. Marko. Force and kinetic barriers to unzipping of the DNA double helix. *Proc. Nat. Acad. Sci. USA*, 98:8608–8613, 2001.

[121] U. Bockelmann, P. Thomen, B. Essevaz-Roulet, V. Viasnoff, and F. Heslot. Unzipping DNA with Optical Tweezers: High Sequence Sensitivity and Force Flips. *Biophys. J.* , 82:1537–1553, 2002.

[122] R.W. Briehl. Nucleation, Fiber Growth and Melting, and Domain Formation and Structure in Sickle Cell Hemoglobin. *J. Mol. Biol.* , 245:710–723, 1995.

[123] C.W. Jones, J.C. Wang, R.W. Briehl, and M.S. Turner. Measuring Forces between Protein Fibers by Microscopy. *Biophys. J.* , 88:2433–2441, 2005.

[124] W.H. Roos. Biomimetic cytoskeleton assemblies and living cells on micropillar force sensor arrays. PhD thesis, University of Heidelberg, 2004.

[125] M.M.A.E. Claessens, M. Bathe, E. Frey, and A.R. Bausch. Actin-binding proteins sensitively mediate F-actin bundle stiffness. *Nat. Mater.* , 5:748–753, 2006.

[126] R.R. Netz. Pulling adsorbed polymers from surfaces with the AFM: stick vs. slip, peeling vs. gliding. *Europhys. Lett.* , 73:292–298, 2006.

[127] J. Wilhelm and E. Frey. Radial Distribution Function of Semiflexible Polymers. *Phys. Rev. Lett.* , 77:2581–2584, 1996.

[128] M.P. do Carmo. *Differential Geometry of Curves and Surfaces.* Prentice-Hall, Inc. , Englewood Cliffs, 1976.

Danke ...

So viele haben direkt oder indirekt zu dieser Arbeit beigetragen – bei ihnen allen möchte ich mich an dieser Stelle bedanken. Mein ganz besonderer Dank gilt ...

... Reinhard Lipowsky, der mich in seine Gruppe aufgenommen und mir den „Sprung über den Campus" überhaupt ermöglicht hat, für seine Anregungen und seine Unterstützung.

... Jan Kierfeld für viele lange und lehrreiche Diskussionen, Geduld, Zeit, Ratschläge, Unterstützung und seinen Humor, der all das so angenehm gemacht hat.

... Joachim P. Spatz und Simon Schulz für die interessante Zusammenarbeit.

... Ruben Gracia für hilfreiche Diskussionen.

... der DFG für die finanzielle Unterstützung im Rahmen des SFB 448.

... Gudrun Conrad, Angelo Valleriani und Christian Seidel insbesondere für die Organisation schöner Klassenfahrten.

... den aktuellen und ehemaligen Doktorandenvertretern dafür, dass sie das Campusleben lebendiger machen.

... der ganzen Theoriegruppe für die entspannte Arbeitsatmosphäre.

... meinem Büro für den Spaß und die vielen kleinen aufmunternden Pausen.

... den Experimentatoren für die frühen Mittagessen.

... außerdem Andrea Grafmüller, Carmen Remde, Rumiana Dimova und Janina Beeg für die schöne Zeit am Institut und vieles mehr.

... meiner Familie für alles, was an dieser Stelle keinen Platz hat.